UNIVERSIDAD POLITÉCNICA DE MADRID
Escuela Técnica Superior de Ingenieros de Caminos, Canales y Puertos

Effect of grain boundaries on the deformation and fracture of metallic polycrystals

DOCTORAL THESIS

Submitted for the degree of Doctor by:

María Eugenia Nieto Valeiras
Master in Materials Engineering

Madrid, 2023


UNIVERSIDAD POLITÉCNICA DE MADRID
Escuela Técnica Superior de Ingenieros de Caminos, Canales y Puertos

Doctoral Degree in Engineering of Structures, Foundations and Materials

Effect of grain boundaries on the deformation and fracture of metallic polycrystals

DOCTORAL THESIS

Submitted for the degree of Doctor by:

María Eugenia Nieto Valeiras
Master in Materials Engineering

Under the supervision of:
Dr. Javier LLorca

Madrid, 2023

Title: Effect of grain boundaries on the deformation and fracture of metallic polycrystals
Author: María Eugenia Nieto Valeiras
Doctoral Programme: Engineering of Structures, Foundations and Materials

Thesis Supervision:

Dr. Javier LLorca, University Professor, Universidad Politécnica de Madrid

External Reviewers:

Thesis Defense Committee:

Thesis Defense Date:

Para Milocho.

Acknowledgements

I would like to acknowledge the financial support from the European Research Council under the European Union's Horizon 2020 research and innovation programme (Advanced Grant VIRMETAL, grant agreement No. 669141) and to the Grant Program for Research and Teaching Stays in the USA of the Polytechnic University of Madrid, for conceding me the grant for my research stay at Purdue University.

A PhD thesis is a long, tortuous way, and there are a lot of people who have accompanied me along this journey. However, I would rather express my gratitude in my mother tongue.

En primer lugar, quiero darle las gracias a mi supervisor, Javier LLorca. Dicen que la relación entre un doctorando y su supervisor es una de las grandes claves del éxito en la investigación académica. En mi caso, me siento tremendamente afortunada de haber recorrido este camino junto a Javier. Gracias por toda la confianza depositada, el inmenso conocimiento compartido y la formación del más alto nivel que he podido recibir. Gracias por creer en mí, por acompañarme en momentos difíciles y por organizar las millones de ideas en esta cabecita alocada. Ha sido un privilegio poder compartir tanto ratos de ecuaciones en la pizarra y conversaciones científicas, como nuestra pequeña rivalidad en cierto deporte de raqueta.

En segundo lugar, quiero agradecer a Nik Chawla y a su grupo de investigación por haberme acogido con tanto cariño en Purdue desde el primer momento. Gracias a Nik por involucrarme en todas las actividades, tanto académicas como no académicas, y por dejarme aprender y enseñar. Mi formación profesional no sería la que es si no hubiese pasado cinco meses como parte del Chawla Research Group. Gracias a todos mis compañeros del grupo, Eshan, Hamid, Swapnil, Daniel, Rahul, Amey, John, Ted, Ankit y Min, por acompañarme en mi aventura americana. En especial quiero darle las gracias a Eshan, con el que siempre es un placer trabajar o simplemente perderse en la ciencia con un café.

Esta tesis y el poso que deja en mí no serían lo mismo si no se hubiese llevado a cabo en IMDEA Materiales. Después de casi cinco años bajo ese techo acristalado echo la vista atrás y hay tantas personas a las que tengo que dar las gracias que no podría nombrarlas a todas. Recordando mis primeros años de tesis tengo que darles las gracias a Sarra Haouala y a Alberto Orozco, a los que he sentido como mentores desde el principio y de los que he aprendido tantísimo. A Bárbara, probablemente mi mejor compañera de mesa, a la que admiro profundamente. A los técnicos de IMDEA, que siempre han estado disponibles para echarme una mano, y en especial a Amalia, por su tiempo y por su inmensa paciencia. A mis compañeros del grupo de investigación, Abbas, Biaobiao, y especialmente a mi amiga Maral, que me ha acompañado en tantísimos momentos felices y no tan felices, y quién siempre ha tenido un hueco para mí. Gracias a toda la gente que trabaja en IMDEA, desde investigadores, postdocs, predocs, y gente de la cuarta planta, hasta el personal de limpieza, recepción y mantenimiento. Es muy fácil trabajar en algo tan frustrante como la ciencia cuando estás rodeada de personas tan estupendas y cariñosas. Además, quiero darle las gracias a la gente de la segunda planta porque gracias a ellos me siento como en

casa. Gracias también a todos los que se toman (o en algún momento se han tomado) el café a las 11, comen a las 2, y comen en Getafe los viernes, porque la rutina nunca es rutina con vosotros.

Finalmente quiero dedicarles unas palabras a esas personas que han sido un apoyo imprescindible para mí durante estos años de tesis. Gracias a mis compañeros de IMDEA que se han convertido en amigos del alma, Andrés, Ángela, Carmen, David, Guille, Jorge, Lola, Nacho Escobar, y Nacho Rodríguez. Por hacer los días infinitamente más divertidos, reír conmigo en los momentos alegres y acompañarme en los momentos difíciles. No puedo no dar una mención especial a mi gran apoyo y casi hermano Nacho Escobar, por no dejar de animarme y de creer en mí y por estar siempre ahí incondicionalmente. Esta tesis también es un poquito tuya. A mis amigos de Ourense y de Madrid, que tengo la fortuna de tener desde hace muchísimos años y que espero disfrutar, como mínimo, de otros tantos más. A Picu, porque ha sido un pilar fundamental durante muchos años a pesar de escuchar a diario un montón de datos innecesarios sobre bordes de grano. Por ser mi mejor amigo y hacerme reír hasta llorar, y llorar conmigo hasta reír. Por último, quiero darle las gracias a mi familia, que siempre me han creído capaz de todo lo que me proponga. Soy una privilegiada por tenerles a mi lado y por formar parte de una piña tan unida. Gracias a mis tías y a mis hermanos, de los que me siento profundamente orgullosa. Gracias a mis padres, por invertir tantísimo en mí, en mi educación y en mi felicidad, y por enseñarme que si estamos juntos podemos con todo. Gracias papá por ser mi fan número uno y por enseñarme a no darme nunca por vencida. Espero que estés orgulloso, te llevo conmigo.

Abstract

Metallic materials stand for the standard materials for structural applications in engineering. However, the strength of pure metals is rather limited due to the development of plastic deformation by dislocation slip. Different strengthening mechanisms have been employed to create obstacles that hinder dislocation motion through the crystalline lattice. Grain boundaries stand among the strongest barriers to dislocation slip in polycrystals, playing a critical role in their mechanical properties. However, grain boundaries can trigger damage, induce size effects such as the Hall-Petch effect, or weaken the material due to irradiation and hydrogen embrittlement. Designing materials with grain boundaries resistant to such effects is essential for increasing the lifespan and safety of critical components and requires understanding the interaction of dislocations with grain boundaries. The experimental evidence has revealed dislocations can transfer slip to the neighbor grain through the grain boundary in some cases, while dislocation pile-ups are formed in other grain boundaries. Nevertheless, there is still no general agreement on the criteria to predict slip transfer in polycrystalline materials.

This thesis aims to analyze the mechanisms of dislocation/grain boundary interaction in metallic polycrystals from the experimental and simulation viewpoints. The occurrence of slip transfer and blocking has been analyzed in thin pure nickel (face-centered cubic) and pure titanium (hexagonal close-packed) polycrystals. State-of-the-art experimental techniques, such as electron backscatter diffraction-based slip trace analysis, diffraction contrast tomography, and high-resolution digital image correlation, have been used to characterize the microstructure and determine the conditions for slip transfer. In particular, diffraction contrast tomography was employed to determine the effect of the three-dimensional grain boundary geometry on slip transfer, and high-resolution digital image correlation was used to account for the effect of the local stress state around grain boundaries. A large database of slip transfer/blocking events acquired in nickel and titanium was used to validate/disprove the accuracy of the geometrical criteria for slip transfer across grain boundaries available in the literature.

In addition, an existing crystal plasticity model was extended to include the strengthening effect of grain boundaries and the possibility of slip transfer on the mechanical behavior of face-centered cubic and hexagonal close-packed polycrystals. A variety of geometrical slip transfer criteria were successfully implemented and were used to simulate the effect of grain size on the flow strength of face-centered cubic and hexagonal close-packed polycrystals by means of computational homogenization. The simulations were validated against experimental data of the tensile response of well-annealed cubic and hexagonal polycrystals found in the literature. Subsequently, the effect of slip transfer on intergranular fracture was studied through the insertion of cohesive surfaces at the grain boundaries of polycrystalline foils to determine the effect of grain boundary character and geometry on the strength and fracture of metallic polycrystals.

The main results of Chapter 2 of this thesis have been published in

E. Nieto-Valeiras, J. LLorca,
Criteria for slip transfer across grain and twin boundaries in pure Ni,
Materialia **21**, 101303 (2022)

The main results of Chapter 3 of this thesis have been published in

E. Ganju, E. Nieto-Valeiras, N. Chawla, J. LLorca,
A novel diffraction contrast tomography (DCT) acquisition strategy for capturing the 3D crystallographic structure of pure titanium,
Tomography of Materials and Structures **1**, 100003 (2023)

The main results of Chapter 4 of this thesis have been published in

E. Nieto-Valeiras, E. Ganju, N. Chawla, J. LLorca,
Assessment of slip transfer criteria for prismatic-to-prismatic slip in pure Ti from 3D grain boundary data,
Acta Materialia **262**, 119424 (2024)

The main results of Chapter 5 of this thesis have been submitted for publication in

E. Nieto-Valeiras, A. Orozco-Caballero, M. Sarebanzadeh, J. Sun, J. LLorca,
Assessing prismatic-to-prismatic slip transfer across grain boundaries via high-resolution digital image correlation: when the geometrical criteria fail,
International Journal of Plasticity, (2024)

The main results of Chapter 6 of this thesis have been published in

E. Nieto-Valeiras, S. Haouala, J. LLorca,
On the effect of slip transfer at grain boundaries on the strength of FCC polycrystals,
European Journal of Mechanics - A/Solids **91**, 104427 (2022)

Resumen

Los materiales metálicos suelen ser los materiales estándar para aplicaciones estructurales en ingeniería. Sin embargo, la resistencia de los metales puros es bastante limitada debido al desarrollo de la deformación plástica por deslizamiento de dislocaciones. Se han empleado distintos mecanismos de endurecimiento para crear obstáculos que dificulten el movimiento de las dislocaciones a través de la red cristalina. Los bordes de grano se encuentran entre las barreras más fuertes al deslizamiento de dislocaciones en policristales, desempeñando un papel crítico en sus propiedades mecánicas. Sin embargo, los bordes de grano pueden provocar daños, inducir efectos de tamaño como el efecto Hall-Petch o debilitar el material debido a la irradiación y la fragilización por hidrógeno. Diseñar materiales con bordes de grano resistentes a estos efectos es esencial para alargar la vida útil y la seguridad de los componentes críticos y requiere comprender la interacción entre las dislocaciones y los bordes de grano. Las pruebas experimentales han revelado que, en algunos casos, las dislocaciones pueden transferir deslizamiento al grano vecino a través del borde de grano (*slip transfer*), mientras que en otros bordes de grano se forman apilamientos de dislocaciones (*slip blocking*). Sin embargo, aún no existe un acuerdo general sobre los criterios para predecir el *slip transfer* en materiales policristalinos.

Esta tesis tiene como objetivo analizar los mecanismos de interacción dislocación/borde de grano en policristales metálicos desde el punto de vista experimental y de simulación numérica. Se ha analizado la ocurrencia de *slip transfer/blocking* en policristales delgados de níquel puro (red cúbica centrada en las caras) y titanio puro (red hexagonal compacta). Se han utilizado técnicas experimentales de última generación, como el análisis de trazas de deslizamiento basado en la difracción de electrones retrodispersados, la tomografía de difracción de contraste y la correlación digital de imágenes de alta resolución, para caracterizar la microestructura y determinar las condiciones para el *slip transfer*. En particular, la tomografía de difracción de contraste se empleó para determinar el efecto de la geometría tridimensional de los bordes de grano en el *slip transfer*, y la correlación digital de imágenes de alta resolución se utilizó para tener en cuenta el efecto del estado de tensiones locales alrededor de los bordes de grano. Se utilizó una amplia base de datos de eventos de *slip transfer/blocking* adquiridos en níquel y titanio para validar/desaprobar la precisión de los criterios geométricos de *slip transfer* disponibles en la bibliografía.

Además, se amplió un modelo existente de plasticidad cristalina para incluir el efecto endurecedor de los bordes de grano y la posibilidad de *slip transfer* en el comportamiento mecánico de policristales cúbicos centrados en las cara y hexagonales compactos. Se implementaron con éxito diversos criterios geométricos de *slip transfer* y se utilizaron para simular el efecto del tamaño de grano en la resistencia mecánica de los policristales mediante homogeneización computacional. Las simulaciones se validaron frente a datos experimentales de la respuesta a la tracción de policristales cúbicos y hexagonales encontrados en la bibliografía. Posteriormente, se estudió el efecto del *slip transfer* en la fractura intergranular mediante la inserción de superficies cohesivas en los bordes de grano de láminas policristalinas para determinar el efecto del carácter y la geometría de los bordes de grano en la resistencia y la fractura de policristales metálicos.

Los resultados presentados en el capítulo 2 de esta tesis han sido publicados en

E. Nieto-Valeiras, J. LLorca,
Criteria for slip transfer across grain and twin boundaries in pure Ni,
Materialia **21**, 101303 (2022)

Los resultados presentados en el capítulo 3 de esta tesis han sido publicados en

E. Ganju, E. Nieto-Valeiras, N. Chawla, J. LLorca,
A novel diffraction contrast tomography (DCT) acquisition strategy for capturing the 3D crystallographic structure of pure titanium,
Tomography of Materials and Structures **1**, 100003 (2023)

Los resultados presentados en el capítulo 4 de esta tesis han sido publicados en

E. Nieto-Valeiras, E. Ganju, N. Chawla, J. LLorca,
Assessment of slip transfer criteria for prismatic-to-prismatic slip in pure Ti from 3D grain boundary data,
Acta Materialia **262**, 119424 (2024)

Los resultados presentados en el capítulo 5 de esta tesis han sido enviados para publicación en

E. Nieto-Valeiras, A. Orozco-Caballero, M. Sarebanzadeh, J. Sun, J. LLorca,
Assessing prismatic-to-prismatic slip transfer across grain boundaries via high-resolution digital image correlation: when the geometrical criteria fail,
International Journal of Plasticity, (2024)

Los resultados presentados en el capítulo 6 de esta tesis han sido publicados en

E. Nieto-Valeiras, S. Haouala, J. LLorca,
On the effect of slip transfer at grain boundaries on the strength of FCC polycrystals,
European Journal of Mechanics - A/Solids **91**, 104427 (2022)

Contents

List of Figures

List of Tables

Glossary

Acronym	Definition
AFM	Atomic Force Microscopy
BCC	Body-Centered Cubic
CBS	Circular Backscatter
C-DCT	Conventional Diffraction Contrast Tomography
CRSS	Critical Resolved Shear Stress
CSL	Coincident Site Lattice
DCT	Diffraction Contrast Tomography
DOF	Degrees Of Freedom
EBSD	Electron Backscatter Diffraction
EDT	Euclidean Distance Transform
FCC	Face-Centered Cubic
FFT	Fast Fourier Transformation
FIB	Focused Ion Beam
FN	False Negatives
FP	False Positives
GB(s)	Grain boundary(ies)
GNDs	Geometrically Necessary Dislocations
GROD	Grain Reference Orientation Deviation

Table 1: Recurrent acronyms used throughout this thesis (A-G).

Acronym	Definition
HCP	Hexagonal Close-Packed
HP-DCT	Helical Phyllotaxis Diffraction Contrast Tomography
HRDIC	High-Resolution Digital Image Correlation
LabDCT	Laboratory-scale Diffraction Contrast Tomography
LRB	Lee Robertson and Birnbaum
MFP	Mean Free Path
PCT	Phase Contrast Tomography
RDR	Relative Displacement Ratio
ROI	Region Of Interest
RSS	Resolved Shear Stress
RVE	Representative Volume Element
SEM	Scanning Electron Microscopy
SF	Schmid Factor
SGCP	Strain Gradient Crystal Plasticity
SSDs	Statistically Stored Dislocations
ST-MLRA	Slip Trace Modified Lattice Rotation Analysis
TB(s)	Twin Boundary(ies)
TEM	Transmission Electron Microscopy
TN	True Negatives
TP	True Positives
UMAT	User-Defined Material

Table 2: Recurrent acronyms used throughout this thesis (H-Z).

Symbol	Definition	Reference
$\boldsymbol{b}$	Slip system Burgers vector	Fig. 1.5
Δb	Residual Burgers vector	Sec. 1.3, Eqs. 1.1, 6.15
D	Damage at cohesive surfaces	Fig. 7.1
d_b	Distance to the nearest grain boundary	Sec. 6.3
$\overline{D}_g$	Average grain size	Ch. 6
F1	F1 score	Eq. 4.5
$\boldsymbol{G}$	Orientation matrix	Eq. 6.16
G_C	Energy of the cohesive surface	Sec. 7.2.3
K	Similitude coefficient	Eq. 6.6
K_{ii}	Cohesive surface stiffness constants	Fig. 7.1
K_s	Dislocation storage coefficient	Eqs. 6.5, 6.10
ℓ^α	Dislocation mean free path	Eq. 6.6
$\mathrm{L_{GB}}$	Grain boundary length	Sec. 7.4
LRB	Lee Robertson and Birnbaum parameter	Sec. 1.3, Eq. 1.3
m	Strain rate sensitivity coefficient	Eq. 5.1
m'	Luster Morris parameter	Sec. 1.3, Eqs. 1.4, 6.15
$\boldsymbol{n}$	Slip system normal vector	Fig. 1.5
N	Livingston and Chalmers parameter	Sec. 1.3, Eq. 1.2
$\mathrm{n_{Trs}}$	Number of transparent slip systems per grain boundary	Sec. 7.4
$q^{\alpha\beta}$	Dislocation interaction coefficients	Eqs. 6.3, 6.8
r	Pearson correlation coefficient	Sec. 7.4
SA	Slip activation factor	Sec. 7.4
t	Traction between cohesive surfaces	Fig. 7.1
t_i^0	Stress for damage initiation at the cohesive surface	Sec. 7.2.3
y_c	Critical annihilation distance between dislocations	Eqs. 6.5, 6.10, 6.11
y_e	Annihilation distance between edge dislocations	Eq. 6.11
y_s	Annihilation distance between screw dislocations	Eq. 6.11

Table 3: Recurrent notations used throughout this thesis — Latin symbols.

Symbol	Definition	Reference
α	Grain boundary trace angle	Fig. 1.3
α_x	Angle between grain boundary and loading axis	Sec. 7.4
β	Grain boundary inclination angle	Fig. 4.3 (c)
γ	Angle between incoming slip plane and outgoing Burgers vector	Fig. 1.5
γ	Accumulated plastic slip	Eq. 5.1
$\dot{\gamma}$	Shear strain rate	Eq. 5.1
$\dot{\gamma}_0$	Reference shear strain rate	Eq. 5.1
δ	Angle between incoming Burgers vector and outgoing slip plane	Fig. 1.5
δ	Angle between incoming Burgers vector and outgoing slip plane	Fig. 1.5
δ	Separation between cohesive surfaces	Fig. 7.1
δ_i^f	Maximum separation between cohesive surfaces	Sec. 7.2.3
ε	Applied strain	Ch. 2, 4, 5, 6, 7
ε_{dmg}^0	Strain for damage initiation	Sec. 7.4
φ_1	First Euler angle	Fig. 1.3
ϕ	Second Euler angle	Fig. 1.3
φ_2	Third Euler angle	Fig. 1.3
κ	Angle between incoming and outgoing Burgers vectors	Fig. 1.5
ψ	Angle between incoming and outgoing slip planes	Fig. 1.5
π	Pi	Eq. 6.11
σ_y	Yield strength of a polycrystal	Eq. 6.1
σ_∞	Flow strength of a polycrystal with infinite grain size	Eq. 6.1
θ	Twist angle	Fig. 1.5
Θ	Misorientation angle	Fig. 1.3
τ	Resolved shear stress	Eq. 5.1
τ_c	Critical resolved shear stress	Eq. 6.3
τ_{c0}	Lattice resistance	Eq. 6.8
μ	Shear modulus	Eqs. 6.3, 6.8
ρ	Dislocation density	Eq. 6.6
$\dot{\rho}$	Dislocation density rate	Eqs. 6.4, 6.5, 6.9, 6.10

Table 4: Recurrent notations used throughout this thesis — Greek symbols.

1 Introduction

Metallic materials stand as ideal candidates for many structural applications in the automotive, aerospace, chemical, construction, and biomedical sectors owing to their high stiffness, formability, and ductility. However, the strength of pure metals is very low due to the development of plastic deformation by dislocation slip. Hence, they have to be strengthened by obstacles that hinder dislocation motion.

Grain boundaries (GBs) stand among the strongest barriers to dislocation slip in polycrystals, playing a critical role in their mechanical properties [185]. Dislocations move through the crystal lattice when a metal undergoes plastic deformation by the application of an external load. GBs act as barriers to the motion of dislocations due to the lack of continuity between the lattice planes in neighbor grains, impeding the progress of dislocation motion. The interaction between dislocations and GBs allows to control the mechanical properties of metals, and GB engineering arises as a tool to deliberately manipulate the GB characteristics to enhance the performance of metallic materials. In fact, it is possible to tailor the mechanical properties to meet specific requirements by controlling the grain size, orientation, and distribution.

However, GBs are not just passive interfaces and can be sources of damage in metallic materials. They can act as sites for the initiation and propagation of cracks and voids in the presence of thermo-mechanical loads, leading to the premature failure of metallic components, particularly in the case of mechanical fatigue and/or creep deformation at high temperatures. Thus, understanding the behavior of GBs in the presence of thermo-mechanical loads is critical for designing materials with improved resistance to fatigue and creep [95, 193].

GBs also induce size effects during the plastic deformation of metals, leading to the classical Hall-Petch effect that relates the yield strength with the inverse of the square root of the average grain size [72, 143]. Moreover, metallic with nanoscale grains exhibit improved strength and hardness, as compared with their coarse-grained counterparts, but their strain hardening and ductility are dramatically reduced because dislocation storage within the grains is limited by their small size [43, 101, 174].

GBs also play a crucial role in the response of metallic materials to external factors such as irradiation and hydrogen exposure. In nuclear materials, irradiation can create defects and alter the GB structure, affecting their mechanical properties and integrity [18, 49]. Similarly, hydrogen embrittlement is a phenomenon where hydrogen atoms absorbed by GBs can lead to reduced ductility and catastrophic failure [21, 150]. Designing materials with GBs that are resistant to such effects is essential for ensuring the long-term performance and safety of critical components.

In conclusion, the behavior of GBs is one of the key factors to take into account for the design of metallic materials with improved mechanical properties. GB engineering offers a powerful tool to optimize material performance by tailoring these boundaries to meet specific requirements, and it is an essential aspect of physical metallurgy.

1.1 Plastic deformation by dislocation slip

Dislocation slip is a fundamental mechanism for plastic deformation in metals. Dislocations are line defects characterized by the Burgers vector $\boldsymbol{b}$, which represents the magnitude and direction of the lattice distortion caused by the dislocation. Dislocations move along crystallographic planes driven by the resolved shear stress acting on the slip plane along the slip direction, which is parallel to the Burgers vector [30]. There are three types of dislocations: edge, screw, and mixed dislocations. Edge dislocations are created by the insertion of an extra half-plane of atoms above the dislocation lines, and their Burgers vector is perpendicular to the dislocation line. Screw dislocations do not involve an extra half-plane of atoms, but the atomic planes are misaligned along the dislocation line, creating a spiral or helical pattern, and the Burgers vector is parallel to the dislocation line. Finally, mixed dislocations have components of both edge and screw dislocations [86, 142].

Following experimental observations and theoretical analyses, dislocation slip along crystallographic planes takes place when the shear stresses acting on the slip plane along the slip direction reach a certain critical value, denominated critical resolved shear stress (CRSS). The minimum CRSS in metallic materials is found in the most densely packed slip planes and along the orientations with the largest atomic density in these planes, which vary depending on the crystal lattice [86, 142].

In the case of face-centered cubic (FCC) crystal lattices (characterized by a lattice parameter a), dislocation slip takes place in four $\{111\}$ close-packed planes and three $<110>$ close-packed directions within these planes (Fig. 1.1 (b)). This leads to 12 different slip systems, characterized by the slip plane and the slip direction, which are presented in Table 1.1 and colored according to the active slip plane. Slip along these planes and directions is the primary mechanism for plastic deformation in FCC metals, and the CRSS is the same for all systems.

The hexagonal close-packed (HCP) crystal lattice is characterized by two lattice parameters: the basal plane hexagonal edge length a and the height between basal planes c (see Fig. 1.2 (a)). The c/a ratio has a direct impact on CRSS for dislocation motion along differ-

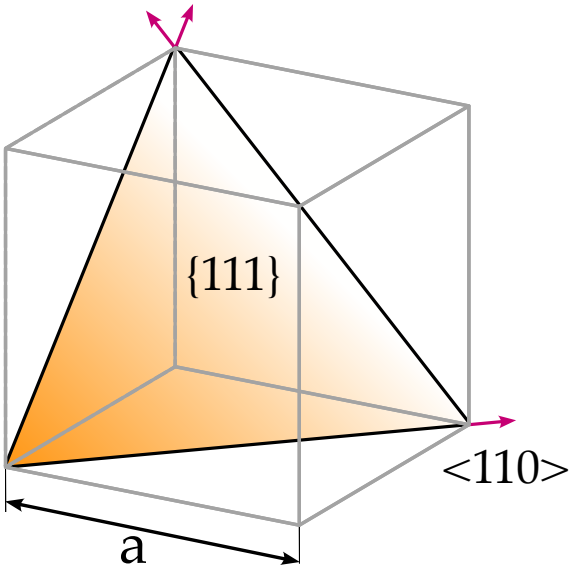

Figure 1.1: Most densely packed slip planes and directions within the FCC unit lattice.

Table 1.1: Slip system notation in FCC metals, indicating the coloring of the four $\{111\}$ slip planes.

Slip system	Plane	Direction
1	$(1\ 1\ 1)$	$[\bar{1}\ 1\ 0]$
2	$(1\ 1\ 1)$	$[1\ 0\ \bar{1}]$
3	$(1\ 1\ 1)$	$[0\ \bar{1}\ 1]$
4	$(\bar{1}\ 1\ 1)$	$[\bar{1}\ \bar{1}\ 0]$
5	$(\bar{1}\ 1\ 1)$	$[1\ 0\ 1]$
6	$(\bar{1}\ 1\ 1)$	$[0\ 1\ \bar{1}]$
7	$(\bar{1}\ \bar{1}\ 1)$	$[1\ \bar{1}\ 0]$
8	$(\bar{1}\ \bar{1}\ 1)$	$[\bar{1}\ 0\ \bar{1}]$
9	$(\bar{1}\ \bar{1}\ 1)$	$[0\ 1\ 1]$
10	$(1\ \bar{1}\ 1)$	$[1\ 1\ 0]$
11	$(1\ \bar{1}\ 1)$	$[\bar{1}\ 0\ 1]$
12	$(1\ \bar{1}\ 1)$	$[0\ \bar{1}\ \bar{1}]$

ent crystallographic directions because the spacing between crystal planes depends on it. The main slip systems in HCP lattices are schematically shown in Fig. 1.2, and the number of independent slip systems and their corresponding slip plane and slip direction families are displayed in Table 1.2.

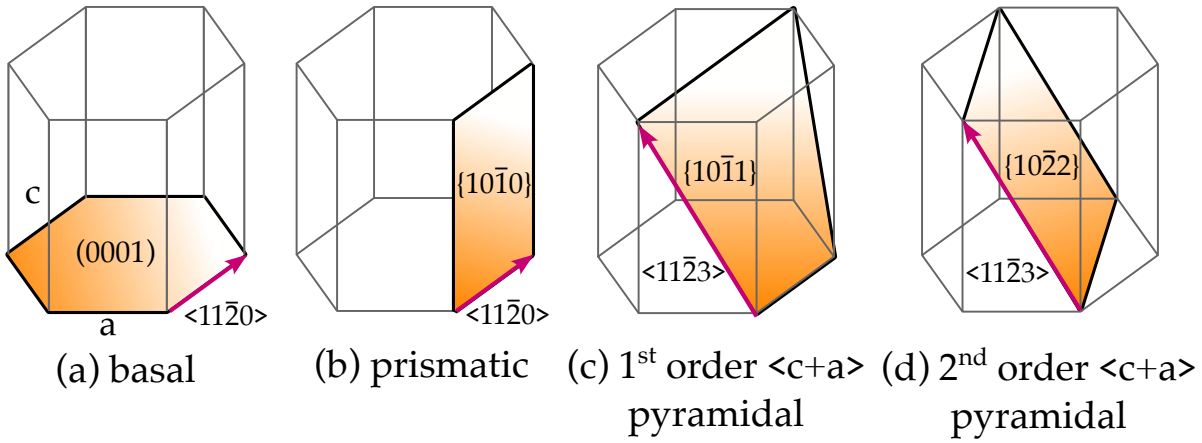

Figure 1.2: Schematic diagram of the main slip systems in HCP lattices.

Table 1.2: Main slip system families in HCP metals.

Slip family	Slip plane	Slip direction	Number of systems
Basal	(0001)	$<11\bar{2}0>$	3
Prismatic	$\{10\bar{1}0\}$	$<11\bar{2}0>$	3
1^{st} order pyramidal <c+a>	$\{10\bar{1}1\}$	$<11\bar{2}3>$	12
2^{nd} order pyramidal <c+a>	$\{10\bar{2}2\}$	$<11\bar{2}3>$	6

1.2 Grain boundaries

1.2.1 Geometrical description of grain boundaries

Polycrystalline materials are composed of an aggregate of single crystals or grains with different orientations. The different grains are separated by GBs, which are disordered regions where the crystallographic orientation abruptly changes from one grain to the next.

A planar grain boundary can be described by five macroscopic degrees of freedom (DOFs) [185]. Three DOFs are related to the relative crystallographic orientation between the neighboring grains, and the remaining two describe the geometry of the GB plane.

As depicted in Fig. 1.3, the crystallographic orientation of each crystal across the GB is determined by three Euler angles $(\varphi_1, \Phi, \varphi_2)$ per crystal. Then, the relative misorientation across the GB can be expressed as an axis-angle rotation that can be uniquely described by three parameters: two for the rotation axis ax determined by its direction cosines and one misorientation angle Θ. The other two remaining parameters deal with the orientation of the GB plane in the three-dimensional space and can be defined by the GB trace angle α and the GB inclination angle through the thickness β.

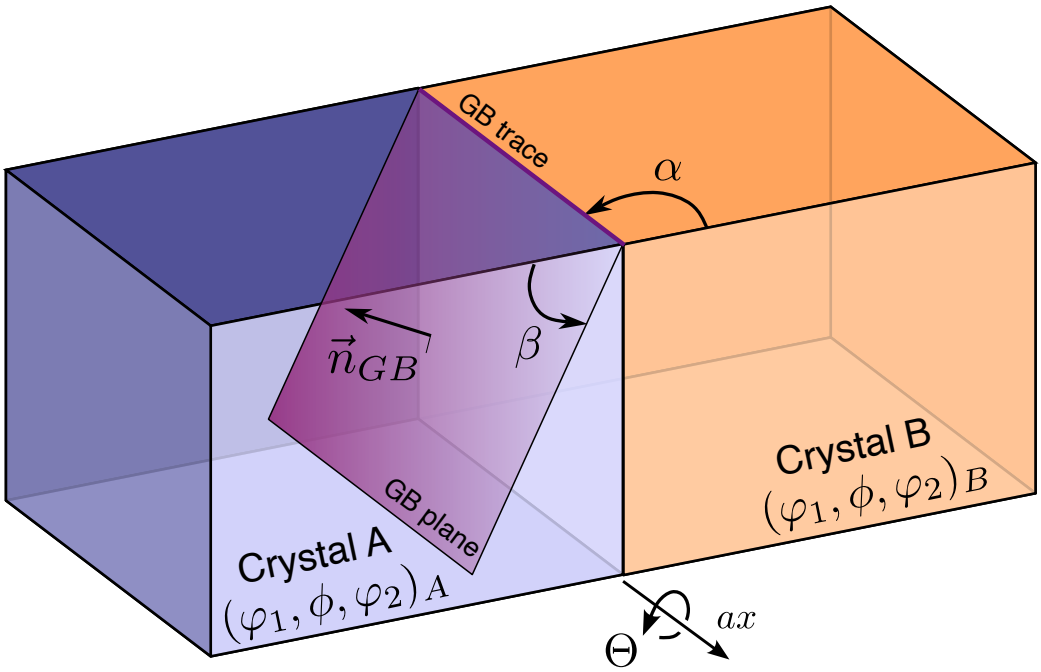

Figure 1.3: Five degrees of freedom to describe a planar GB.

1.2.2 Interactions between dislocations and grain boundaries

Grain boundaries play a key role in the plastic deformation of polycrystals because they constitute physical barriers to dislocation motion [83]. The interaction between dislocations and GBs was reviewed by Bayerschen *et al.* [19], and the most relevant mechanisms of dislocation-GB interactions are schematically illustrated in Fig. 1.4, where A stands for the incoming slip system in the blue grain and B stands for the outgoing slip system in the orange grain across the GB.

Slip transmission from the blue to the orange grain one is not possible in the case depicted in Fig. 1.4 (a) because of the differences in the orientation of the Burgers vector of the dislocations between both slip planes. Thus, the GB behaves as an impenetrable or opaque boundary that impedes dislocation slip to the adjacent grain, leading to the formation of dislocation pile-ups and local stress concentration at the GB. As a result, geometrically necessary dislocations (GNDs) are accumulated at the GB, which induce strong strain gradients in order to preserve the displacement continuity between neighbor grains [58, 85]. This stress concentration induced by the dislocation pile-up at the GB may lead to the activation of dislocation sources in the adjacent grain, thus promoting the emission of dislocations from the boundary [160].

Conversely, if the slip systems across the GB are suitably aligned, dislocations gliding along the slip system A in the blue grain can continue gliding in the slip system B in the orange grain (Fig. 1.4 (c)). Hence, this GB is transparent from the viewpoint of dislocation

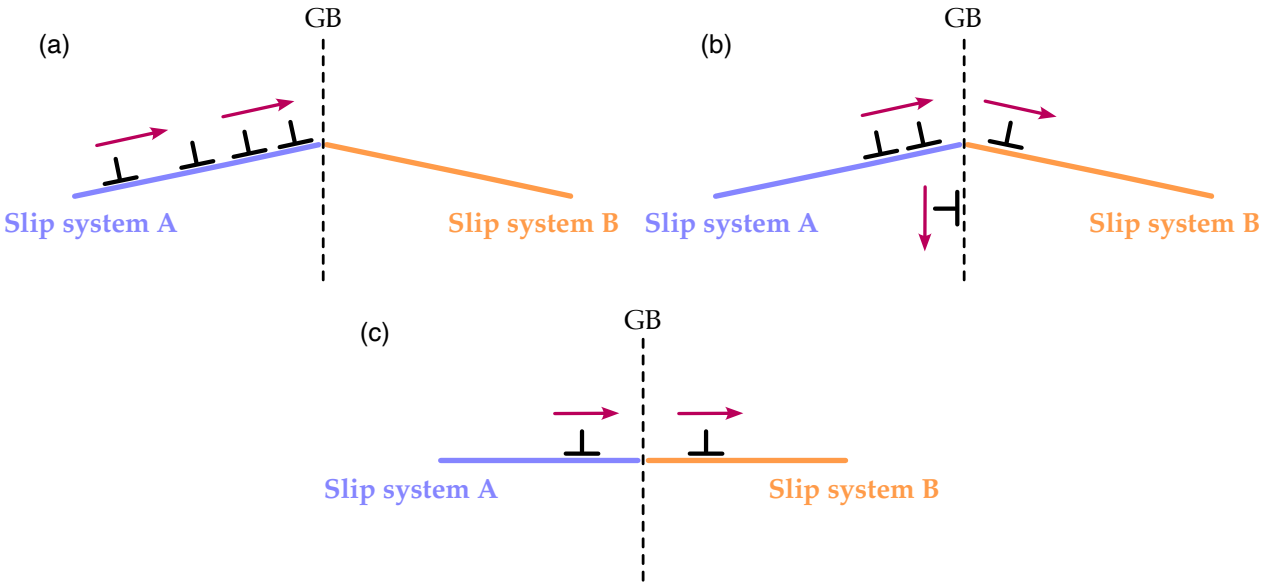

Figure 1.4: Basic mechanisms of dislocation-GB interaction between two active slip systems A and B in adjacent grains separated by a GB. (a) Opaque GB, (b) translucent GB, and (c) transparent GB.

motion and does not lead to any stress concentration [71]. The intermediate scenario is depicted in Fig. 1.4 (b)), which shows a translucent GB. Due to the misalignment between the incoming and outgoing Burgers vectors, slip transfer from the blue to the orange grain is necessarily accompanied by a residual dislocation at the GB to ensure the continuity of the Burgers vector [114]. This process is associated with a certain stress concentration that will depend on the misorientation between the slip planes across the boundary. Moreover, the accumulation of residual dislocations at the GB can also lead to grain boundary sliding and/or to the nucleation of dislocation sources in the adjacent grain.

1.3 Slip transfer criteria: state of the art

There is ample experimental evidence that different GBs present different slip transfer behavior. The empirical observations indicate that slip transfer occurs more easily in low-angle GBs, i.e., when the misorientation angle between adjacent grains is below $\approx 15°$ [149]. Nevertheless, slip transfer is not guaranteed by low-angle GBs, nor is impossible to occur for large GB misorientations.

The geometry of slip across a GB can be schematically described as shown in Fig. 1.5. The incoming slip system in crystal A is characterized by the Burgers vector $\boldsymbol{b}_A$ and the slip plane normal $\boldsymbol{n}_A$, whereas the outgoing slip system in crystal B is determined by the Burgers vector $\boldsymbol{b}_B$ and slip plane normal $\boldsymbol{n}_B$. $\boldsymbol{l}_A$ and $\boldsymbol{l}_B$ stand for the traces of the incoming and outgoing slip planes within the GB plane. This configuration gives rise to a series of angles that describe the geometrical alignment between incoming and outgoing slip systems across the GB. To begin with, the angle κ is the angle between Burgers vectors, and

ψ is the angle between slip plane normals. Next, δ and γ stand for the angles between the incoming Burgers vector and the outgoing slip plane normal and vice-versa, respectively. Finally, θ (often designated as the twist angle) represents the angle between the traces of the incoming ($\boldsymbol{l}_A$) and outgoing ($\boldsymbol{l}_B$) slip planes with the GB plane.

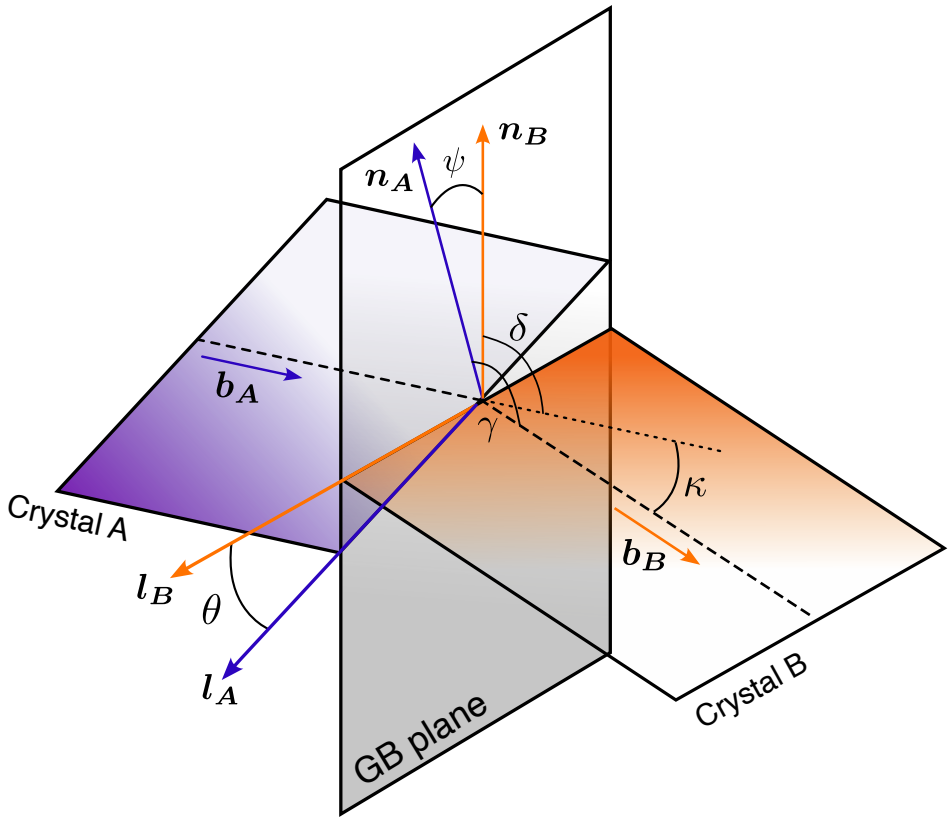

Figure 1.5: Schematic representation of the geometrical alignment between incoming and outgoing slip systems across a GB.

The occurrence of slip transfer across a GB has been extensively studied, and it has been associated with good geometrical alignment between the incoming and outgoing active slip systems [19]. Thus, criteria based on the angular parameters that characterize slip across GBs have been preferred (Fig. 1.5). Several investigations have attempted to define geometrical criteria to predict the likelihood of slip transfer across GBs.

Slip transfer is less likely to take place if the magnitude of the residual Burgers vector left at the GB Δb is very large [70, 71]. Δb is directly associated with the angle κ

$$\Delta b = |\boldsymbol{b}_A - \boldsymbol{b}_B| = 2 \cdot sin(\kappa/2). \tag{1.1}$$

Δb has been extensively used as an indicator for slip transfer when the κ angle between the slip systems is minimum [2, 3, 41, 140]. In that case, the local stress concentration caused by residual dislocations left at the GB is low [71]. Abuzaid *et al.* [2, 3] used a combination of electron back-scattered diffraction (EBSD) and digital image correlation to capture the formation of pile-ups at GB (indicative of slip blocked) or the transmission of

strains across GBs (indicative of slip transfer) in a Ni-based superalloy. Slip transfer was associated with small values of Δb, which seemed to be the best predictor of slip transfer, particularly for coherent twin boundaries where $\Delta b = 0$ was associated with slip transfer via cross-slip. Patriarca *et al.* [140] found a close correlation between the Δb and the local strain change across the GBs in a FeCr body-centered cubic (BCC) alloy. When the residual Burgers vector magnitude was large, the high strains on one side of the GB were paired with low strains across the GB, indicating the difficulties for dislocations to penetrate the interface. Conversely, smooth strain gradients were observed across the boundary when Δb was minimum because the resistance to slip transmission was negligible. Hence, their results suggested that the residual Burgers vector was closely related to the resistance to slip transfer.

Livingston and Chalmers [115] pioneered the use of geometrical criteria to predict the active slip system in a grain adjacent to a dislocation pile-up. This criterion was experimentally determined by means of transmission electron microscopy (TEM) after tensile deformation of several pure Al bicrystals. The geometrical criterion N was defined according to

$$N = \cos\psi \cos\kappa + \cos\gamma \cos\delta. \tag{1.2}$$

This criterion is based on the approximation that the stress state in the adjacent grain, resulting from the pile-ups of the incoming slip system at the GB, is of pure shear stress type. Thus, the shear stresses on the incoming and outgoing slip systems are related by the individual transmission factor, N. Using this approximation, given an incoming slip system A, the slip activation process will favor the operation of the slip system B with the highest N ($0 < N < 1$) in the adjacent grain. This criterion predicted additional (non-primary) active slip systems in the examined Al bicrystals and indicated that the higher N, the larger the probability of operation of an outgoing slip system B alongside the GB. Moreover, the slip traces of slip system B appeared clearly over nearly the entire crystal surface in the few cases where $N > 0.9$ [115]. This provided a more fundamental understanding of the bicrystal deformation process and constituted the first step toward the analysis of polycrystalline deformation.

However, as reviewed by Shen *et al.* [160], the N criterion alone is insufficient to predict the active slip system and more information is required regarding the geometry of the GB and the stress state around it. By means of dynamic TEM experiments performed in stainless steel, they concluded that the outgoing slip plane can be predicted by means of geometric factors that include the geometry of the GB plane, whereas the outgoing slip direction will be that with the maximum resolved shear stress. A year later, Lee, Robertson, and Birnbaum [108] proposed a combined criterion based on *in situ* transmission electron microscopy (TEM) deformation experiments as an extension of the work of Clark *et al.* [41] and Shen *et al.* [160]. They stated that slip transfer will take place under three conditions:

1. The geometrical condition: the angle between the lines of intersection between the active slip planes and the GB (the twist angle θ) should be minimized.
2. The resolved shear stress condition: the resolved shear stress (RSS) acting on the outgoing slip system should be maximized.

3. The residual GB dislocation condition: the Burgers vector of the dislocation left at the GB Δb, and thus the angle κ (Eq. 1.1) should be minimized.

Mathematically, this criterion was expressed as:

$$LRB = \cos\theta \cos\kappa. \tag{1.3}$$

Later, Lee *et al.* [109] proposed that the maximum resolved shear stress criteria and minimum Δb (conditions (2) and (3)) needed to be combined, as they are competitive in nature. This conclusion was also supported by Lim *et al.* [114], who suggested that the slip system with the maximum resolved shear stress may not be activated and could even operate only for a short period of time if Δb is very large.

The LRB factor has been used in previous investigations that indicate that not only a good alignment between the Burgers vectors according to κ is necessary for slip transfer, but also the slip planes must be well-aligned with the GB plane according to θ [26, 73, 154]. Several experimental investigations have revealed that the θ angle may affect the occurrence of slip transfer across GB even though the slip systems are well aligned. For instance, Lee *et al.* [109] performed a TEM-based study in which it was observed that the outgoing slip plane was that with the smallest twist angle in order to accommodate slip in FCC materials. In fact, the twin plane normal and the twist angle can be directly calculated in the case of $\Sigma 3$ annealing twin boundaries in Ni and Genée *et al.* [62], reported that $\theta \approx 0°$ appears as a necessary condition for slip transmission across coherent twin boundaries. Regarding HCP materials, slip blocking was observed in a few GBs in pure Mg, which were well-aligned for slip transfer but $\theta > 60°$ [154]. They measured the GB orientation within the sample by sequential milling with a focused ion beam. This technique has also been used in other investigations [45, 144], but it is destructive and very time-consuming, limiting the number of GBs that can be analyzed.

One of the most accepted criteria for slip transmission is the one proposed by Luster and Morris [118], who performed a detailed TEM analysis of the active slip systems in TiAl. They emphasized the importance of the good alignment between the incoming and outgoing slip systems through the geometric compatibility factor m', defined as

$$m' = \cos\psi \cos\kappa \tag{1.4}$$

which may vary between 0 and 1. $m' = 1$ indicates full compatibility between the active slip systems across the GB because the slip directions and the slip planes are perfectly parallel. Hence, dislocations should be easily transmitted across the GB to the adjacent grain. On the contrary, the slip systems are incompatible when $m' = 0$ because either the slip directions or the slip planes are orthogonal. This criterion has been used to assess slip transfer and blocking across GBs in various investigations [7, 24, 26, 88, 154]. For instance, Wang *et al.* [184] successfully related high m' values with the occurrence of a pop-in effect during indentation tests along selected GBs in pure Nb, which was associated with slip transfer across the GB. Later investigations showed that m' could also be employed to predict the nucleation of mechanical twins at GBs in pure Mg, Mg-rare-earth alloys, and pure Ti [179, 182]. Hémery *et al.* [82] studied slip transfer in a Ti-6Al-4V alloy and

found that the Luster-Morris parameter, combined with high resolved shear stresses in the outgoing slip system, was a good indicator of the probability of slip transfer. Bieler *et al.* [24] studied over 250 GBs to analyze the effect of the misalignment between the slip systems on either side of a GB in pure Al. It was observed that slip transfer across GBs is rare and only convincingly evident when $m' > 0.97$ across low-angle boundaries with $< 15°$ misorientation. Even though it was found that m' was effective when estimating the likelihood of slip transfer, they concluded that the alignment between slip plane normals and directions is not the only important metric to determine the threshold for slip transmission. Furthermore, a study carried out by Alizadeh *et al.* [7] in pure Al GBs by means of conventional slip trace analysis revealed that slip transfer was very likely to occur if the residual Burgers vector was below $0.3b$ and the Luster-Morris parameter was higher than 0.9. Moreover, the ratio of $m'/\Delta b$ also presented a threshold above which slip transfer was very probable.

The validity of these geometrical slip transfer criteria has been assessed in recent years thanks to the information provided by EBSD in combination with slip transfer/blocking evidence at GBs from slip trace analysis in the scanning electron microscope (SEM). The slip traces left by the active slip systems on the grain surface can be observed by SEM imaging. The theoretical orientation of the slip traces in each grain can be obtained from the grain orientation before deformation provided by EBSD. Thus, the active slip plane can be identified by comparing the orientation of the slip traces observed via SEM imaging with the theoretical slip traces of the possible slip systems obtained by EBSD.

This experimental strategy does not indicate the active slip system when several slip systems with different slip directions share the same slip plane (such as FCC lattices or basal slip in HCP lattices). Thus, the slip system that presents the highest resolved shear stress on the slip plane is assumed to be active. This is normally assessed through the Schmid factor (SF), a geometrical parameter that gives the ratio of the resolved shear stress on the slip plane along the slip direction to the applied stress. The maximum resolved shear stress occurs when both the slip plane and the slip direction are oriented at $45°$ to the applied stress, and thus, the maximum SF equals 0.5.

Slip trace analysis in combination with EBSD and the assumption that the slip system with the highest SF is active has been employed in different investigations to assess slip transmission and slip activity in Al [7, 24, 26], Ni-based superalloys [62, 169], Ti and Ti alloys [70, 82, 179, 182], and Mg and Mg alloys [35, 88, 154, 200]. According to these investigations, slip transfer is associated with low misorientation angles between adjacent grains and also with low values of the residual Burgers vector, Δb, and high values (close to 1) of the N, and m' compatibility factors. Nevertheless, a non-negligible number of instances of slip blocking was reported in all cases where slip transfer should occur because the incoming and outgoing slip systems showed good alignment. And vice versa, slip transfer was sometimes found when the incoming and outgoing slip systems were not well aligned. These inconsistencies may be caused by the limitations of EBSD-based slip trace analysis:

1. *Slip traces can only be identified for slip systems that lead to a slip trace on the specimen surface.* Thus, slip bands will not appear in the grain surface if the Burgers vector of the active slip system is parallel or nearly parallel to the sample surface.

2. *This method can only identify the active slip plane, not the slip direction.* There are three different slip directions for each $\{111\}$ plane of the FCC lattice as well as three different slip directions in the (0001) basal planes of the HCP lattice. In addition, the second-order pyramidal slip systems in the HCP lattice comprise six $\{10\bar{1}\bar{2}\}$ pyramidal planes with two possible $<11\bar{2}3>$ directions each. The slip system with the highest SF is assumed to be active among the different possibilities. This may be a reasonable assumption for FCC crystals, in which plastic deformation is rather isotropic, but it is not guaranteed and may be far away from reality in HCP metals, which present a large plastic anisotropy during deformation. This could lead to the activation of a different slip system from that with the highest global SF and even to the activity of several slip systems within the same slip plane [102, 119, 201].

   Lately, complementary techniques have developed to solve this issue, such as the slip trace modified lattice rotation analysis (ST-MLRA) [190] or the relative displacement ratio (RDR) [39]. The ST-MLRA technique tracks the crystal lattice rotation induced by slip after plastic deformation by means of EBSD. The crystallographic orientation of the grain after deformation is compared to the theoretical rotation of the crystal caused by slip along the different slip directions that share the same slip plane, and the actual slip plane(s) can be identified. This strategy was recently employed by Sarebanzadeh *et al.* [154], who identified the active basal slip system(s) in pure Mg after tensile deformation. Using this method, multiple basal slip could be identified for grains with coarser grain sizes, whereas single slip was dominant for small grain sizes. Moreover, the slip system with the highest SF was not active in $\approx 30\%$ of the grains, and hence, the basal slip system with the highest SF cannot be assumed to be the only active slip system in Mg.

   Alternatively, the RDR method uses high-resolution digital image correlation to determine the ratio between the x and y components of the displacement at both sides of a slip band. They are compared to the ratio between the x and y components of the different theoretical Burgers vectors of the slip systems in the slip plane to identify the active one [39]. This method has been successfully employed to identify the active slip system in several works [166, 189], yet requires the presence of sharp and discrete slip traces.

3. *Lack of information about the GB inclination beneath the sample surface.* The conventional slip trace analysis technique is surface-based, and thus, it can only determine the GB trace angle α but not the GB inclination β (Fig. 1.3). The twist angle θ (see Fig. 1.5) is directly related to the GB plane geometry, so its effect on slip transfer can only be assessed by 3D characterization techniques except for special GBs such as twin boundaries, where the parent/child orientation relationship is well-known.

   The 3D GB geometry has to be determined to overcome this limitation for general GBs. This can be achieved by serial sectioning via mechanical polishing or focused ion beam (FIB) milling, and this technique has been used to assess the role of the twist angle on slip transfer during deformation in Mg and Mg alloys [154, 200]. Nevertheless, this strategy is rather time-consuming, and only a limited number of GBs can be analyzed. Given the experimental difficulties in measuring the GB orientation

through the thickness, several studies have assumed that GB is perpendicular to the sample surface [38, 62] to study the effect of θ on the likelihood of slip transmission. However, this hypothesis may lead to large errors in the evaluation of θ [62].

4. *Lack of information about the local stress state after deformation* which may be very different from the global stress state induced by the external forces. In this context, high-resolution digital image correlation (HRDIC) appears as a powerful tool to quantify strain heterogeneity in plastically deformed polycrystalline materials. Several works have attempted to correlate the dislocation-GB interactions with the plastic strain heterogeneity at the GB neighborhoods via HRDIC. They have attempted to correlate the classical geometrical slip criteria with the pile-up stresses and the slip transfer behavior observed via HRDIC. Abuzaid *et al.* [2] concluded that higher strains across some GBs in a Ni-based superalloy with low Δb were associated with lower GB resistance against slip transfer while lower strains across GBs with high Δb were attributed to higher resistance against slip transfer. The shear strain maps also revealed cross slip in a large number of $\Sigma 3$ GBs with $\Delta b \approx 0$. Sperry *et al.* [167] correlated the pile-up stresses observed at GBs in a Ni-based superalloy with the occurrence of slip transfer across GBs and did not observe clear correlations between GB misorientation or the m' factor with the GB pile-up stress. Harte *et al.* [79, 80] observed the slip band characteristics and the local deformation mechanisms at the microscale level in a precipitation-strengthened Ni-based superalloy via HRDIC. They were able to quantify the number of active slip planes, slip planarity, the presence of cross slip, slip band bifurcation, slip band fading towards a GB, and slip band impingement upon a GB. These investigations concluded that the high slip intensity and slip band impingement on GBs create diffuse strain regions, causing local hardening.

   The heterogeneity in the plastic strain accommodation at GBs was observed through HRDIC in AZ31 Mg alloy by Orozco *et al.* [136] and Yavuzyegit *et al.* [191], where a large extent of the deformation was accommodated at GBs whereas lower plastic strain was accommodated by basal slip in the bulk. Both investigations agreed that there is very strong evidence that the local stresses have a major effect on both slip activity and twinning. [65] performed an HRDIC analysis of the strain transfer phenomena across GBs in TiAl alloys, where slip transfer was observed at low-angle GBs, as extensively reported in the literature. Nevertheless, they observed a different strain transfer mechanism at certain high-angle GBs, where the crystal lattice rotated locally to geometrically restore a compatible deformation across the GB. A region of accumulated slip was found perpendicular to the active slip plane in the adjacent grain across the GB due to slip band impingement. The slip gradients through the boundary enabled a localized lattice rotation that accommodates the shear strain in the incoming band, preventing the build-up of interfacial stresses. This strain transfer mechanism could only be detected after large deformations, unlike slip transfer, which is often observed at the onset of plastic deformation.

   Thus, HRDIC can provide extra information about the local plastic strains near GBs that can be used to elucidate other factors –besides good alignment– that control slip

transfer at GBs. Due to the limited number of HRDIC investigations on slip transfer, the local stresses are not considered in the slip transfer criteria, which nowadays rely only on the geometrical alignment of the slip systems across the boundary.

1.4 Mesoscale modeling of grain boundaries

Numerical simulations of the mechanical behavior of polycrystals have progressed rapidly in recent years through the combination of computational homogenization and crystal plasticity constitutive models [158]. This strategy is able to determine the effective properties of a polycrystal by solving a boundary value problem of a microstructural representative volume element (RVE) of the microstructure under homogeneous boundary conditions. Normally, algorithms based on either the finite element method or the fast Fourier transform are used to solve the boundary value problem.

An RVE is a statistical representation of the microstructure of a polycrystal, usually described by the grain size and shape distributions and the crystallographic orientations of the single crystals. RVEs have to be large enough to provide an accurate statistical representation of the polycrystalline microstructure that leads to effective properties that are independent of the size of the RVE. The RVE discretizations can be classified according to the finite element type employed for meshing the microstructure geometry into voxel-based (hexahedral elements) and tessellated (tetrahedral elements) RVEs. Traditionally, the polycrystals have been commonly discretized by voxels or cubic elements, which generally provide higher accuracy and convergence rates. However, as shown in Fig. 1.6 (a), this discretization leads to a stair-stepped appearance at GBs. Conversely, Voronoi tessellation consists of a subdivision of the 3D space into convex polyhedra that intersect at their flat boundaries. Hence, tetrahedral elements can more naturally adapt to curved and irregular surfaces providing a smoother interpolation of the GB geometry, as shown in 1.6 (b). For this reason, when comparing simulation results to experimental observations of GBs, using tetrahedral elements can lead to a closer alignment in terms of surface geometry and appearance. However, Voronoi tessellations are not always able to reproduce the actual grain size distribution, and weighted Voronoi tessellations are used instead.

Crystal plasticity models are based on the multiplicative decomposition of the deformation gradient, $\mathbf{F}$, into its elastic ($\mathbf{F^e}$) and plastic ($\mathbf{F^p}$) components as follows,

$$\mathbf{F} = \mathbf{F}^e \cdot \mathbf{F}^p \tag{1.5}$$

where $\mathbf{F^p}$ is called the intermediate or relaxed configuration. The velocity gradient can be decomposed as

$$\mathbf{L} = \dot{\mathbf{F}} \cdot \mathbf{F^{-1}} = \mathbf{L^e} + \mathbf{F^e} \cdot \mathbf{L^p} \cdot \mathbf{F^{e^{-1}}} \tag{1.6}$$

where $\dot{\mathbf{F}}$ represents the total derivative of the deformation gradient with respect to time. Writing $\mathbf{L^e}$ and $\mathbf{L^p}$ in the form of Eq. 1.6 leads to:

$$\mathbf{L^e} = \dot{\mathbf{F}}^\mathbf{e} \cdot \mathbf{F^{e^{-1}}}, \ \mathbf{L^p} = \dot{\mathbf{F}}^\mathbf{p} \cdot \mathbf{F^{p^{-1}}}. \tag{1.7}$$

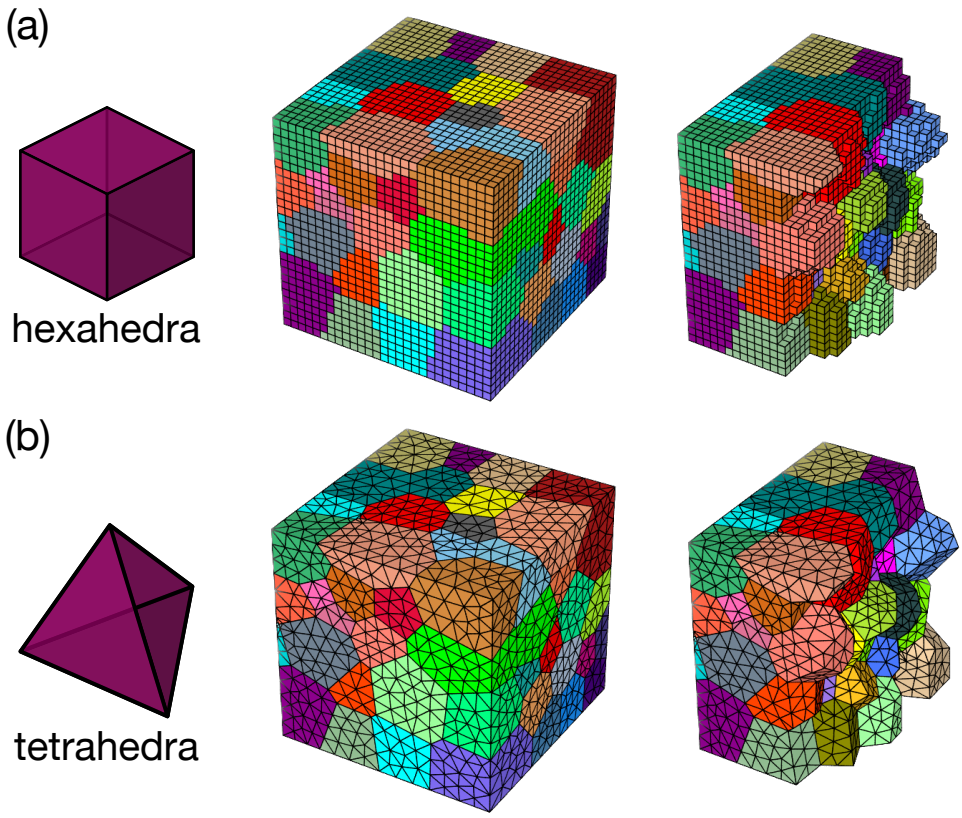

Figure 1.6: Different RVE discretizations for the same microstructure with 100 equiaxed grains generated with the open-source software Neper [146]. (a) RVE discretized with hexahedral or voxel elements. (b) RVE discretized with tetrahedral elements.

The evolution of the plastic deformation gradient $\mathbf{F}^{\mathrm{P}}$ is assumed to arise only from dislocation slip. Thus, the rate of the plastic velocity gradient $\mathbf{L}^{\mathrm{P}}$ in a grain depends on the sum of the slip rates $\dot{\gamma}^{\alpha}$ from all the slip systems α according to

$$\mathbf{L}^{\mathrm{P}} = \sum_{\alpha} \dot{\boldsymbol{\gamma}}^{\alpha} (\boldsymbol{s}^{\alpha} \otimes \boldsymbol{m}^{\alpha}) \tag{1.8}$$

where $\mathbf{s}^{\alpha}$ and $\mathbf{m}^{\alpha}$ denote the unit vectors in the slip direction and in the perpendicular direction to the slip plane, respectively.

Crystal plasticity models usually use phenomenological expressions to define the slip rates and the evolution of the internal variables. The evolution of plastic slip in a slip system α is commonly defined by a power-law dependency according to

$$\dot{\gamma^{\alpha}} = \dot{\gamma_0} \left(\frac{|\tau^{\alpha}|}{\tau_c^{\alpha}} \right)^{\frac{1}{m}} sgn(\tau^{\alpha}) \tag{1.9}$$

where $\dot{\gamma_0}$ stands for the reference shear strain, m is the strain rate sensitivity parameter, ${\tau_c}^{\alpha}$ is the CRSS, and τ^{α} is the resolved shear stress on the slip system α. The latter can be

expressed as the projection of the Piola-Kirchhoff stress, $\mathbf{S}$, on the current slip system α, given by

$$\tau^{\alpha} = \mathbf{S} : (\mathbf{s}^{\alpha} \otimes \mathbf{m}^{\alpha}) \tag{1.10}$$

The boundary conditions applied to the RVE constitute a crucial aspect of full-field computational homogenization. Periodic boundary conditions are often applied because they reproduce the mechanical behavior of an infinite media constructed by a periodic arrangement of the RVE, assuming that it deforms as a jigsaw puzzle.

Nevertheless, the standard crystal plasticity models assume that GBs are transparent for slip transfer, and thus, the effect of GBs on the mechanical behavior of polycrystals has not been usually considered. Two strategies have been employed to account for the effect of GBs in crystal plasticity simulations through the increase of dislocation density near GBs: strain gradient crystal plasticity (SGCP) and physically based crystal plasticity.

The effect of the plastic heterogeneities in the mechanical response of a crystal was first rationalized by Nye and Ashby [9, 133] as a result of the interaction between statistically stored dislocations (SSDs), which evolve from random trapping processes during plastic deformation, and geometrically necessary dislocations (GNDs) induced by the presence of plastic strain gradients. The contribution of GNDs depends on the grain size and concentrates at GBs, whereas the density of SSDs is size-independent. Other theoretical approaches also provided a rational explanation of the Hall-Petch law [72, 143] with a grain representation formed by a soft core surrounded by a hard shell around the GB [83, 96]. From the modeling viewpoint, the most common approach to account for the effect of plastic strain heterogeneities in the material response is by introducing the influence of some plastic strain gradient measure in the constitutive equation, leading to the so-called strain gradient plasticity. Thus, strain gradient crystal plasticity simulations can account for the effect of GBs through the density of GNDs generated near the boundaries due to deformation incompatibility between grains with different crystallographic orientations. Different investigations have used this approach to analyze the effect of grain size on the strength of polycrystals [4, 17, 20, 40, 53, 105]. A recent investigation carried out by Haouala *et al.* [77] predicted the effect of grain size on the flow stress of various FCC polycrystals by means of strain gradient crystal plasticity and fast Fourier transformation (FFT) homogenization. Even though these simulations could capture the Hall-Petch effect on the flow stress due to the generation of GNDs, these simulations assume that all GBs behave as fully opaque to dislocations, so the slip transfer phenomenon at low-angle GBs is not taken into account.

Physically-based crystal plasticity models introduce the effect of GBs through the increase of dislocation density near the GB due to the accumulation of dislocations. In particular, the model developed by Haouala *et al.* and Rubio *et al.* for FCC polycrystals ([78], [151]), succeeded in predicting the grain size effect on the mechanical response of Cu, Al, Ag, and Ni polycrystals. The mechanical behavior of the crystals was modeled by a dislocation-based, rate-dependent crystal plasticity model in which the hardening of the slip systems follows the Taylor model [175]. The dislocation generation and annihilation in each slip system were controlled by a modified Kocks-Mecking model [97], which took into account the distance to the nearest GB in each slip system, so the dislocation density

increased near GBs. Interestingly, despite this model was able to capture the Hall-Petch effect in polycrystals, the predictions overestimated the strength of the polycrystals when the average grain size was < 20 μm. It was argued that the differences between experimental data and simulation results arose because all GBs were assumed to be opaque to dislocations. Haouala *et al.* updated this dislocation-based crystal plasticity model in order to account for slip transfer in pure Al bicrystals [76]. Different bicrystal orientations were studied in grains oriented for single and double slip, including fully transparent, fully opaque, and partially transparent GBs in the simulations. The addition of the slip transfer criteria in the model led to stress relaxation at the GB when it was suitably oriented for slip transfer ($m' > 0.95$), whilst high stress and dislocation densities were still observed when the alignment was poor.

1.5 Objectives

The present thesis aims to provide a quantitative understanding of the effect of grain boundaries (GBs) on the mechanical properties of metallic polycrystals through a combination of experiments and numerical simulations. From the experimental viewpoint, the experimental evidence has not yet provided robust criteria that can accurately predict slip transfer in polycrystalline materials due to the existence of a non-negligible number of outliers that do not follow the predictions from the classical geometrical criteria. These limitations are associated with the difficulties of assessing the actual active slip system, the GB geometry in 3D, and the local stress state. From the simulation viewpoint, the most widely used strategy to model polycrystal deformation is based on crystal plasticity simulations, which usually assume that all the GBs are transparent. Recent works have assumed that all GBs are opaque to predict the flow stress of polycrystals [76, 77], but models that include slip transfer and blocking are not available.

These limitations have been addressed as follows:

1. Experimental analysis of slip transfer was performed in pure Ni (FCC) and pure Ti (HCP) thin foils to avoid the effect of alloying elements or second phases in the dislocation-GB interactions. A large number of GBs were analyzed after plastic deformation, and the occurrence of slip transfer/blocking was registered. In order to overcome the main limitations of the standard slip transfer analysis procedures, the experiments were performed through a combination of different techniques, such as EBSD-based slip trace analysis, laboratory-scale diffraction contrast tomography (LabDCT), and high-resolution digital image correlation (HRDIC). LabDCT was employed to include the effect of 3D GB geometry on slip transfer, and HRDIC was used to account for the effect of the local stress state around GBs. The large and accurate database of slip transfer/blocking events was used to validate/disprove the accuracy of the geometrical criteria for slip transfer across GBs available in the literature.

2. An existing crystal plasticity model [76] was extended to include the effect of slip transfer on the mechanical behavior of FCC and HCP polycrystals. Different geometrical slip transfer criteria were successfully implemented and provided better agreement against experimental data of the tensile response of well-annealed polycrystals found in the literature. Subsequently, the effect of slip transfer on intragranular fracture was studied through the insertion of cohesive surfaces at the GBs of thin foil RVEs.

This thesis is structured as follows. After the introduction, the experimental work is presented in Chapters 2-5. Chapter 2 deals with the experimental analysis of slip transfer in pure Ni. Chapter 3 shows the potential of the LabDCT technique to assess the microstructure of polycrystals in 3D. Chapters 4 and 5 present the slip transfer analysis in pure Ti introducing the effect of 3D GB geometry through LabDCT (Chapter 4), and of local stresses through HRDIC (Chapter 5). The modeling part of this work is presented in Chapters 6 and 7. Chapter 6 presents the extension of the dislocation-based crystal plasticity model to account for slip transfer at GBs in FCC and HCP materials and the

validation of the simulations against experimental data. Chapter 7 presents the workflow to include intragranular fracture in the crystal plasticity simulations and the influence of GBs in damage nucleation and propagation. Finally, the main conclusions and the future work and perspectives are summarized in Chapter 8.

2 Slip transfer at grain boundaries in Ni

2.1 Introduction

The microstructure of annealed Ni polycrystals presents two types of grain boundaries: regular GBs and twin boundaries (TBs). The presence of annealing twin boundaries provides more obstacles for dislocation glide, making plastic deformation more challenging. As reported by some works, TBs can have a strong effect on the localization of plastic deformation that can lead to premature fatigue crack initiation in Ni-based superalloys [168, 170, 195]. Annealing twins in nickel (Ni) exhibit a distinctive $60°$ rotation around the $<111>$ axis, creating a fixed crystallographic relationship between the twin and the matrix. These twins, which are essentially $\Sigma 3$ GBs, are induced by the low stacking fault energy in Ni and appear during solidification and annealing. TBs are low-energy GBs, and thus, they are thermodynamically favorable in comparison with regular GBs.

The matrix-twin interface in TBs can be coherent or incoherent [28, 138, 164]. Coherent TBs maintain a consistent crystallographic orientation with the Ni matrix, resulting in a seamless lattice alignment with mirror symmetry across the boundary. The continuous alignment between the atomic planes across a coherent TB typically results in straight-sided bands that run across grains (see twin 1 in Fig. 2.1). These bands have a twinned orientation relative to their neighboring grain, and the parallel boundaries coincide with a $\{111\}$ twinning plane. In contrast, incoherent TBs appear at the twin ends when the annealing twins do not sufficiently grow to go through the entire parent grain size. As shown in Fig. 2.1, the perpendicular segment that joins the two coherent parallel TBs in twin 2 is incoherent with the lattice matrix and leads to a high lattice misfit and high boundary free energy.

Slip transfer in Ni-based superalloys has been analyzed in several investigations. A combination of EBSD and HRDIC was employed by Abuzaid *et al.* [2] to capture the formation of pile-ups at GBs (indicative of slip blocking) or the transmission of strains across the GB (indicative of slip transfer). This latter behavior was associated with small values of Δb, which seemed to be the best predictor of slip transfer, particularly for coherent TBs where $\Delta b = 0$ was associated with slip transfer via cross-slip. Genée *et al.* [62] analyzed

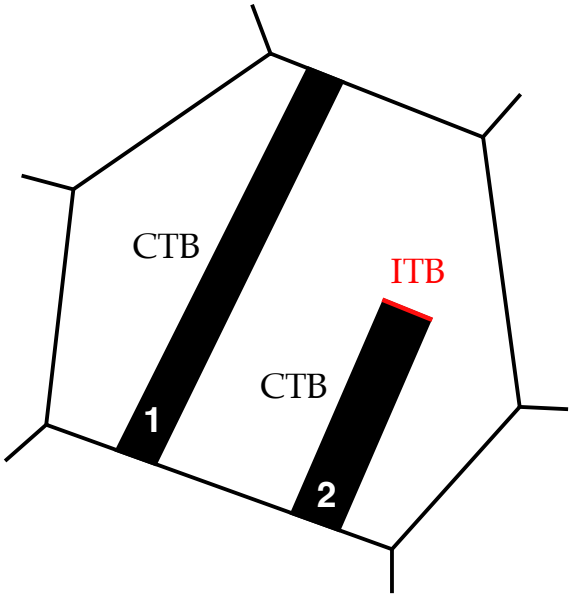

Figure 2.1: Schematic representation of two annealing twins in a Ni grain, where twin 1 is composed of two parallel coherent TBs (CTB) and twin 2 is composed of two parallel coherent TBs (CTB) and one incoherent TB (ICB).

slip transfer in another Ni-based superalloy using EBSD and concluded that the necessary condition for slip transfer at coherent TB was given by θ = 0° (as opposed to the other possibility θ = 60°). Regarding regular GB, they observed that slip transfer was favored by small values of κ and ψ. They could not, however, provide a criterion because of the experimental scatter, which was attributed to the influence of the twist angle θ, which cannot be determined from the EBSD information for regular GBs. Finally, Sperry *et al.* [167] also combined EBSD with HRDIC to study slip transfer in another Ni-based superalloy. They concluded that slip transfer in regular GBs was associated with low misorientation angles, and it was maximum when $m' = 0.78$ in twin boundaries.

These investigations on slip transfer in various Ni-based superalloys have not provided a quantitative unified geometrical criterion, possibly due to the choice of different slip transfer criteria and the differences between the alloys used in each investigation. Moreover, the strengthening effect provided by the alloying elements in Ni-based superalloys hinders the development of slip bands compared to pure Ni, where larger datasets of slip blocking/transmission events can be obtained.

To overcome the limitations of previous investigations, slip transfer/blocking was analyzed in more than 200 regular and twin boundaries of pure Ni foils. The standard conventional slip trace analysis workflow was employed as a starting point for the experimental slip transfer assessment. The objective was to rationalize the previous results obtained in Ni-based superalloys and to provide robust geometrical criteria for slip transfer that can be later incorporated within the framework of crystal plasticity simulations.

2.2 Material and experimental techniques

Slip transfer across GBs and TBs was analyzed in high purity (99.999%) Ni foils of 1 mm in thickness manufactured by rolling, which were purchased from Goodfellow. Two dogbone micro-tensile specimens with a central gauge section of 6×2 mm^2 were manufactured by electro-discharge machining (Fig. 2.2), with the tensile axis oriented at 0° and 45° from the foil rolling direction.

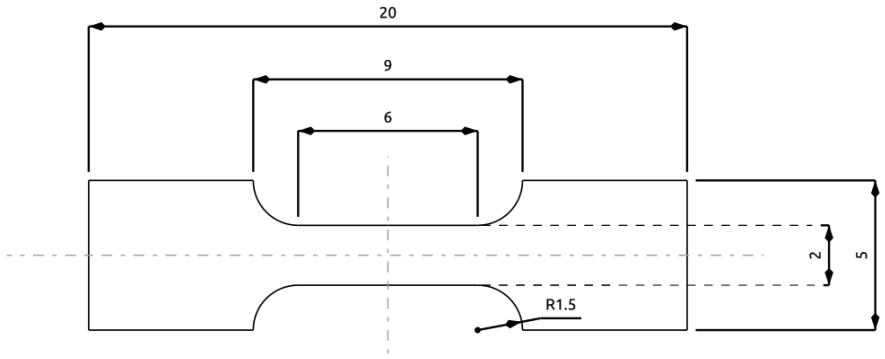

Figure 2.2: Dogbone tensile specimen of Ni. dimensions in mm.

The as-received foil was manually polished with synthetic cloths and 6-3-1 μm diamond paste and etched with Kalling's 2 reagent to reveal the microstructure (Fig. 2.3). The average grain size was 186 ± 31 μm. The as-received microstructure was irregular with wavy GBs, and thus the samples were heat treated to promote grain growth and homogenize the grain shape. To this end, they were encapsulated in quartz tubes filled with high-purity Ar (to prevent oxidation) and annealed at 800 °C for 30 minutes in a tubular vacuum furnace. EBSD maps of the gauge section were obtained after metallographic preparation of the surface of the samples by manual grinding followed by electropolishing using a nitric acid-methanol solution (20% volume of HNO_3) at -30°C and 20 V. Four micro indentations were placed in the central region of the gauge to ease the orientation and alignment of the samples inside the microscope.

EBSD maps were acquired at the upper and bottom surfaces of the gauge length of the sample. The crystallographic orientations were obtained in a FEI Helios NanoLab 600i dual-beam microscope equipped with an Oxford Instruments EBSD detector. The whole gauge length was mapped with 3×5 overlapping maps, followed by stitching in AZtec. The EBSD maps were acquired at 20 kV and 2.7 nA, with a step size of 3.4 μm, in order to accurately resolve the microstructural features. The overall quality of the EBSD maps was above 95% indexing. The maps were post-processed with the MTEX Matlab Toolbox [14] with a grain boundary misorientation threshold of $5°$.

The samples were tested *ex-situ* under uniaxial tension in a Kammrath and Weiss microtensile testing machine using a 10 kN load cell up to $\approx 5\%$ strain at a strain rate of $\approx 10^{-3}$ s^{-1}. The micro tensile test of the sample along the rolling direction is plotted in Fig. 2.4.

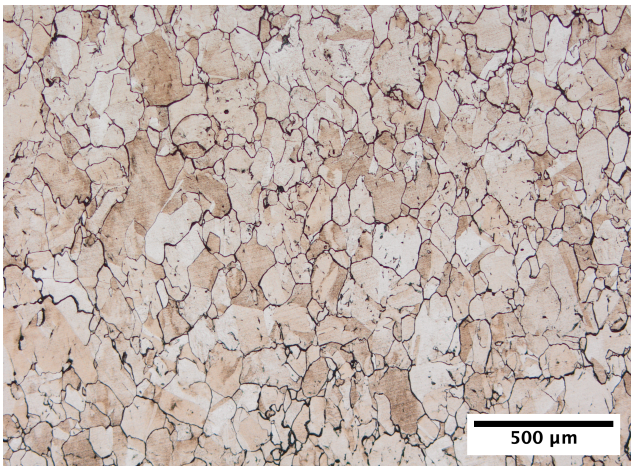

Figure 2.3: Microstructure of the as-received Ni foil, after metallographic preparation and chemical etching with Kalling's 2 reagent.

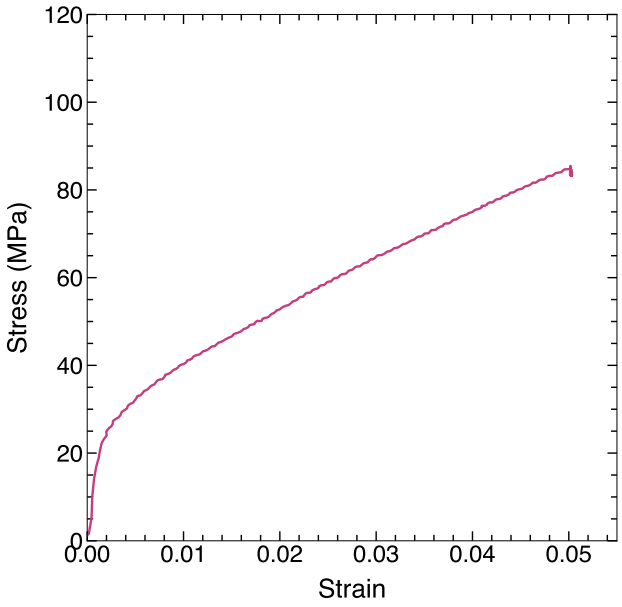

Figure 2.4: Stress-strain curve of the Ni sample deformed along the rolling direction (Fig. 2.5(a)).

SEM imaging was performed after deformation all over the sample surface employing the circular backscatter detector (CBS) to obtain the optimum balance between brightness and contrast to resolve slip traces and identify slip transfer/blocking across GBs. The active slip systems in the grains after deformation were identified by means of conventional slip trace analysis [7, 24]. This technique compares the spatial orientation of the theoretical slip bands calculated from the crystal orientation before deformation (obtained by EBSD) with the experimental ones shown by SEM. The theoretical slip traces were calculated from the EBSD crystal orientations with a Matlab code [24]. In the case of Ni, slip takes place on the $\{111\}$ close-packed planes along the $<110>$ close-packed directions, which results in

12 possible slip systems, as depicted in Table 1.1. Since each of the directions is common to two $\{111\}$ planes, three possible slip systems exist within the four possible slip planes. The deviations in the orientations between the theoretical and the experimental slip traces were always $< 5°$.

2.3 Results and discussion

The EBSD maps of the Ni foils after annealing revealed random texture and a very wide grain size distribution comprised of very large grains (of the order of mm) and clusters of smaller grains (Fig. 2.5). The average grain size was 240 ± 250 μm. In addition, many annealing twins were found throughout the microstructure. There were no significant differences between the samples mechanized at $0°$ and $45°$ from the rolling direction, and hence, no further distinction is made between both specimens

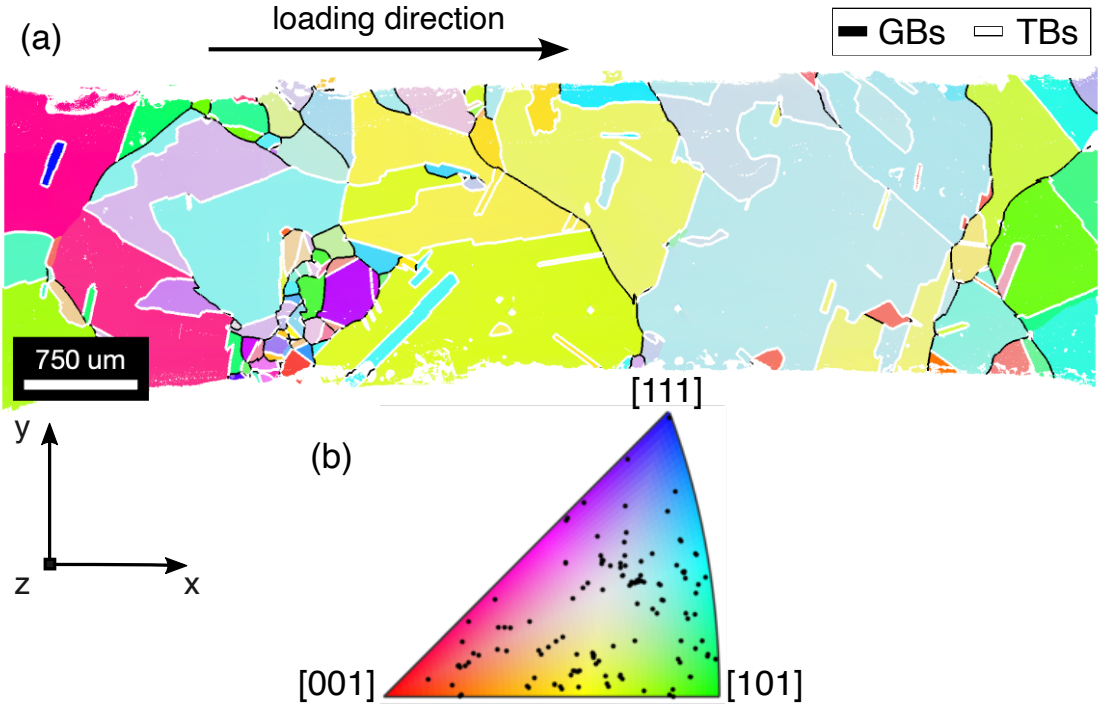

Figure 2.5: (a) EBSD map of the surface of the dogbone specimen parallel to the rolling direction. TBs (which are associated with a misorientation angle Θ of 60°) are drawn with white lines, while regular GBs are drawn with black lines. (b) Inverse pole figure with respect to the z axis, where each grain mean crystallographic orientation is represented by a black dot.

Slip transfer was analyzed in more than 200 GBs. After deformation and inspection of the slip traces in each grain, GBs were classified into two groups: boundaries where slip transfer was convincingly observed and boundaries where slip transfer was not observed. Convincing slip transfer was considered when the incoming and outgoing slip traces across a GB were continuous and clearly correlated, while negligible topography along the GB was observed, indicating relatively homogeneous deformation between the grains (Figs.

2.6 (a), (c) and (d)). Furthermore, the large number of annealing twins promotes the activation of the slip parallel to the TB in the so-called parallel slip configuration near TB [168, 169] (Fig. 2.6 (d)). The annealing twins can span the whole parent grain beginning at one boundary and ending at the opposite one, so the associated TBs are fully coherent with the matrix. However, sometimes the annealing twin does not reach the opposite boundary, leading to the formation of another TB (perpendicular to the coherent TB), which is incoherent [138, 164]. This is the case of Fig. 2.6 (d), in which the slip traces are parallel to the coherent TB (and, thus, neither slip transfer nor slip blocking occurs), and slip transfer is registered at the incoherent TB. Conversely, the slip blocking at GBs or TBs was indicated by the lack of continuity between the observed slip bands across the boundary, and this observation was reinforced by the existence of ledges or topography at the boundary, which is indicative of incompatibility of deformation between both grains (Fig. 2.6 (b)). In some cases, the impingement of the slip traces on a GB leads to the formation of micro volumes of deformation (Fig. 2.6 (e)), which appear due to a high density of dislocations, local crystalline rotations and/or grain boundary shearing, and also indicate that slip transfer is not possible [62].

The traces of the different {111} slip planes in each Ni grain on the specimen surface were obtained from a Matlab code from the crystallographic orientation of the grain provided by the EBSD scans obtained before deformation. It was assumed that the small lattice rotations induced by the applied deformation were negligible. To this end, the slip systems were rotated from the crystal to the sample reference frame using the orientation matrix computed from the Euler angles of the grain in Bunge convention. The trace orientation was computed from the cross-product between the slip plane normal and the z axis of the specimen in the sample reference frame.

The orientation of the traces for different slip systems was compared with the experimental slip traces (Fig. 2.6) to identify the active slip plane. Then, the SF for the possible slip directions in the active slip plane were determined assuming uniaxial tension from the stress tensor rotated to the crystal reference frame. Among the three possible slip systems sharing the active slip plane, it was assumed that deformation occurred in the one with the highest SF, which is a reasonable assumption given the absence of any information regarding the stress state in the microstructure [25, 197]. Once the two active slip systems across the GB or TB were identified, different metrics can be determined to assess whether they are able to predict slip transfer or blocking. Among them, the Luster-Morris parameter m' and the residual Burgers vector Δb have been used previously [2, 7, 82, 167] in metallic polycrystals. It should be noted that if slip traces were only visible in one grain across the boundary but not in the other, these GBs or TBs were not included in the analysis because it was not possible to identify the active slip plane in the latter grain.

The analysis of slip transfer/blocking included 133 regular GBs and 99 TBs (75 coherent and 24 incoherent). They showed that slip transfer mainly took place at GBs with low misorientation angle ($\Theta < 20°$) and in TBs, which present a misorientation angle of $\Theta = 60°$ (Fig. 2.7 (a)). The experimental results of slip transfer/blocking at boundaries are plotted in Fig. 2.7 (b) as a function of the Luster-Morris parameter m' and the misorientation angle. They show that slip transfer is strongly correlated with high values of m' and that slip

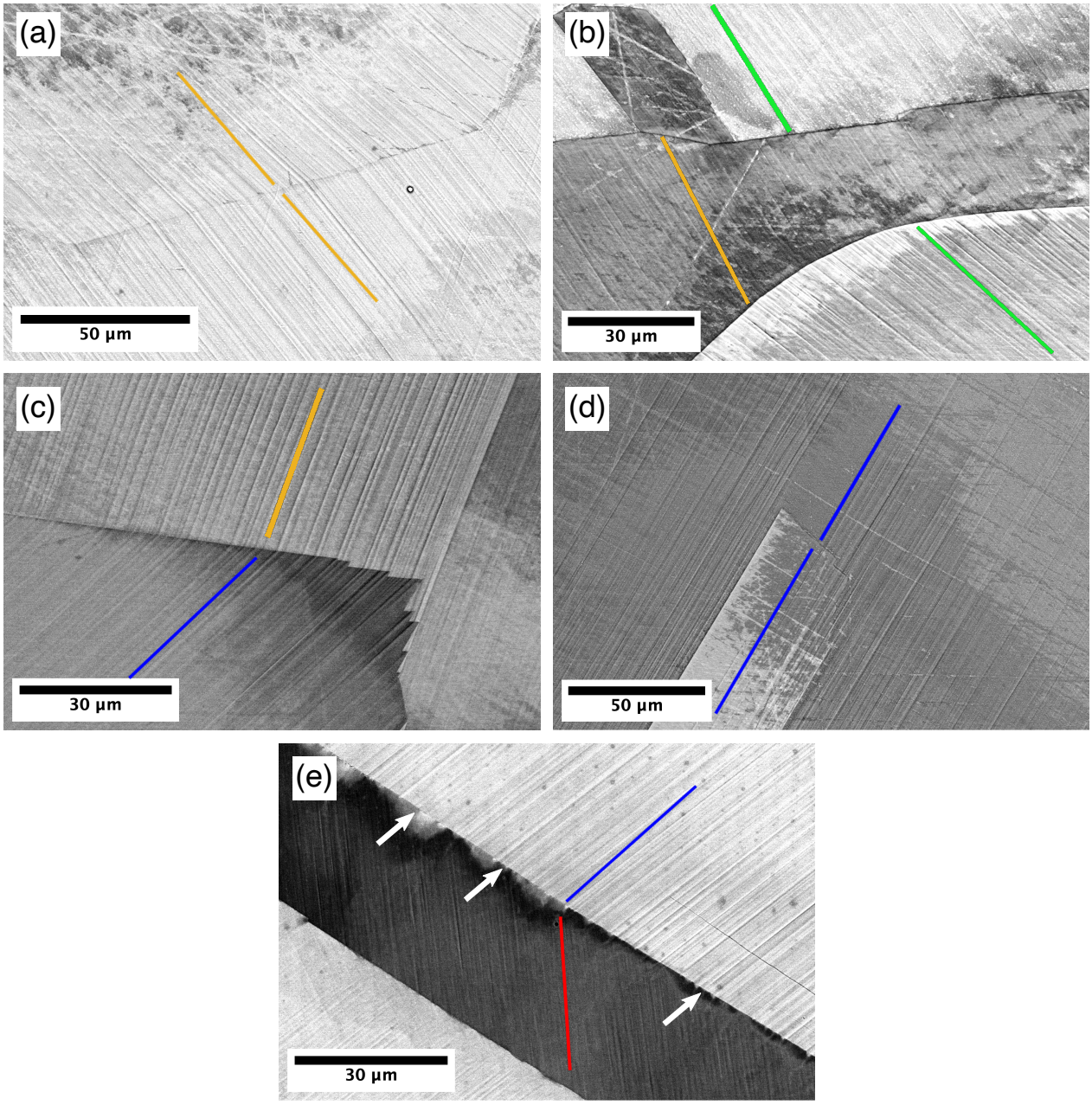

Figure 2.6: Examples of slip transfer and slip blocking at different GBs (a) Slip transfer across a regular GB. (b) Blocked slip at two regular GBs, supported by the slip trace discontinuity and the presence of a ledge. (c) Slip transfer across a coherent TB. (d) Slip transfer across the end of the twin boundary (incoherent TB). The slip bands in the parent grain and the twinned grain are parallel to each other and parallel to the twin boundary. (d) Blocked slip at a TB supported by the discontinuity between slip bands across the boundary and the formation of micro volumes (marked by white arrows). The orientation of the trace of the active slip system in each grain according to slip trace analysis is marked by solid lines, colored according to the active slip plane as indicated in Table 1.1.

transfer in GBs with a high misorientation angle (in the range $20° < \Theta < 60°$) was always associated with high m', which indicates a good alignment between the slip systems. However, it should be noted that slip blocking was observed in high-angle GBs even when m' was high. On the contrary, slip transfer was never observed when $m' < 0.65$. Thus, high m' seems to be a necessary condition for slip transfer at regular GBs but not sufficient, and this may be due to the influence of the twist angle θ that is unknown because it depends on the actual orientation of the GB across the sample thickness. However, the limited number of instances of slip blocking with high m' seems to indicate that the influence of θ is of second order compared to m'.

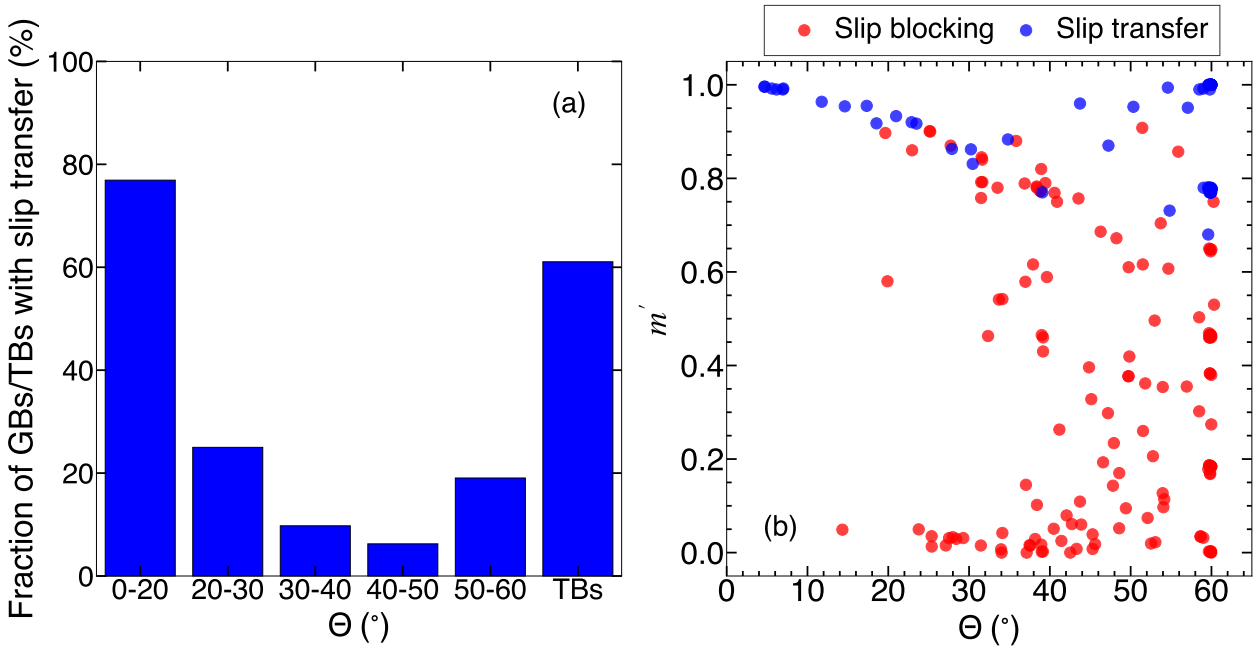

Figure 2.7: (a) Effect of the misorientation angle Θ on slip transfer for GBs and TBs. (b) Occurrence/absence of slip transfer across GBs and TBs as a function of the Luster-Morris parameter m' and the misorientation angle.

Regarding annealing TBs, slip transfer was observed in approximately 60%, and m' was either equal to 1 (32% out of the slip transfer instances across TBs) or 0.77 (remaining 68%). $m' = 1$ corresponds to slip transfer across an incoherent TB when the slip traces were parallel to the coherent TB (Fig. 2.6 (d)) while $m' = 0.77$ indicates that slip transfer took place at coherent TB between slip systems oblique to the TB (Fig. 2.6 (c)). The clustering of the slip transfer instances around these values of m' is a result of the limited number of combinations between incoming and outgoing slip systems across TBs due to the 60° rotation around <111>.

The performance of m' and Δb as metrics to predict slip transfer/blocking across GBs and TBs in Ni is depicted in Fig. 2.8. In the case of GBs, the evidence of slip transfer and slip blocking in 133 GBs is plotted in Fig. 2.8 and as a function of κ (which is related to Δb) and ψ (angle between the incoming and outgoing slip planes). Practically all the slip transfer instances are found in the lower-left corner of the figure, indicating that high values of

m' indicate a great likelihood of slip transfer. For instance, the criterion of $m' \geq 0.9$ for slip transfer (represented by a circular line in Fig. 2.8 (a)) correctly predicts 73% and 97% of the slip transfer and slip blocking events, respectively. If $m' \geq 0.75$ is chosen as the slip transfer criterion, 92% and 76% of slip transfer and slip blocking events are predicted correctly. Thus, $m' > 0.8$ seems to be an accurate criterion for slip transfer across regular GBs in Ni, similar to the results previously reported for Al [7]. The few experimental data about slip transfer/blocking that do not fulfill this criterion may be attributed to GBs with a very large twist angle θ, which impedes the slip transfer from one grain to the neighbor, but this factor seems to be of second order as compared with the role played by m'.

In the case of coherent and incoherent TBs (Fig. 2.8 (b)), slip transfer seems to be controlled by the angle between slip directions κ or, in other words, by the residual Burgers vector Δb. Slip transfer was found in 43 coherent ($\psi \approx 39°$) and 21 incoherent TBs ($\psi \approx 0°$) when $\Delta b \approx 0$, and slip blocking was found in 35 coherent and incoherent TBs when $\Delta b > 0$. When ψ and κ were close to zero, slip transfer took place across the incoherent TB present in unfinished annealing twins by the nearly perfect alignment of the active slip systems in the parent and the twinned regions (Fig. 2.6 (d)). When the angle between slip plane normals ψ was not zero, slip transfer was only observed when κ (and, thus, Δb) was close to zero. Hence, slip transfer was independent of the angle between slip system normals ψ, indicating that the incoming and outgoing slip planes may have very different orientations. Obviously, this abrupt change in the slip plane orientation, together with a negligible residual Burgers vector, is indicative of slip transfer by dislocation cross-slip at the TB [2, 52]. In addition, the role played by the twist angle θ on slip transfer can be analyzed in the case of coherent TBs because the orientation of the boundary between parent grain and twin is perfectly defined from crystallographic rotation measured by means of EBSD. This angle was calculated as the angle between the projections of the slip plane traces onto the twin boundary plane as indicated by Zhai *et al.* [193].

$$\theta = \cos^{-1}(\boldsymbol{n}_{TB} \times \boldsymbol{n}_A \cdot \boldsymbol{n}_{TB} \times \boldsymbol{n}_B) \tag{2.1}$$

where $\boldsymbol{n}_{TB}$ is the normal to the coherent TB and $\boldsymbol{n_A}$ and $\boldsymbol{n_B}$ stand for the slip plane normals to the incoming and outgoing slip systems, respectively.

As shown in Fig. 2.8 (c), only two twist angles, θ = 0° and 60° can be found in these coherent TBs. Slip blocking was found in the 24 TBs with θ = 60° while 43 of the 51 TBs with θ = 0° showed slip transfer. The latter corresponds to those TBs whose residual Burgers vector is close to 0, indicating that small values of Δb stand for the necessary condition for slip transfer in annealing TBs in Ni, and cross-slip is the physical mechanism responsible for slip transfer.

2.4 Conclusions and limitations

Slip transfer/blocking was analyzed in more than 200 GBs in two polycrystalline pure Ni samples by means of conventional slip trace analysis. The workflow for slip transfer assessment coupling EBSD orientation mapping and SEM imaging was successfully

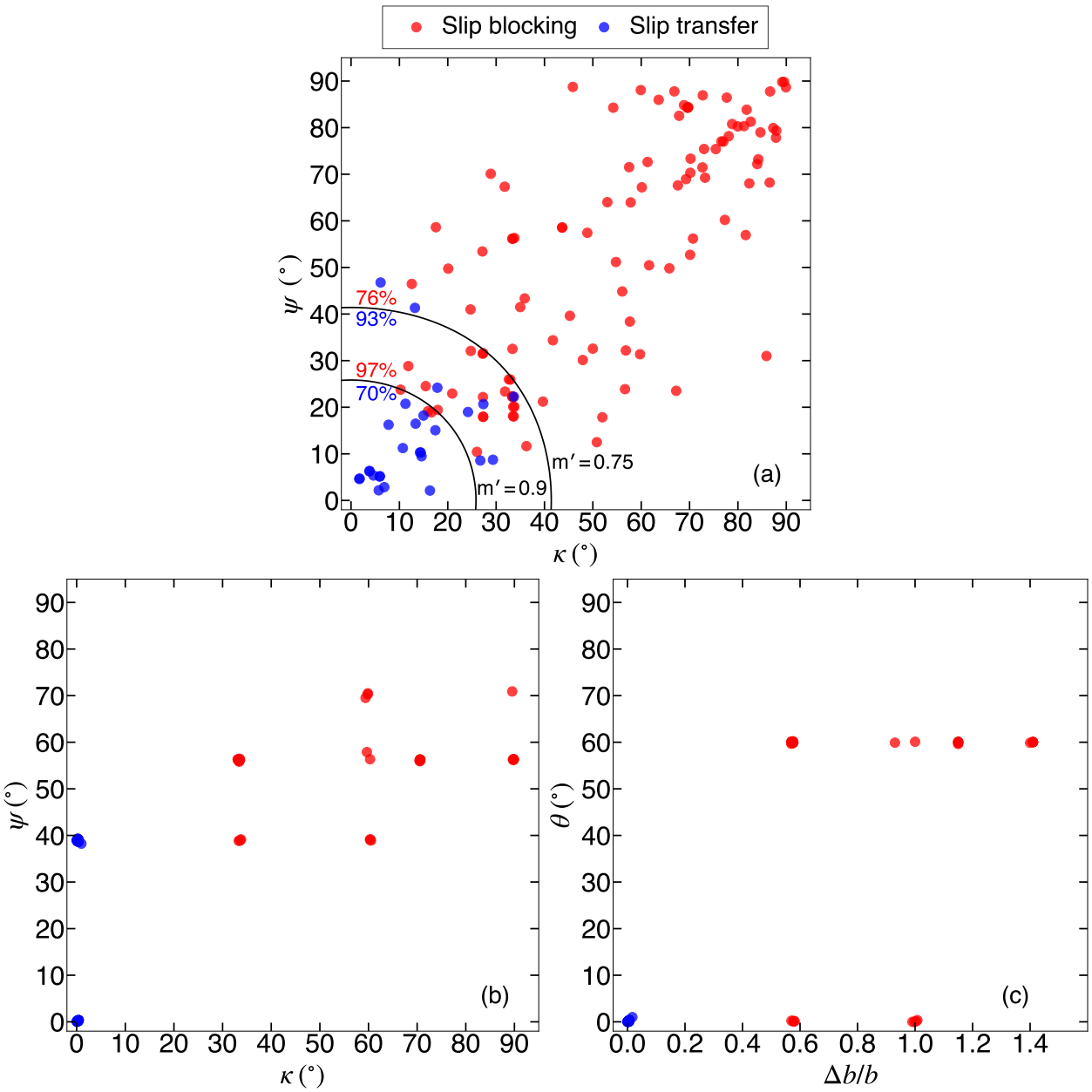

Figure 2.8: Geometrical criteria for slip transfer in Ni. (a) Regular GB. (b) Coherent and incoherent TBs. (c) Coherent TB.

established. The main conclusions of this chapter read as follows:

- Slip transfer at coherent and incoherent TBs is controlled by the residual Burgers vector and takes place when $\Delta b \approx 0$, regardless of the angle between slip normals and the twist angle between the incoming and outgoing slip planes. In this latter case, slip transfer seems to be controlled by dislocation cross-slip.
- In the case of regular GBs, slip transfer is very likely to occur across low-angle regular GBs if the Luster–Morris parameter $m' > 0.8$, and it is unlikely to take place

otherwise.

Nonetheless, although m' seems to be a good predictor for slip transfer across regular GBs in pure Ni (Fig. 2.8 (a)), there is a significant number of slip blocking instances when $0.75 < m' < 0.9$. Moreover, slip can transfer in some cases where the misorientation angle is rather high ($\Theta > 30°$) (Fig. 2.7). This behavior could be caused by different reasons that arise from the main limitations of the slip trace analysis technique, as stated in Sec. 1.3. Firstly, the active slip system is assumed to be that with the highest SF among the three possible slip systems in each slip plane. This is a reasonable assumption, especially in FCC metals whose plastic deformation is rather isotropic, but it is not guaranteed and may lead to errors.

Secondly, the lack of knowledge about the 3D GB geometry across the thickness of the sample impedes the assessment of the effect of the twist angle θ on slip transfer across regular GBs. Some experimental investigations have revealed that the θ angle may affect the occurrence of slip transfer across GBs even though the slip systems (between incoming and outgoing grains) are well aligned.

Finally, the conventional slip trace analysis does not provide information regarding the local stresses or the local strain heterogeneity in the microstructure during plastic deformation, which may also play an important role in promoting or impeding slip transfer.

3

3D grain mapping by means of Diffraction Contrast Tomography (DCT)

3.1 Introduction

The lack of knowledge about the 3D GB geometry across the thickness of a polycrystalline sample significantly biases the studies that assess the occurrence of slip transfer across GBs. As mentioned in the previous chapters, the GB inclination can affect the likelihood of slip transfer in FCC and HCP metals [108, 154]. However, most of the experimental techniques available to three-dimensionally characterize microstructures are destructive and very time-consuming, thus limiting the number of GB that can be examined.

X-ray Diffraction Contrast Tomography (DCT) has emerged as an alternative novel technique to map the crystal orientation of the grain in 3D in a non-destructive manner. DCT has been widely used to obtain grain orientations with a parallel beam (synchrotron source) [89, 117], and with a cone beam (X-ray tube source) at the lab scale [56, 93, 123, 132, 198]. More recently, Lab-based DCT (LabDCT) has proven to be an attractive option since it is more accessible than synchrotron-based DCT, and it lends itself to experiments requiring longer timescales.

The LabDCT technique was first used by King *et al.* [93] to capture the grain shape, location, and orientation in a metastable β-titanium alloy Ti21S (Tiβ21S) sample. The 3D grain maps obtained from the LabDCT technique were compared to the grain maps obtained from Phase Contrast Tomography (PCT) data, and a good agreement was reported between the two approaches. These findings led to a great amount of interest in the development of the LabDCT experimental setup. A few years later, McDonald *et al.* [123] used the LabDCT technique to map grain shape and orientations in a similar Tiβ21S sample. The authors also compared the grain orientations obtained from LabDCT scans with those obtained from EBSD data for a small polished region near the top surface of the sample. While the EBSD-DCT comparison was limited to a total of five grains, the results showed great promise for the analyses of grain maps using lab-scale X-ray equipment.

The unique combination of a lab-scale commercial X-ray computed tomography (XCT)

setup and the LabDCT technique made 3D grain maps available to a wider range of researchers. In the following years, the LabDCT technique was used to study the sintering of copper metal powder [122], recrystallization of production steel [172], grain orientation and shape in non-metallic materials [84], impurities in polycrystalline silicon [92], liquid metal embrittlement and grain growth mechanisms in steel samples [173], and corrosion in Al alloys [196, 198]. Bachman *et al.* [13] further advanced the LabDCT analyses technique and developed a fast and more accurate geometric indexing algorithm to capture the grain orientation and morphology from the diffraction data, and Niverty *et al.* [132] presented a new forward-modeling approach for the refinement of LabDCT grain reconstructions via an iterative reconstruction process thereby increasing fidelity of grain maps obtained from LabDCT. Recent developments in advanced LabDCT acquisition approaches have brought larger and more challenging geometries within the reach of LabDCT [134, 171]; however, no studies exist in the literature that systematically and quantitatively assess the use of these advanced LabDCT acquisition strategies and compare them to the conventional LabDCT approaches.

In this chapter, a detailed analysis of the grain maps is presented for a pure Ti sample by means of the tried-and-tested conventional LabDCT (C-DCT) acquisition approach and the more recent helical phyllotaxis LabDCT (HP-DCT) acquisition approach. The DCT-based grain maps were compared with those obtained on the surface from ground-truth EBSD and SEM data. Furthermore, the quality of grain reconstructions, grain orientations, GB misorientations, grain shapes, and grain morphology have been quantitatively assessed.

3.2 Materials and methods

3.2.1 Titanium sample

The sample used in this study was obtained from a 99.99% pure Ti foil with a thickness of 0.25 mm (purchased from Goodfellow). A micro-tensile specimen with a $5 \times 1\ mm^2$ central gauge section was machined by electro-discharge machining. The sample was subsequently annealed at 850° for eight hours to promote grain growth in a tubular vacuum furnace under continuum vacuum to prevent oxidation.

The central region of the gauge section was characterized using both SEM and EBSD. The EBSD map of the central gage section was obtained after metallographic preparation of the sample surface by electropolishing using Struers A3 electrolyte at room temperature and 38 V. The EBSD map was acquired using a FEI Helios NanoLab 600i dual beam microscope equipped with an Oxford Instruments EBSD detector at a voltage of 20 kV and a current of 2.7 nA. The step size was 3 μm to obtain good geometrical accuracy, and the overall indexing was above 95%. The EBSD map was post-processed using the open-source MATLAB toolbox MTEX [14], and the data was cleaned using a spline filter to fill non-indexed points. The threshold misorientation for grain reconstruction was set to 0.5°. In addition to the EBSD map, a lower resolution full field of view SEM scan of the central gauge region was also acquired using a Thermo Scientific Apreo 2 SEM at 20 kV and 1.6

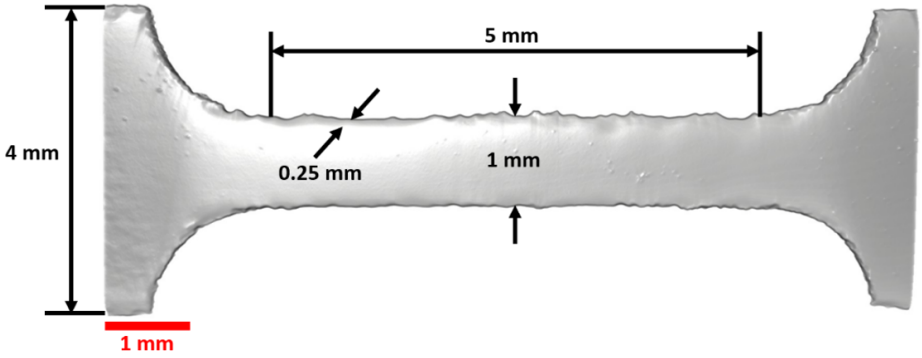

Figure 3.1: Pure Ti sample prepared using electro-discharge machining followed by annealing in vacuum at $850°$.

nA with the concentric backscatter detector (CBS) to resolve the grain boundaries on the surface of the sample.

3.2.2 Diffraction Contrast Tomography (DCT)

The DCT scans of the Ti sample were carried out in a lab-scale X-ray microscope (Zeiss Xradia Versa 620) equipped with DCT capabilities [122–124, 132, 198]. The schematic of the LabDCT setup is shown in Fig. 3.2. The sample was illuminated with a W lab source. The diffraction spots emanating from the sample were captured using a near-field detector. The Ti sample used in this study was positioned in such a manner that it was equidistant from the X-ray source and the detector (Laue Focusing Geometry) with both a source-to-sample (L_{ss}) and sample-to-detector (L_{sd}) distance of 14 mm. The spots created in a LabDCT setup with Laue Focusing Geometry tend to be shaped like elongated streaks due to astigmatic magnification caused by the polychromatic beam with a conical geometry [93]. This allows us to get a high photon count for each diffraction spot at the detector, thereby reducing the exposure time needed for each projection. Conventional DCT (C-DCT) scans are generally carried out by illuminating different orientations of the sample ($0 - 360°$) while keeping the samples fixed at a given height. In the case of a vertically extended sample (such as the one shown in Fig. 3.1), this process is repeated for different vertical sections of the sample by moving the sample vertically in discrete vertical steps, followed by a $360°$ rotation to obtain the diffraction projections at each vertical position (see Fig. 3.3). Generally, 181 diffraction projections at $2°$ interval rotation are captured for each vertical position. The combination of vertical movement followed by a $360°$ rotation is repeated until the entire region of interest is scanned. This approach, after the reconstruction of the grains, results in multiple grain maps, which are then stitched together to obtain the grain map of the entire sample.

In contrast, the sample is rotated and vertically translated to capture the entire sample in a single scan in helical phyllotaxis DCT (HP-DCT) scans. This scanning approach is ideal for the Ti sample used in this research since the central gauge section of the tensile sample is narrow enough to fit in the letterbox aperture's field of view but long enough that a

single C-DCT scan cannot capture the entire region of interest [134]. The different regions of the sample are illuminated by moving the sample in a helical phyllotaxis motion (see Fig. 3.3), which results in uniform angular coverage of the sample over the entire vertical extent. The sample is rotated by an increment of $137.5°$ and vertically translated following the recommendations by Xnovotech [188] for a minimum number of projections needed in the illuminated region of the sample for the forward modeling reconstruction analysis [13, 132]. Unlike the C-DCT scanning approach, the HP-DCT scanning approach allows the capture of grain maps of more challenging sample geometries without the need for stitching of individual grain maps. Furthermore, more uniform illumination of the sample is achieved with the incident x-rays due to the helical phyllotaxis motion, leading to a more efficient data collection than the C-DCT approach.

Table 3.1 presents a summary of the DCT scans carried out for this study. Both C-DCT and HP-DCT scans were carried out on the Ti sample at a source voltage of 160 kV and a source power of 15 W. A letter box aperture 250×750 μm in size was used to shape the incident x-rays on the sample. Each projection was captured with an exposure time of 180 s, which ensured a good signal-to-noise ratio for the diffraction spots. The C-DCT scan was carried out with 181 projections for each vertical position, and a total of 5 scans were performed to cover the central region of the sample (approximately 1 mm in length), with adjacent scans having an overlap of approximately 15%. This resulted in a total of 905 diffraction contrast projections for the conventional DCT scan. The same central region was also scanned with the HP-DCT approach with 680 projections.

Approach	Nb of segments	Source voltage (kV)	Source power (W)	Exposure time (s)	Nb of projections	Total scan time (h)[a]	Average grain completeness (%)
C-DCT	5	160	15	180	905[b]	45.25	81
HP-DCT	1				680	34	86

[a] Total scan time computed as the number of projections $\times$ exposure time per projection (180 s).

[b] Each section of the conventional scan was carried out with 181 projections, making the total number of projections for the targeted volume to be 905. An overlap of 15% was used between the adjacent scans to ensure enough space for alignment during stitching.

Table 3.1: Summary of DCT acquisition and reconstruction approach followed in the current study: scanning and reconstruction times for conventional DCT (C-DCT) and helical phyllotaxis (HP-DCT) and achieved average grain completeness values.

Once the scans were completed, the grain reconstructions from the captured diffraction data were carried out following the forward modeling approach [1, 13] using the fast geometric indexing reconstruction technique developed by Bachmann *et al.* [13] as implemented in GrainMapper3D 3.0 [188]. Fig. 3.4 shows a brief outline of the forward modeling approach. The same reconstruction approach was used for both conventional and helical phyllotaxis DCT reconstructions. For the filtration process, a rolling median filter was applied to the projections to enhance the contrast of the diffraction spots, followed by a grey level-based thresholding for segmentation of the diffraction spots. The four strongest lattice planes of the HCP Ti crystal structure with a c/a ratio of 1.587 were

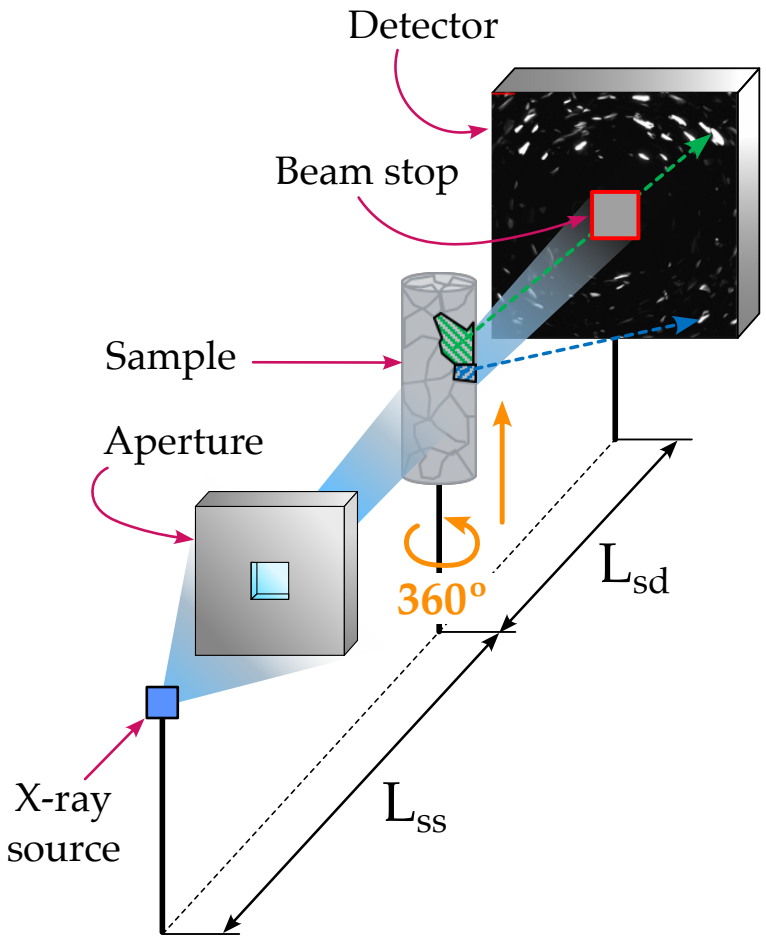

Figure 3.2: LabDCT acquisition set-up using a conical beam source.

used for the grain indexing. The initial reconstructions were iteratively refined by adjusting the source and detector distances in the forward model to minimize the horizontal and vertical distances between the observed and predicted diffraction spots (residuals). The iterations were carried out until no subsequent improvements were observed in the quality of the reconstructed grains (quantified using the completeness parameter). The number of iterations needed to refine the grain reconstructions was found to be similar for the C-DCT and HP-DCT datasets. The final grain reconstruction was carried out at a resolution of 5 $\mu m/\text{voxel}$. The total volume of the reconstructed sample was approximately 0.2 mm^3, while each section of the C-DCT scan had a volume of 0.045 mm^3.

Each conventional DCT scan took approximately 9 hours of acquisition time, while the reconstruction for each of these scans took approximately 10 hours. Therefore, each scan and reconstruction pair took approximately 19 hours to complete. The reconstructions were carried out using GrainMapper3D 3.0 on a Windows PC, with an Intel Xeon Silver 4144 processor with a clock speed of 2.19 GHz and a total RAM of 128 GB. Table 3.1 presents a summary of the scan and analysis time for the two acquisition strategies followed in this investigation. While the scan and analyses can be staggered in the case of the C-DCT approach, the iterative reconstruction process still requires significant manual input prior to

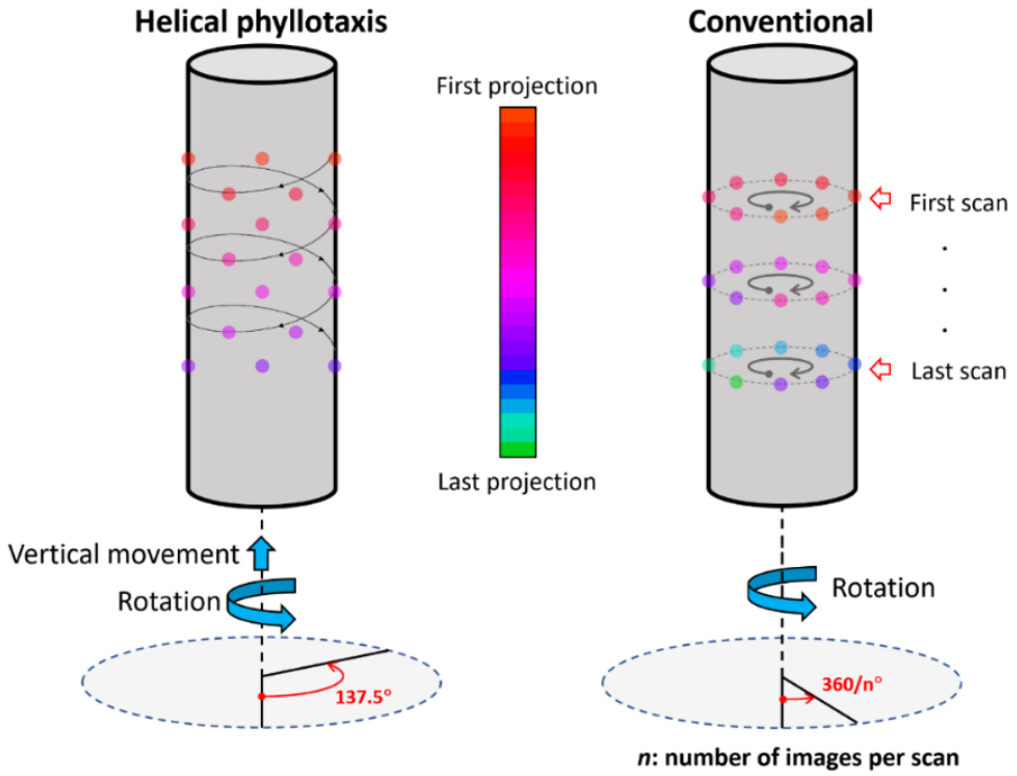

Figure 3.3: Acquisition of Lab DCT using stitched conventional DCT (C-DCT) scans and Helical Phyllotaxis DCT scans (HP-DCT) showing positions on the sample exposed to x-rays during a DCT scan.

the final reconstruction. Furthermore, due to the computationally intensive nature of the reconstruction process, only one reconstruction could be carried out at once. Additionally, the time needed for reconstruction optimization tends to be user-dependent, and it generally takes 30-40% of the entire reconstruction time, with the final reconstruction taking 60-70% of the reconstruction time. While the acquisition times were comparable for the C-DCT and HP-DCT scans in this study, the total reconstruction and analysis time for the C-DCT scan was found to be approximately 5 times that of the HP-DCT scan.

3.3 Results and discussion

The 3D grain reconstructions obtained from the HP-DCT and C-DCT scans are compared in this section, and the accuracy of the grain maps obtained from the two approaches is discussed. The grain orientations obtained from the DCT scans are compared with the ground-truth orientations on the surface of the sample obtained from EBSD data. The differences in GB misorientations between corresponding grains in the DCT and EBSD grain maps are also quantified. Finally, the grain size, morphology, and GB locations obtained from the DCT data are systematically compared with those from SEM micrographs for the corresponding grains.

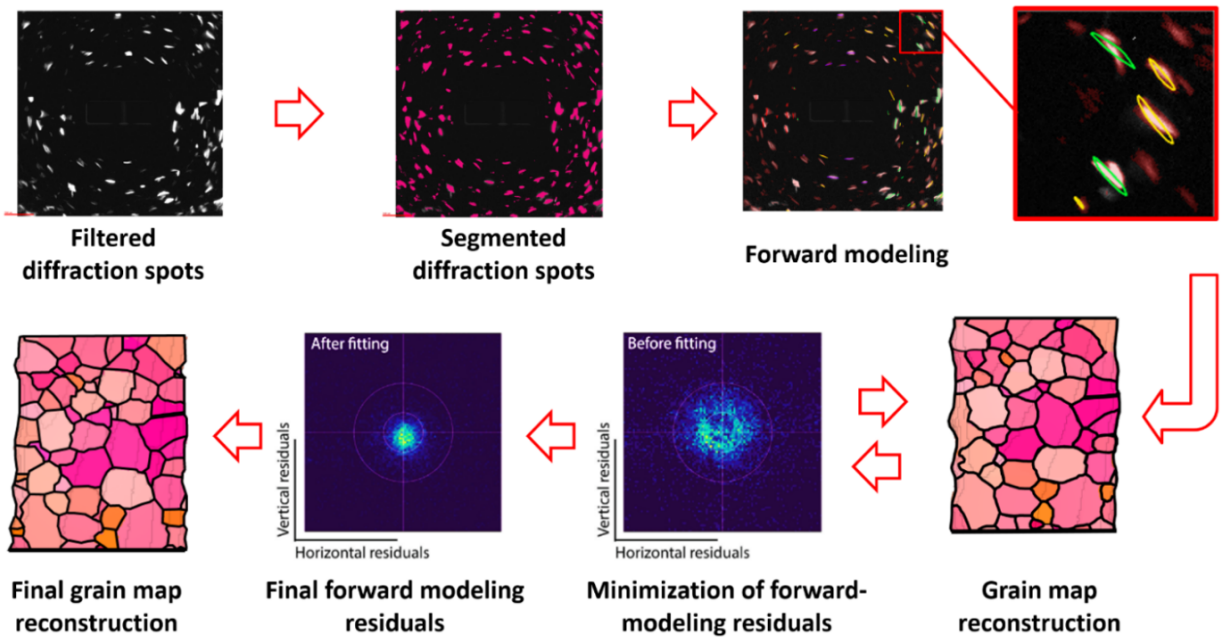

Figure 3.4: Forward modeling reconstruction approach for generation of 3D grain maps implemented in Xnovo GrainMapper3D.

3.3.1 3D grain reconstructions from LabDCT data

Fig. 3.5 shows a 3D rendering of the reconstructed grain map obtained from the C-DCT and HP-DCT scans. The grain maps indicate that the grains obtained from the conventional and helical DCT scans show similar sizes, shapes, and locations. To assess the quality of the DCT reconstructions, a completeness parameter C [13, 110] is generally used:

$$C = \frac{N_0}{N_p} \tag{3.1}$$

where N_0 is the number of observed diffraction spots for a given grain, and N_p is the number of predicted diffraction spots for a given grain from the forward modeling approach [132]. In the forward modeling approach, the mismatch between the predicted and observed diffraction spots is first separated into vertical and horizontal residuals (vertical and horizontal distance between the centers of the predicted and observed spots), and then an auto-fitting process is employed to iteratively update the instrumental parameters (relative positions of source, sample, and detector) in the analysis to minimize the vertical and horizontal residuals. Higher C values indicate higher confidence in the reconstructed grain. shows the average C values for the grains reconstructed using the HP-DCT and C-DCT data. These values indicate that the C-DCT performs slightly better than the HP-DCT scan in terms of the reliability of the reconstruction for an average grain. This observation may be explained by the larger number of total projections captured in the C-DCT scans compared to the HP-DCT scan. A larger number of projections implies that the diffraction spots for a given grain will be captured more frequently in the data, leading to a more robust grain reconstruction.

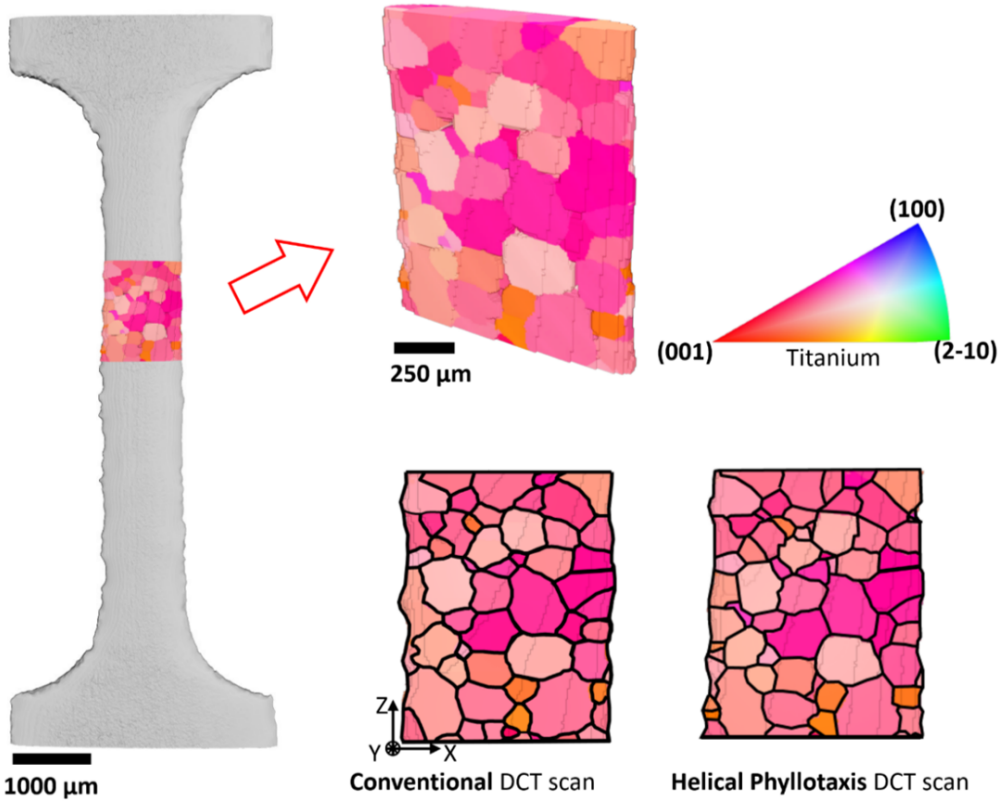

Figure 3.5: 3D grain reconstructions of the central region in the Ti sample: conventional DCT scan acquisition and helical phyllotaxis scan acquisition. The grains are colored according to the inverse pole figure color key along the y-direction.

To better quantify the robustness of the grain reconstruction, it is important to look at individual grain completeness values. While an average grain completeness value is useful to assess the overall quality of the sample, it does not give any information about local grain completeness, e.g., grain completeness as a function of 3D grain size. Fig. 3.6 (a) shows the distribution of average grain completeness, and Fig. 3.6 (b) shows the cumulative distribution of the average grain completeness for the C-DCT and HP-DCT scans. The cumulative distribution in Fig. 3.6 (b) also presents the distribution of the average grain completeness of individual sections of the conventional scans as solid lines. While the average completeness is higher for the C-DCT scans, the distribution of cumulative grain completeness is comparable to the HP-DCT scans in two sections in the C-DCT scans. This may be explained by the occurrence of smaller grains in those regions, which tend to result in lower grain completeness values.

The correlation between the grain size and the average grain completeness for the two scanning strategies is depicted in Fig. 3.6 (c). While the conventional scan plots have a slightly higher average grain completeness compared to the HP-DCT scan, the distributions are quite comparable, and the difference becomes smaller for the larger grains. It is also observable that grain completeness strongly depends on the grain size until a threshold of about 30 μm, after which an increase in grain size does not significantly affect the

grain completeness in both the C-DCT and HP-DCT scans. This observation is aligned with the findings in literature [13, 54, 55] that LabDCT tends to capture grains of the order of >20-40 μm with reasonable accuracy. For the current data, grains smaller than 30 μm have a completeness value less than 75%, whereas grains larger than 30 μm have a completeness value higher than 75%. Furthermore, the difference in completeness values between HP-DCT and C-DCT for grains larger than 30 μm is less than 10%, whereas, for the grains smaller than 30 μm, the difference in completeness values is 10-15% on average. Therefore, for the current sample, the C-DCT scan exhibits better overall grain completeness values, especially for grains smaller than 30 μm.

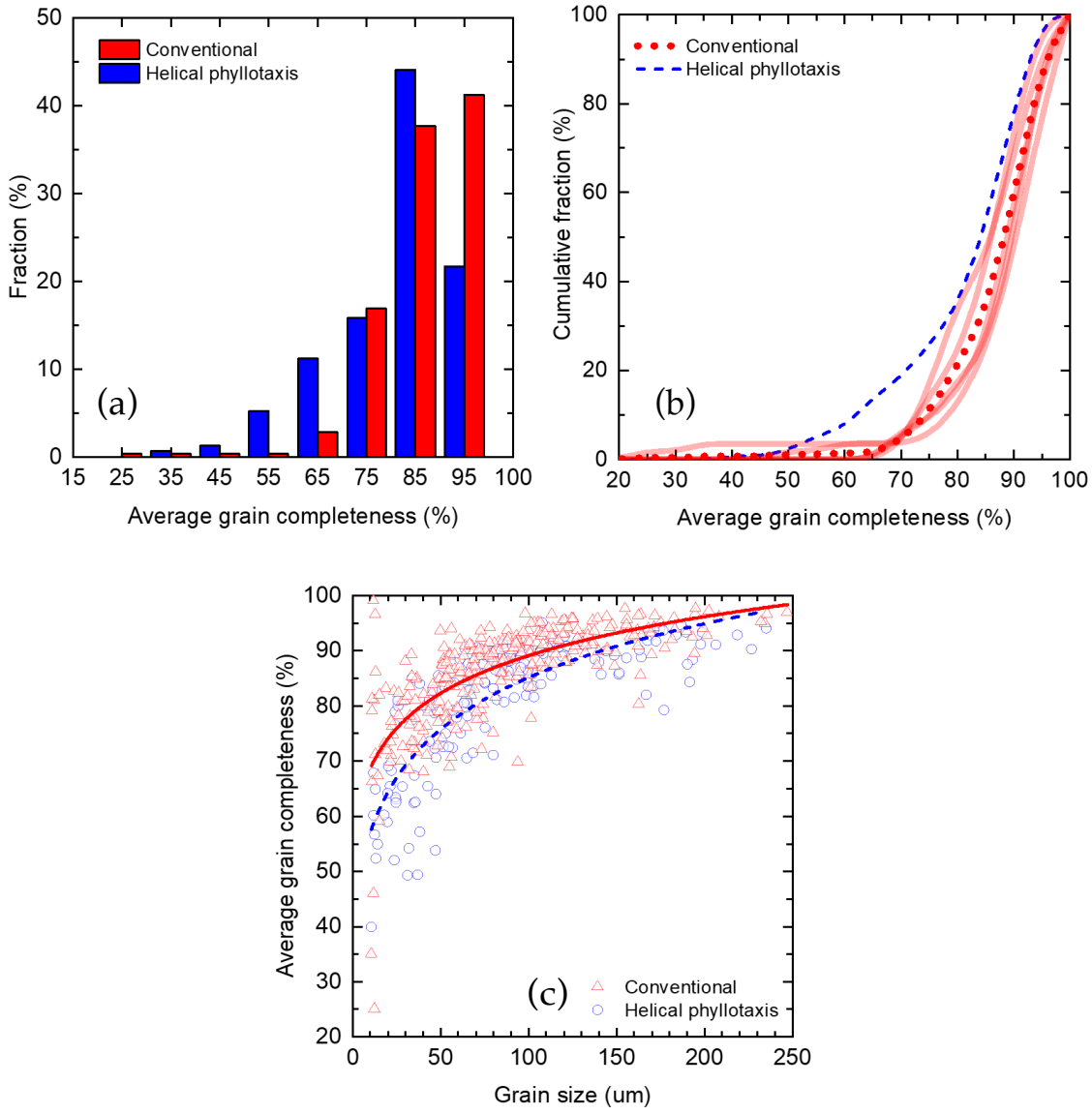

Figure 3.6: Comparison of average grain completeness obtained from conventional and helical phyllotaxis DCT scans: (a) fraction of average grain completeness, (b) cumulative distribution of average grain completeness, and (c) average grain completeness vs. grain size (equivalent sphere diameter).

3.3.2 Comparison of LabDCT and EBSD orientation maps

While a comparison of grain completeness is a good indicator of the robustness of the grain reconstruction from the forward modeling approach, the grain maps obtained from the DCT scans have to be compared to the "ground truth" provided by EBSD data to assess the accuracy of the grain orientations. DCT scans provide 3D maps of the grain, but non-destructive EBSD is limited to 2D grain maps on the surface of the sample. Therefore, to carry out a fair comparison between the EBSD (and later SEM) grain maps, the surface grains of the 3D DCT grain maps were projected on a flat surface parallel to the central plane of the sample. This approach projects the locations of the grain boundaries; however, it does not affect the grain orientation and GB misorientation values.

The grain orientation maps, (0001) pole figures, and GB misorientation maps from EBSD, C-DCT, and HP-DCT scans of the Ti sample can be found in Fig. 3.7 and 3.8, respectively. The EBSD maps show equiaxed grains and a strong bimodal texture typical of rolled commercially pure Ti [64]. The grain maps and GB misorientation maps from the DCT and EBSD show reasonably good agreement. The distribution of GB misorientation angles from EBSD and the DCT is depicted in Fig. 3.9 (a). The bimodal nature of the GB misorientation distribution is captured quite well by the DCT scans, and the two peaks in the distribution are observed at misorientation angles of 65° and 10°. The absolute difference, Δ, between the GB misorientation angles obtained by EBSD and DCT is plotted in Fig. 3.9 (b). The maximum value for Δ is below 0.6°, and 90% of the absolute differences in misorientation angle are below 0.3° for both the conventional and helical phyllotaxis DCT scans. The distribution in Fig. 3.9 (b) demonstrates quantitatively the high quality of the grain reconstructions obtained from both helical phyllotaxis and conventional DCT scans in this study.

3.3.3 Comparison of LabDCT grain geometry with SEM micrographs

In addition to the grain orientations, the accuracy of grain shapes obtained from DCT reconstructions also needs to be assessed. In the case of the grain shape, the ground truth was taken as an SEM image of the central region of the sample, depicted in Fig. 3.10 (a), which clearly shows the different grains in the Ti sample. To assess the grain shapes and locations, the SEM data was used instead of the EBSD data since the EBSD maps were cropped on the upper section due to issues with data collection. The grain maps from the conventional and helical phyllotaxis DCT scans are shown in Fig. 3.10 (b) and (c), respectively. Qualitatively, the grains from the DCT scans show good correspondence with the grains observed in the SEM image. A systematic comparison of the grain size, shape, centroidal grain distances, and average GB distance between corresponding grains in the SEM and DCT grain maps was performed to assess quantitatively the quality of the grain shape and GB locations in the DCT slice.

A comparison of the size and shape of the grains observed from SEM and DCT is presented in Figure 10. The grain size is determined from the equivalent circular diameter d:

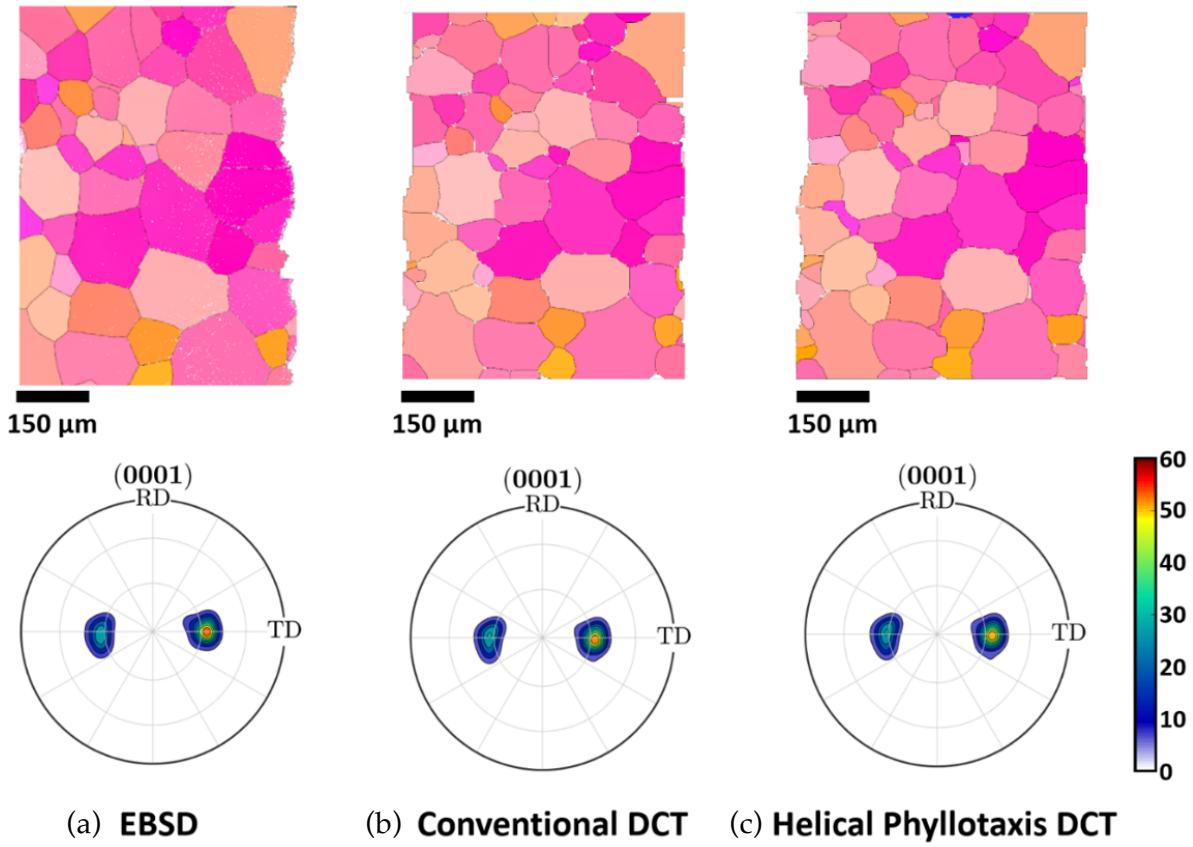

Figure 3.7: Grain maps and (0001) pole figures from (a) EBSD, (b) conventional DCT, and (c) helical phyllotaxis DCT.

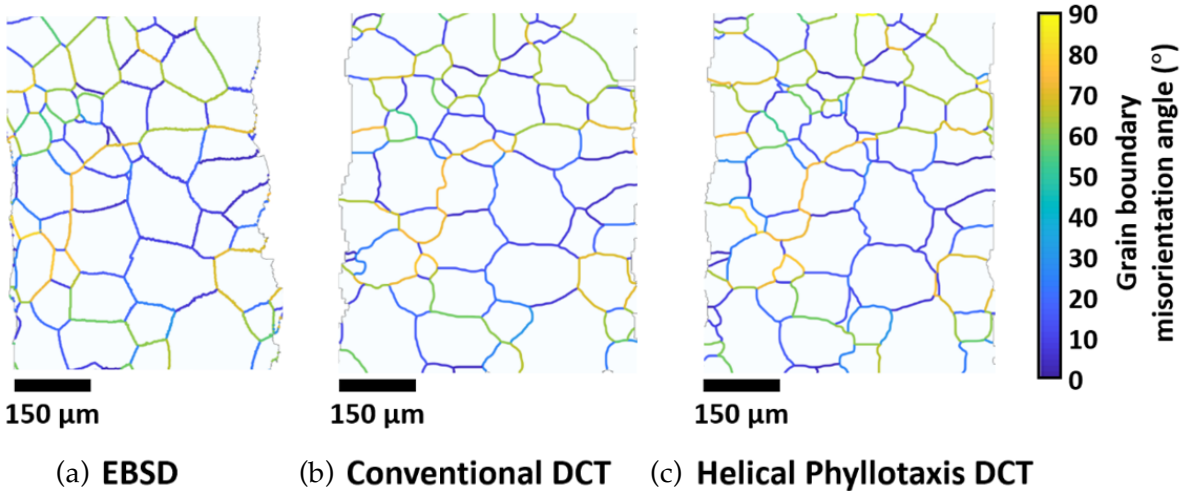

Figure 3.8: GB misorientation distribution for the grain maps from (a) EBSD, (b) conventional DCT, and (d) helical phyllotaxis DCT.

$$d = \sqrt{\frac{4A}{\pi}} \tag{3.2}$$

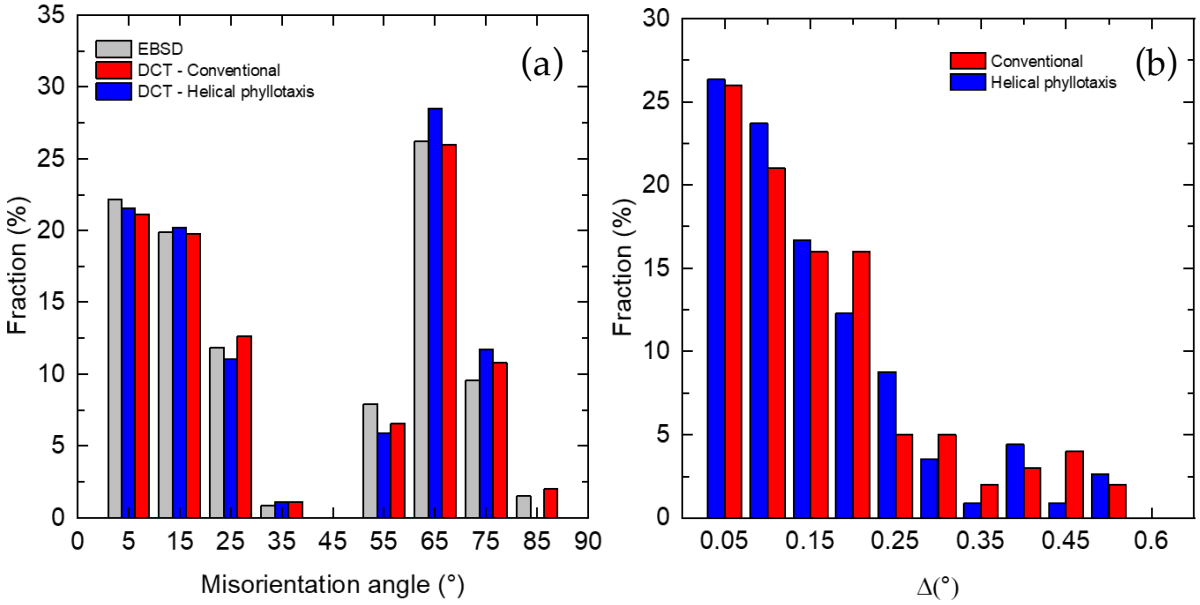

Figure 3.9: Comparison of GB misorientations: (a) distribution of GB misorientation angles obtained from EBSD and LabDCT grain reconstructions, and (b) distribution of absolute difference (Δ) in GB misorientation between EBSD and LabDCT grain maps.

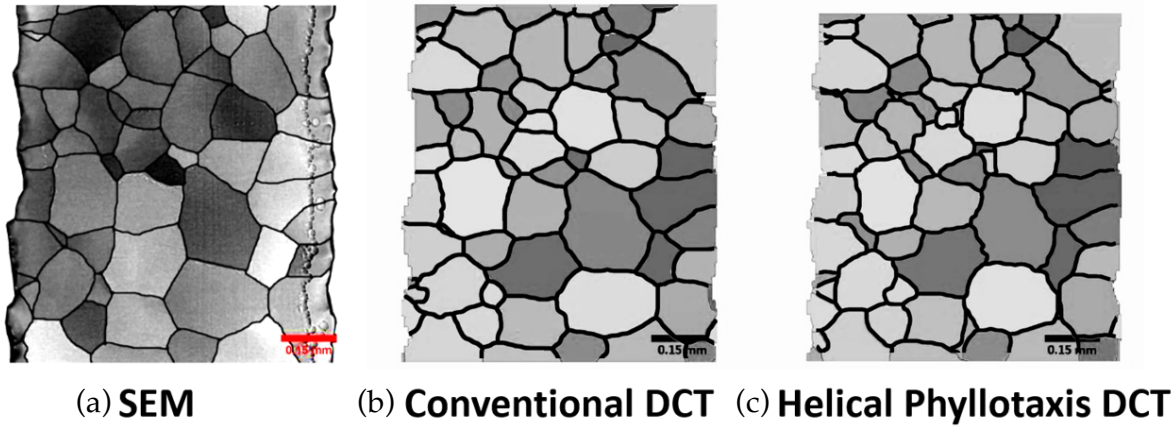

Figure 3.10: Grain maps for the central section of the Ti sample: (a) SEM micrograph, (b) Conventional DCT scan data, and (c) Helical phyllotaxis DCT scan data.

where A is the area of the grain in the 2D grain map. The grain size distributions obtained from DCT and SEM are plotted in Fig. 3.11 (a), and they show reasonable agreement. Furthermore, the grain size distribution from DCT scans normalized by the size of the corresponding grain in the SEM grain map is plotted in Fig. 3.11 (b). A value of 1 for this ratio indicates perfect agreement between the grain size of corresponding grains in the DCT and SEM maps. A value of less than 1 indicates that the DCT grain map underestimates the size of the corresponding grain in the SEM grain map. On average, the conventional DCT scans have a normalized grain size of 0.98 while the helical phyllotaxis DCT scan has a value of 1.02, indicating that the helical phyllotaxis scan slightly overesti-

mated and the conventional scan slightly underestimated the grain size as compared with the grain size measured by SEM.

Fig. 3.11 (c) shows the distribution of the 2D aspect ratio of the grains obtained from SEM and DCT. A normal distribution appears in both SEM and DCT data with an average aspect ratio of 1.4. The normalized aspect ratio, defined as the aspect ratio of the grain in the DCT scan normalized by the aspect ratio of the corresponding grain in the SEM scan, also shows a normal distribution with an average value close to 1, indicating that both the helical and conventional DCT scans capture the 2D aspect ratio of the grain with reasonable accuracy.

The results presented above indicate that both C-DCT and HP-DCT scans accurately capture the grain morphology. The next question that arises is in regard to the accuracy of the location of the grains. To compare the location of the centroids of the grains between the DCT and SEM data, the grain maps obtained from the DCT scans with the grain map obtained from the SEM image were first aligned by maximizing the overlap of the grain boundaries using an in-house Python code. The Python code overlaps the DCT and SEM GB maps and then iteratively moves the DCT GB map while keeping the SEM GB map stationary until maximum overlap between the grain boundaries is achieved, thereby aligning the two maps. The aligned and overlapped maps are shown in Fig. 3.12. The overlapped GB maps show excellent correspondence between the grain boundaries from both DCT scans with those in the SEM image. Afterward, the centroidal distance, defined as the absolute distance between the centroids of corresponding grains in the SEM and DCT grain maps, is computed for each grain in the sample using another in-house Python code. It should be noted that the centroidal distances are obtained after the global alignment of the DCT GB maps to the SEM data and not from the physical alignment of the samples.

The distribution of the centroidal distances between corresponding grains in the SEM and DCT grain maps is depicted in Fig. 3.13 (a). On average, the centroidal distance for the C-DCT scans is about 8 μm, whereas it is 12 μm for the HP-DCT scan. The largest centroidal distances were of the order of 27 μm for the HP-DCT scan and 22 μm for the C-DCT scan. The centroidal distances as a function of grain size are plotted in Fig. 3.13 (b), and no clear trends are apparent in the data. However, if the centroidal distance is normalized by the grain size (see Fig. 3.13 (c)), the error is a significant fraction of the grain size in small grains, whereas it only reaches a small fraction of the grain size in large grains. This trend is more prominent in the HP-DCT scan data than in the C-DCT scan data.

While the centroidal distance gives us a good sense of the correspondence between the grain positions from SEM and DCT data, it is also important to assess how well the DCT maps capture the GB locations. To assess the accuracy of the GB locations, the average GB distance between corresponding grains in the DCT and SEM grain maps was estimated following the method proposed by Ludwig *et al.* [116] and Bachmann *et al.* [13]. The GB maps from the SEM were first binarized - see Fig. 3.14 - and then a Euclidean distance transform (EDT) was computed for each grain in the SEM data.

The EDT of the GB map creates a heatmap of the distance to the nearest GB. In the EDT map, the regions near the GB have a small value (small distance to the nearest GB),

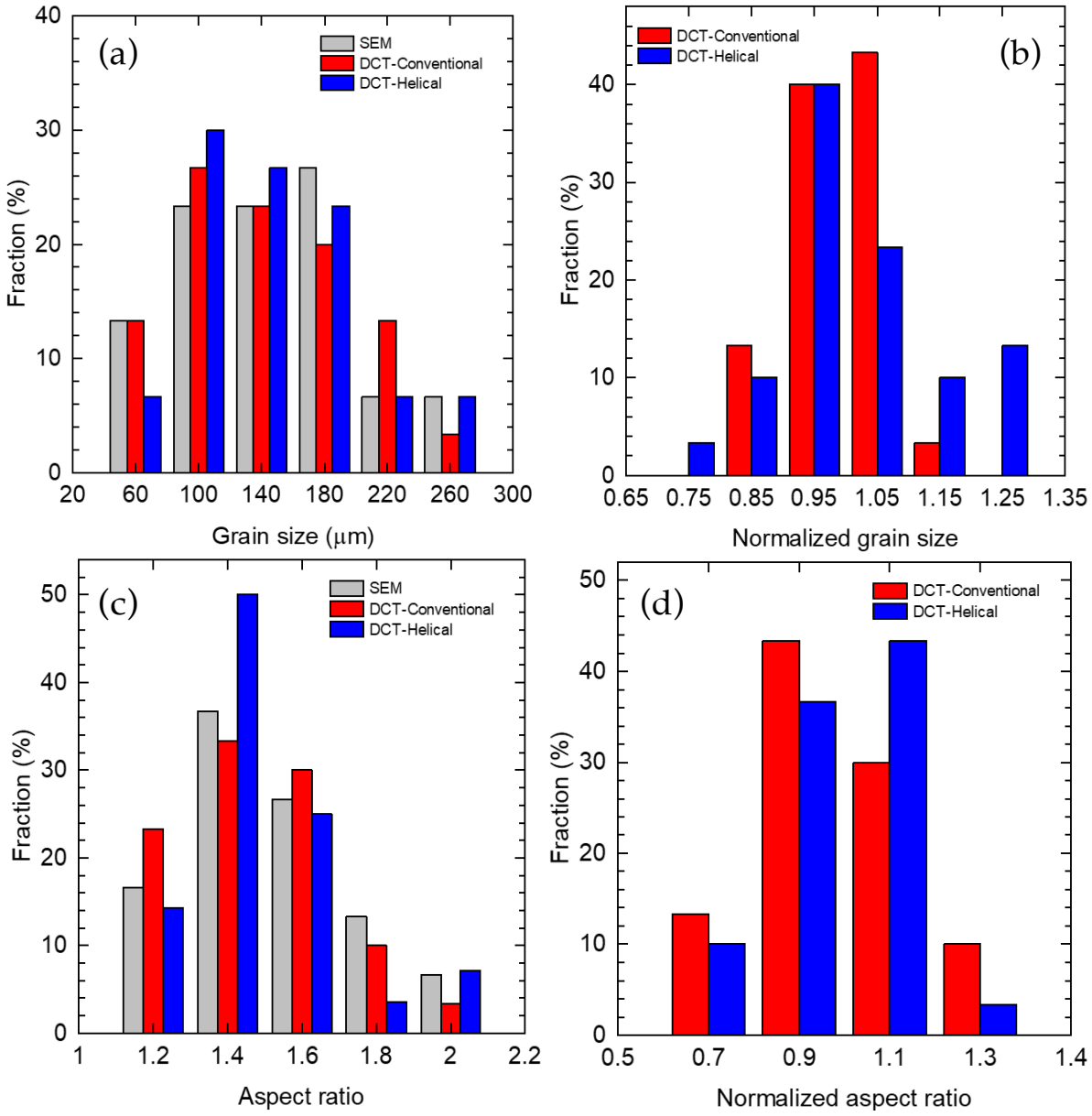

Figure 3.11: Comparison of grain size and morphology obtained from SEM and DCT scan data: (a) grain size distribution from SEM and DCT, (b) distribution of normalized grain size from DCT, (c) aspect ratio distribution from SEM and DCT, and (d) distribution of normalized aspect ratio from DCT.

whereas regions away from the GB have a large value. An EDT heat map of a central grain from the SEM data is shown in Fig. 3.15. To obtain a heatmap of the distance between the grain boundaries from DCT and SEM maps, the EDT map of the SEM grain was multiplied with the GB map (boundary pixels have a value of 1 and non-boundary pixels have a value of 0) of the corresponding grain in the aligned DCT grain map. Fig. 3.15 and 3.16 depicts an example of the GB distance heatmap for a central grain in the DCT grain maps. These heatmaps clearly show how far the DCT grain boundaries are

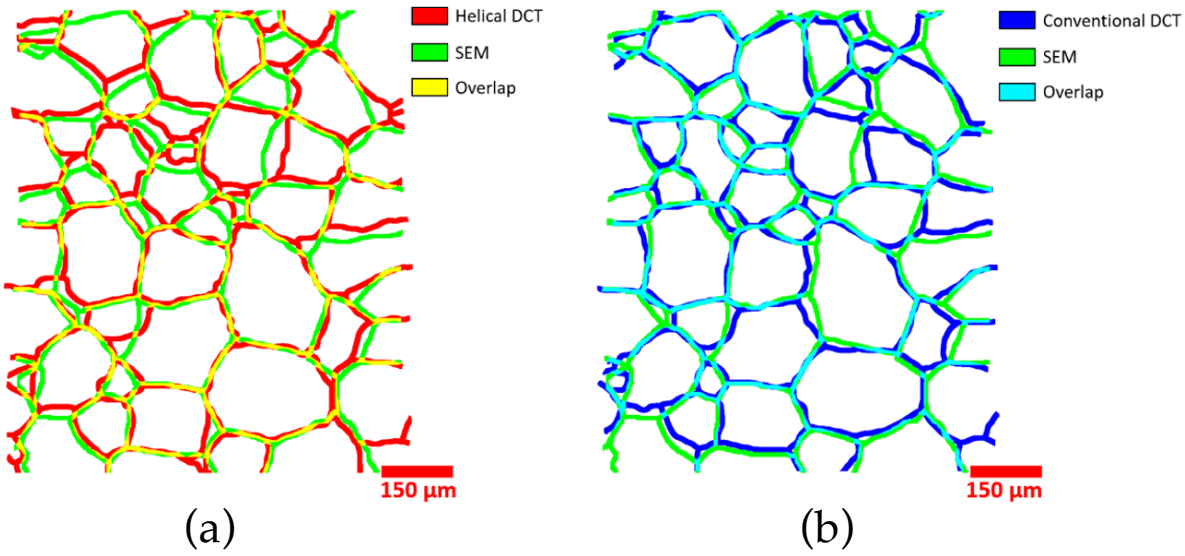

Figure 3.12: Overlap of aligned GB maps: (a) SEM vs. helical phyllotaxis DCT scan, and (b) SEM vs. conventional DCT scan.

from the SEM grain boundaries, and the average distance between the grain boundaries of corresponding grains in the SEM and DCT data can be quantified.

The process outlined above was repeated for each grain in the sample, and the distribution of the average GB distance for the grains in the DCT grain maps is presented in Fig. 3.15. The average GB distance is quite similar for the conventional and helical phyllotaxis scans, with the conventional scan having a slightly smaller value (6 μm) than the helical phyllotaxis scans (8 μm). The largest average GB distances were of the order of 15 μm for the HP-DCT scan and 12 μm for the C-DCT scan. Similar to the centroidal distance, the plot of the average GB distance shows no clear trends with the grain size. However, when the average GB distance is normalized by the grain size, the error in the GB is a larger fraction of the grain size in the case of small grains. This observation is especially true for the helical phyllotaxis scan, where the average GB distance can be as large as 20% of the grain diameter for the small grains. For applications where smaller grains play significant roles, such as in a corrosive environment [137, 148, 165], the inability to accurately capture the grains' morphology and orientation may have a non-negligible impact on our understanding of the underlying phenomena (Fig. 3.17).

3.4 Summary and conclusions

A commercially pure annealed Ti sample was characterized by LabDCT to obtain 3D crystallographic grain maps that were obtained from conventional (C-DCT) and helical phyllotaxis (HP-DCT) acquisition strategies. The quality of the 3D grain maps from both acquisition strategies was assessed, and grain shape and orientation statistics were compared against the grain maps obtained from EBSD and SEM scans of the same Ti sample. Since EBSD and SEM scans are restricted to near-surface grain information, only the sur-

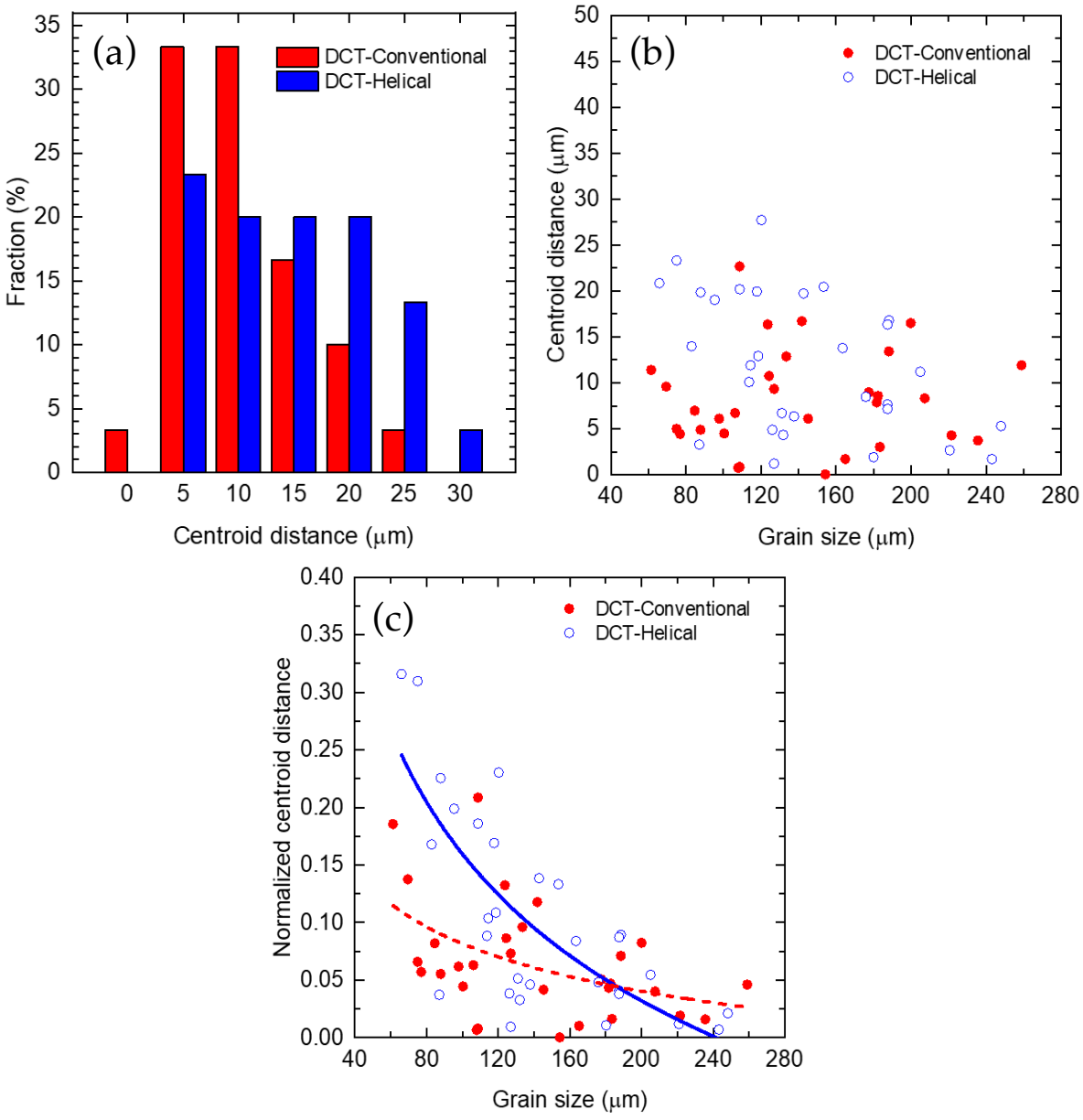

Figure 3.13: Comparison of the centroidal distance between corresponding grains in SEM and DCT grain maps: (a) distribution of centroidal distance between corresponding grain in the SEM and DCT grain maps (b) centroidal distance vs. 2D grain size, and (c) normalized centroidal distance (centroidal distance normalized by 2D grain size) vs. grain size.

face grains in the 3D grain maps from the DCT scans were extracted and compared to the EBSD and SEM data. The main findings from this investigation are the following:

1. Total scan times for HP-DCT and C-DCT scans were comparable for the samples scanned in the present study. However, the total reconstruction and analysis time for the C-DCT scans was five times longer than that of the HP-DCT scan.

2. The reliability of the grain reconstructions from the DCT scans was quantified using

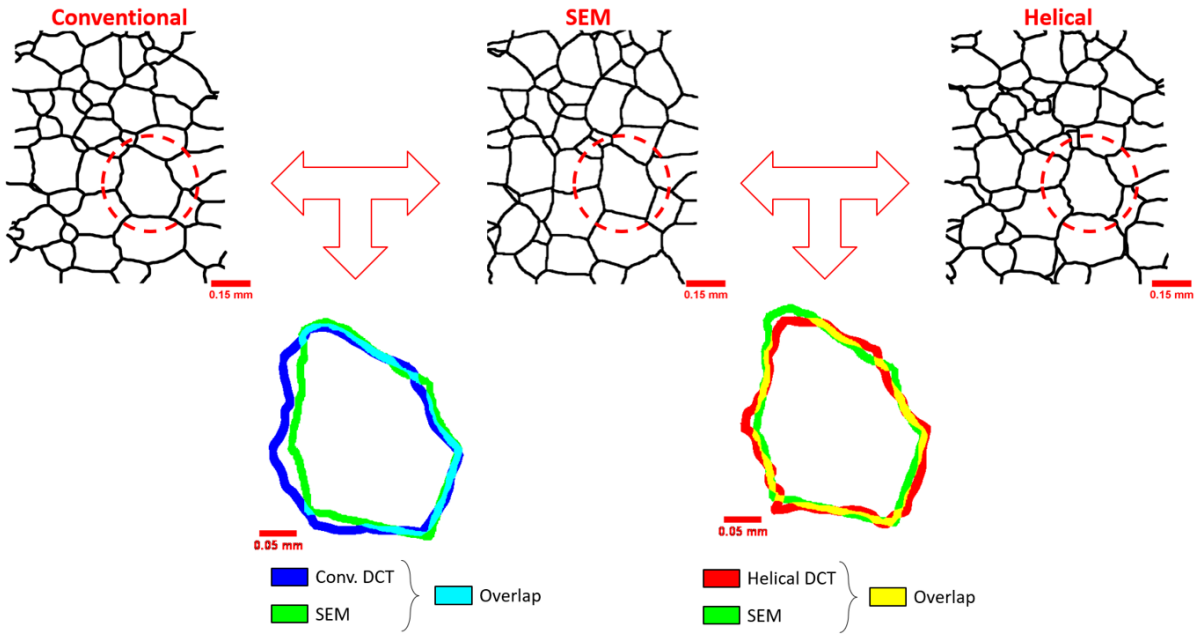

Figure 3.14: Comparison of GB detection accuracy: overlap between SEM and DCT grain data.

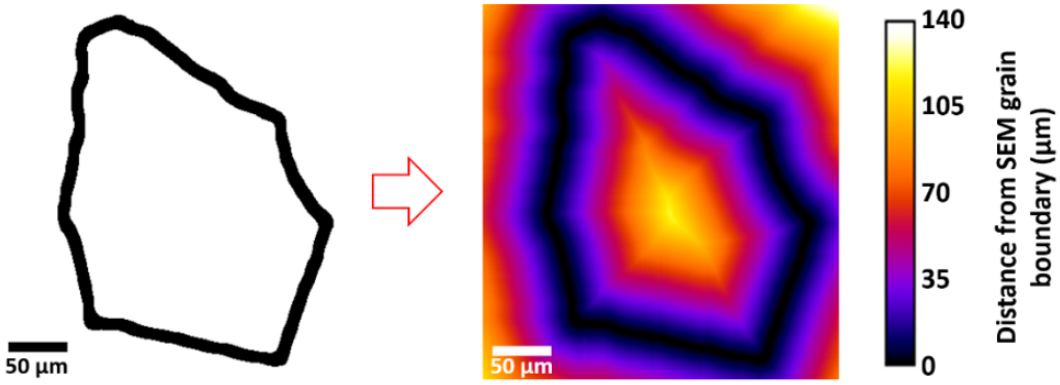

Figure 3.15: Comparison of GB detection accuracy: euclidian distance transform (EDT) heatmap of SEM grain.

a completeness parameter. It was found that the average grain completeness for both acquisition strategies was comparable with the average grain completeness, with the one from the C-DCT being marginally (5%) higher than that of the HP-DCT.

3. The grain orientation and GB misorientation maps obtained from DCT scans showed excellent agreement with the grain orientations from the EBSD data. The absolute difference between grain boundary misorientations was below $0.6°$, and 90% of the differences were below $0.3°$ for both conventional and helical scans.

4. The grain shape and morphology of the grains from the DCT grain maps were com-

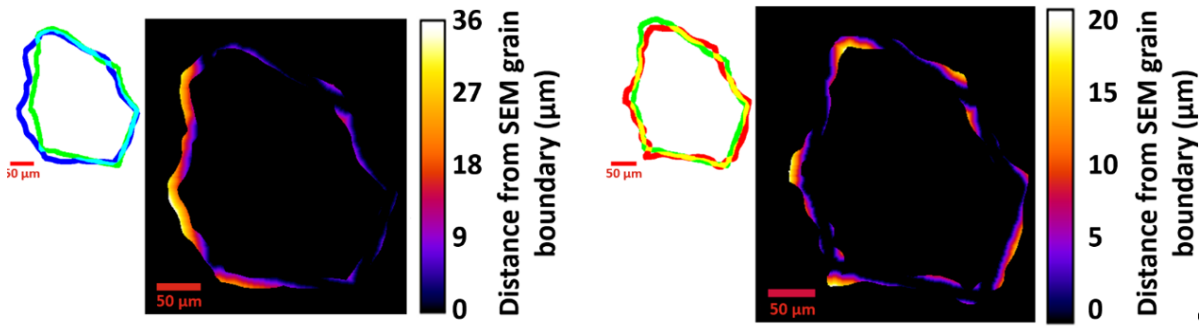

Figure 3.16: Comparison of GB detection accuracy through the heatmap of the distance between SEM and conventional DCT GB for the corresponding grain (left), and heatmap of the distance between SEM and helical phyllotaxis DCT GBs for the corresponding grain (right).

pared with those obtained from SEM grain maps. It was found that, on average, the HP-DCT scan slightly overestimated the 2D grain size by 2% while the C-DCT scan slightly underestimated the grain size from the SEM data (also by 2%). The grain aspect ratios were captured quite accurately by both acquisition strategies.

5. The position of the grain centroids obtained by DCT and SEM was compared. The differences in the positions were very small in the case of C-DCT (average difference of 8 μm) and slightly higher (12 μm) in the case of HP-DCT.

6. The average grain boundary distance for corresponding grains in the DCT and SEM scans was found to be 6 µm for the conventional DCT scans and 8 µm for the helical DCT scans, with the error being a larger fraction of the grain size for the smaller grains.

It should be noted that the analysis presented here is limited to samples with average 3D grain size in the range of 90-100 µm, and further exploration is needed to assess how these advanced DCT acquisition strategies will perform in samples with a finer grain structure. From the current data, it is clear that C-DCT scans result in higher fidelity grain maps compared to HP-DCT. However, the analysis time of the C-DCT approach for elongated sample geometries comes at a significantly higher time cost. This study demonstrates that, regardless of the scanning approach, DCT is a very useful technique for non-destructive 3D grain mapping, providing extremely valuable information that can be incorporated into the study of plastic deformation of polycrystals.

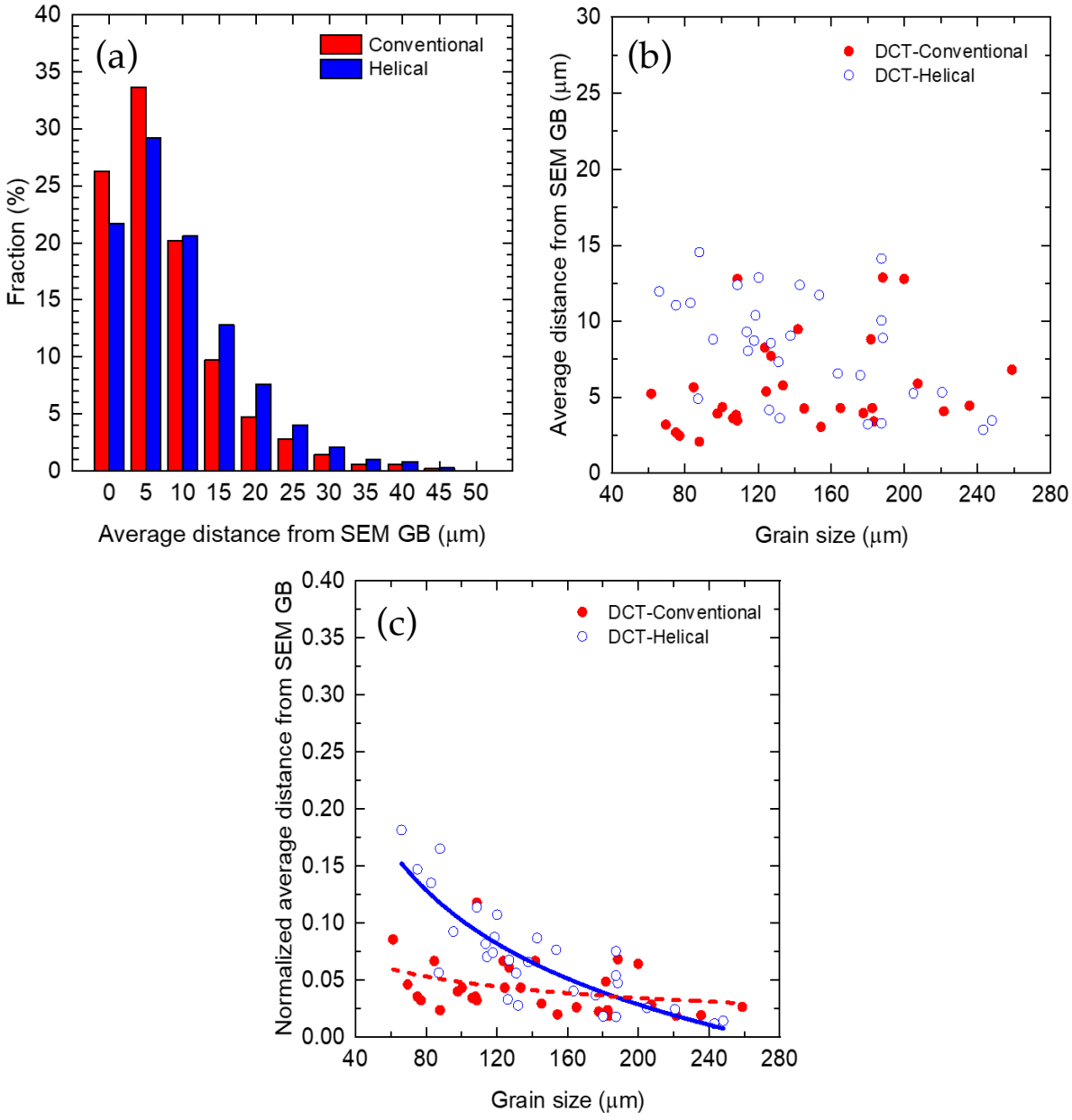

Figure 3.17: Comparison of average grain boundary distance between corresponding grains from SEM and DCT maps: (a) distribution of average grain boundary distance between SEM and DCT data, (b) average grain boundary distance vs. 2D grain size, and (c) normalized average grain boundary distance (average grain boundary distance normalized by 2D grain size) vs. grain size.

4 Analysis of slip transfer in pure Ti through 3D GB characterization

4.1 Introduction

The standard strategies to study slip transfer across GBs present two main drawbacks, namely the lack of information about the 3D GB geometry and the actual knowledge of the active slip system when several slip systems share the same slip plane. It is often argued that the limitations of the geometrical slip transfer criteria based on Δb or m' to predict slip transfer/blocking at GBs have to be associated with these uncertainties while the role played by the twist angle θ (and, thus, the accuracy of the LRB criterion) remains unknown. For instance, slip blockage was observed in five GBs in pure Mg where m' was close to 1, but $\theta > 60°$ [154]. The GB orientation within the sample was measured by sequential milling with FIB in five GBs, but it was not possible to analyze a large dataset of GBs to obtain definitive conclusions because this technique is very time-consuming.

As presented in Chapter 3, LabDCT has become a powerful tool to perform non-destructive, high-fidelity characterization of the 3D grain structure in polycrystals [123]. Notably, the accuracy of LabDCT has been extensively validated against EBSD data [60, 132, 195], and hence, it can help assess the role that the 3D geometrical features of the grains and GBs play in slip transfer. This technique is used in this chapter to assess the GB geometry of Ti foils that were later subjected to tensile deformation. Conventional slip trace analysis was used to ascertain the active prismatic slip systems and the occurrence or absence of slip transfer at several hundreds of GB. This unique data set was then used to validate/disprove the different slip transfer criteria proposed in the literature using the information on the GB orientation in 3D.

4.2 Materials and experimental techniques

High purity (99.99%) cold-rolled Ti foils of 0.25 mm in thickness were purchased from Goodfellow. A micro tensile dog-bone sample with a uniform central region of $5 \times 1\ mm^2$

was machined from the foil by electro-discharge machining. The sample was heat-treated at 850°C for 8 hours in a tubular vacuum furnace under argon atmosphere to minimize oxidation. The sample was gently ground with 1200 grit paper to remove the fine oxidation layer on the surface after the heat treatment. Afterward, it was electropolished to mirror finish on both surfaces of the central gauge section using a Struers A3 electrolyte at 27 V and room temperature.

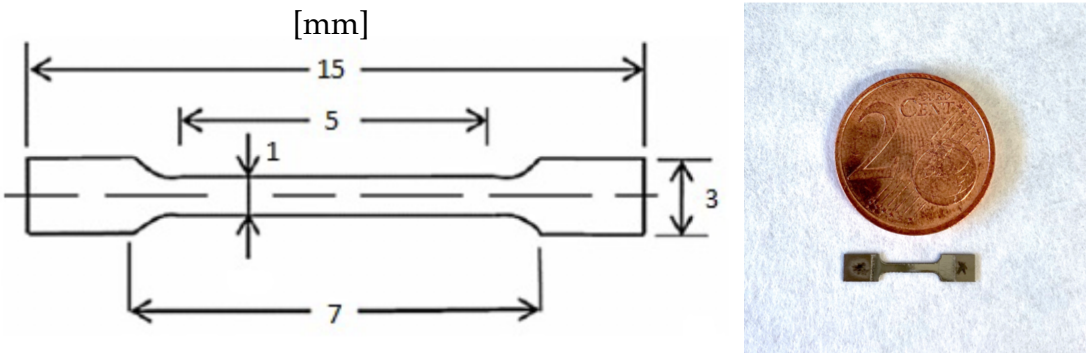

Figure 4.1: Ti dogbone micro tensile specimen dimensions in mm (left) and sample dimensions compared to a coin (right).

EBSD maps were acquired from both surfaces of the gauge length of the sample. The crystallographic orientations were obtained in a FEI Helios NanoLab 600i dual-beam microscope with an Oxford Instruments EBSD detector. The whole gauge length was mapped with several overlapping maps, followed by stitching in AZtec. The EBSD maps were acquired at 20 kV and 2.7 nA, with a step size of 3 μm, in order to accurately resolve the microstructural features. The overall quality of the EBSD maps was above 95% indexing. The maps were post-processed with the MTEX Matlab Toolbox [14] with a grain boundary misorientation threshold of 2° to capture low-angle grain boundaries.

The 3D grain structure was mapped using a Zeiss Xradia Versa 620 X-ray microscope with DCT capabilities. The sample was positioned at equal distance from the X-ray source and the detector (14 mm) (Fig. 3.2), keeping the Laue focusing geometry and a source voltage and power of 160 kV and 15 W, respectively, were used. A 4X DCT detector with a transmission beam stop was used to capture the diffraction spots during the scan. A conventional DCT (C-DCT) scanning approach, such as that presented in Chapter 3, was employed for this sample. In order to map the full gauge length with the selected aperture, seven overlapping scans were needed, followed by stitching, resulting in a total scan time of 63 h. The acquired DCT projections were iteratively reconstructed with GrainMapper3D (Xnovo Technology) using the forward modeling approach [132] until the average completeness values (Eq. 3.1) reached at least 90%. Then, Dream3D [69] was used to segment the volume into grains and grain boundaries, and Paraview [12] was used for visualization purposes.

The sample was deformed in uniaxial tension in a Kammrath and Weiss micro tensile testing machine equipped with a 1 kN load cell at a quasi-static strain rate of $\approx 10^{-3}\, s^{-1}$ to a strain of about 2%. The combination of SEM imaging and grain orientation before

deformation by EBSD was used to identify the active slip systems in the grains after deformation. The active slip system identification by conventional slip trace analysis is based on the comparison between the orientation of the experimentally observed slip bands with that obtained from the crystal orientation, as measured by EBSD [7, 24, 130]. It is worth mentioning that the crystal orientations provided by DCT could have also been used instead of EBSD to determine the theoretical orientation of the slip traces. However, the spatial resolution of EBSD at the sample surface is better than that of DCT, improving the accuracy in the case of very small grains.

4.3 Results

4.3.1 3D grain and grain boundary characterization

The DCT data reconstructed in GrainMapper3D was imported into Dream3D [69] to characterize the microstructure in 3D. Each voxel contained information about the Euler angles and the completeness value attained after the forward-modeling process. The data were denoised using a minimum completeness value of 0.1 and misorientation threshold of 2° for grain segmentation. Any spurious data were filled using an erode/dilate process with two iterations. Fig. 4.2 (a) shows the reconstructed sample gauge after post-processing in Dream3D, where the left half shows the voxelized volume. The sample was composed of approximately 24 million voxels and 588 grains, and the information about grains' positions, sizes, shapes, and misorientations was exported for the 3D microstructural analysis. A detailed view of two neighbor grains reconstructed with 5 μm voxel size is provided in Fig. 4.2 (c).

Once the volume of the sample was reconstructed, a triangular surface mesh was generated over the inner (GBs) and outer surfaces of the sample. The initial triangular surface mesh was smoothed using a Laplacian algorithm to minimize any stair-stepped appearance, and the resulting triangle data (triangle identifier, centroid, area, curvature, misorientation, and normal direction) were exported for further analysis. The right half of Fig. 4.2 (a) shows the generated surface mesh, composed of roughly 1.5 million triangles and 2319 GBs, where the outer surfaces of the sample have been removed for the sake of GB visualization. Fig. 4.2 (d) shows the surface mesh at the GBs of the grains in Fig. 4.2 (c), where the shared GB normals have been plotted as yellow arrows.

The lognormal grain size distribution obtained from DCT data is plotted in Fig. 4.3 (a). The average grain size is 111 ± 58 μm. The GB misorientation angle (also provided by DCT data after grain segmentation) is plotted in Fig. 4.3 (b) and presents a bimodal distribution with peaks at $\approx 15°$ and $\approx 70°$.

The normal vector to each triangle in the surface mesh was directly obtained from the surface mesh, and the GB normal direction, $\boldsymbol{n}_{GB}$, was estimated. To this end, a different subset was generated for every GB from the triangular mesh, so only the corresponding triangle normals were selected. The triangle winding was carefully checked and corrected so that all normal directions were pointing in the same direction. Given that the mean curvature of the studied GBs is close to 0, the GB normal was taken as the mean of the triangle

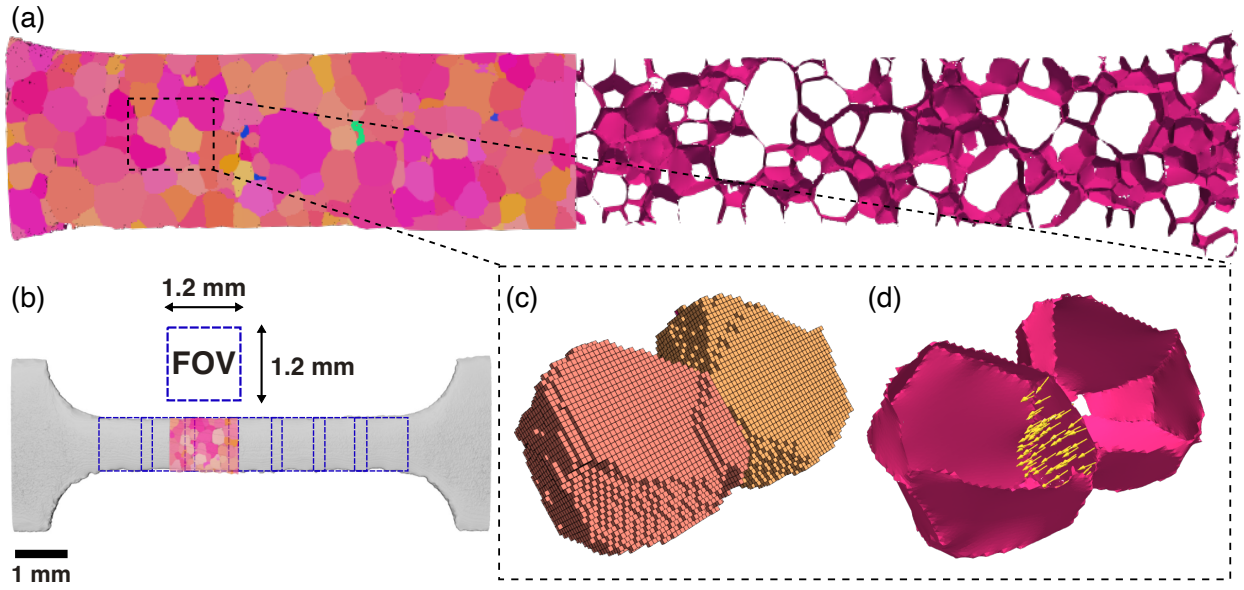

Figure 4.2: Microstructural characterization by DCT. (a) Reconstructed DCT map of the sample gauge colored according to the inverse pole figure with respect to the screen plane (color key in Fig. 4.4 (b)). The left half corresponds to the reconstructed volume of the sample, and the right half corresponds to the surface mesh generated at the GBs. (b) Sample scanning strategy consisting of 7 overlapping sub-regions to map the full gauge length. (c) Detailed view of two neighboring grains (dashed squared area in (a)), where the reconstructed voxelized volume is shown in (c), and the corresponding surface mesh is shown in (d). In the latter, some GB surface normals are drawn in yellow.

normals included in the surface. From this information, it was possible to calculate the GB inclination β, defined as the angle between the GB plane, characterized by the GB normal $\boldsymbol{n}_{GB}$, and the plane perpendicular to the sample surface and oriented along the length of the sample. Thus, vertical GBs (perpendicular to the sample surface) are characterized by high β (close to 90°). The GB inclination distribution β is plotted in Fig. 4.3 (c). As observed in Fig. 4.2 (a), there is a significant fraction ($\approx$ 20%) of vertical or close to vertical GBs with $\beta > 80°$ that grew very likely during the heat treatment due to the small thickness of the sample. Nevertheless, approximately 55% of the GB have an inclination $< 65°$.

The calculated GB normals, together with the observed active slip systems at both neighboring grains, also allowed the calculation of the twist angle θ associated with two slip planes across a GB according to (Fig. 1.5)

$$\theta = tan^{-1}\left(\frac{||\boldsymbol{l}_A \times \boldsymbol{l}_B||}{\boldsymbol{l}_A \cdot \boldsymbol{l}_B}\right) \tag{4.1}$$

where $\boldsymbol{l}_A$ and $\boldsymbol{l}_B$ stand for the traces of the incoming and the outgoing slip planes with the

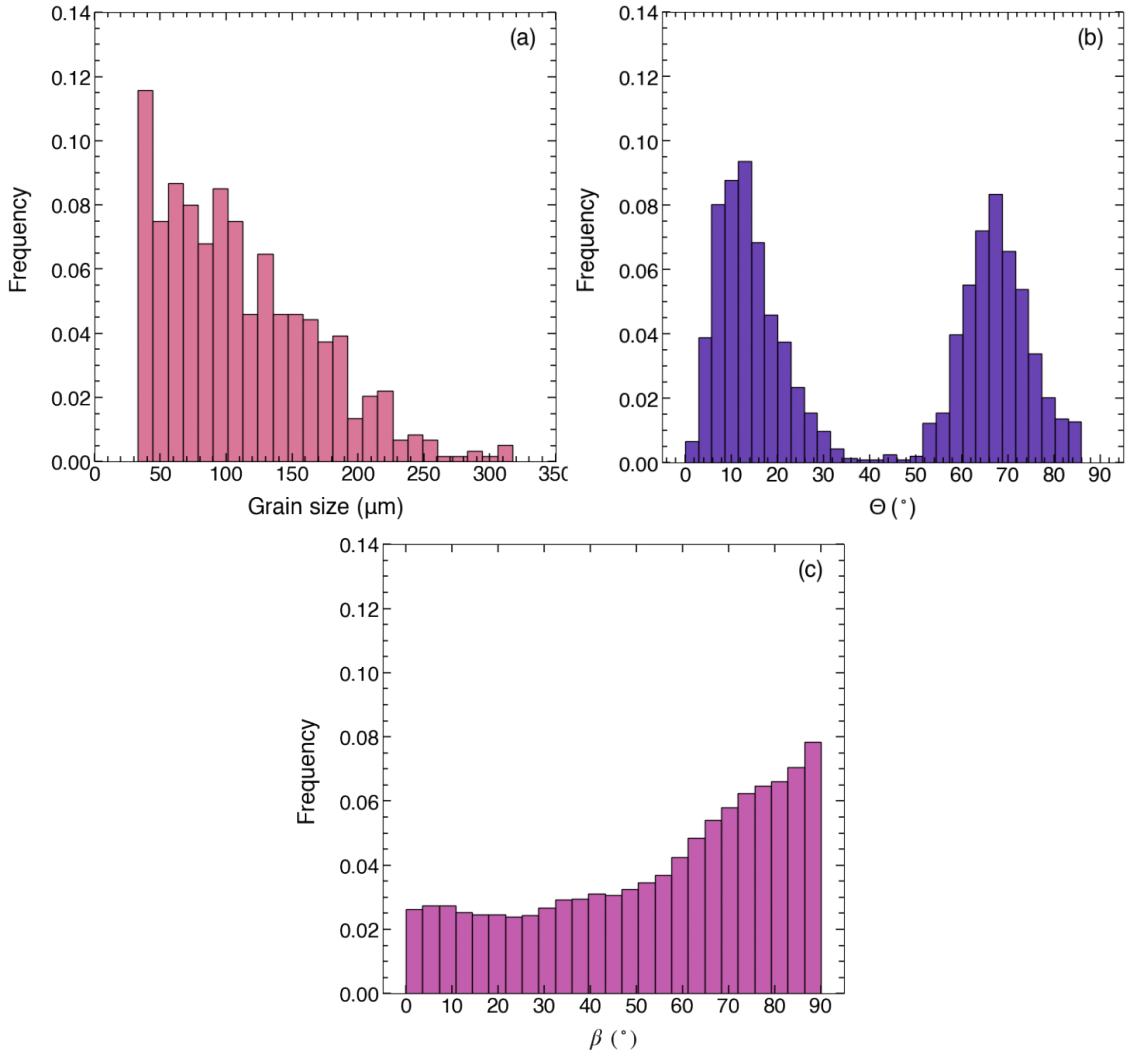

Figure 4.3: Microstructural features of the Ti sample obtained by DCT. (a) Grain size distribution, (b) Grain boundary misorientation distribution, (c) Grain boundary inclination (β) distribution.

GB plane, respectively, (Fig. 1.5) that can be calculated as follows:

$$\begin{aligned} \boldsymbol{l}_A &= \boldsymbol{n}_{GB} \times \boldsymbol{n}_A \\ \boldsymbol{l}_B &= \boldsymbol{n}_{GB} \times \boldsymbol{n}_B \end{aligned} \tag{4.2}$$

4.3.2 2D microstructural characterization

The microstructure within the surface of the sample obtained by EBSD is shown in Fig. 4.4. The grains have been colored according to the inverse pole figure perpendicular to the surface, and the color key is provided by the inverse pole figure color code in Fig. 4.4 (b). The raw EBSD map displayed in Fig. 4.4 (a) shows a good indexing rate with equiaxed grains throughout the sample gauge. The post-processed EBSD map of the rectangular region on

the left side of the sample is shown at higher magnification in Fig. 4.4(c). The GBs are colored according to their misorientation angle, ranging from very low misorientation GBs (blue) to high misorientation GBs (yellow). The relative orientation of the hexagonal unit cells is shown in the center of each grain and reveals a marked texture. The basal plane pole figure in Fig. 4.4 (d) shows a strong inclined basal texture, with the c-axes tilted about $\pm 30°$ from the Z axis (perpendicular to the surface). This texture is typical of cold-rolled commercially pure Ti [64] and agrees with the bimodal misorientation angle distribution obtained from the DCT data (Fig. 4.3 (b)). As a result of this texture, tensile deformation will favor the activation of two of the three prismatic <a> slip systems in the hexagonal unit cell, whose SF are close to 0.5 (Fig. 4.4 (c)).

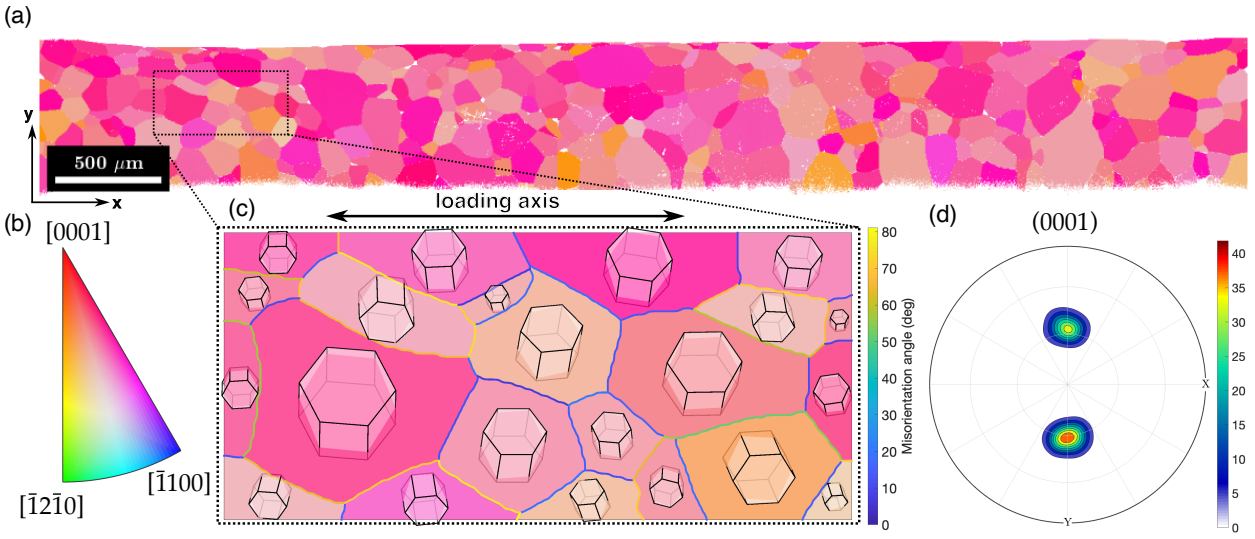

Figure 4.4: Microstructure of the gauge section of the sample from EBSD. (a) Raw EBSD map colored according to the inverse pole figure perpendicular to the surface in (b). White dots correspond to regions that were not indexed by EBSD. The loading axis is horizontal, as indicated by the arrow. (c) Post-processed EBSD map of the rectangular region indicated in (a) at higher magnification. GB are colored according to their misorientation angle in degrees, and the orientation of the hexagonal unit cell is shown at the center of each grain. (d) Basal plane (0001) pole figure. Intensity is marked in multiple of random distributions.

4.3.3 Slip trace and slip transfer analysis

The analysis of 233 grains in the SEM revealed that only prismatic <a> slip took place in the sample, favored by the strong texture. The lack of activation of other basal <a> or pyramidal <c+a> slip systems facilitates the unique identification of the active slip system (slip plane and direction) since the three prismatic planes lead to slip traces with different orientations on the sample surface. It should be noted that the active slip system identification through conventional slip trace analysis is not effective if the slip plane or the Burgers vector is parallel to the sample surface. To avoid this problem, the material and texture were carefully selected for this investigation to limit the number of active slip

systems to avoid the noise and complexity introduced by the activation of many (and different) slip systems [178]. In particular, (1) the prismatic planes are always oblique to the loading direction, and only one or two of them were suitably oriented for slip, and (2) the basal planes (which may be parallel to the sample surface) are very poorly oriented for plastic deformation given the geometry of the hexagonal lattice. Thus, it is very unlikely that other slip systems (besides prismatic) could be active, and any slip traces different from prismatic were not observed throughout the sample. The low CRSS of prismatic slip in pure Ti and the only observation of prismatic slip traces after deformation indicate that prismatic slip is enough to accommodate the plastic deformation in the sample.

Moreover, the deviation between the theoretical slip trace (calculated from the grain orientations obtained from the EBSD of the undeformed sample) and the observed slip trace was always $<5^{\circ}$. These small deviations between the observed and theoretical slip traces can be explained by the change in crystal orientation caused by the plastic deformation of the sample. Once one active prismatic slip system was impinging onto a GB, a number of parameters were measured for that GB. In the case of multiple slip in one or both grains across a GB, the best combinations in terms of the geometrical alignment between the active slip systems were chosen. This means that the two that provide the lowest κ and ψ were chosen in case that double prismatic slip was observed at both sides of a GB among the four possible combinations between the slip systems. The recorded parameters include GB misorientation Θ, the SF of the incoming and outgoing slip systems across the GB, and the four angles that characterize the geometrical alignment between the incoming and outgoing slip systems at the GB on the surface of the sample (κ, ψ, δ, γ) (Fig. 1.5). This information was recorded for 361 GBs considered reliable due to their similitude between EBSD and DCT, and was used to assess the slip transfer criteria.

The active prismatic slip systems were identified on either side of each GB, and they were classified according to the occurrence or absence of slip transfer in three distinct groups. The first group included those GBs in which slip transfer was convincingly observed, as revealed by the visible and unequivocal continuity between all or most of the slip traces at both sides of the boundary (Figs. 4.5 (a) and (b)). In some cases, only one slip system was active in both grains across the GB (Fig. 4.5 (a)), while double slip transfer along two different pairs of slip systems took place in other cases (Fig. 4.5 (b)). Slip transfer in these cases was confirmed by the absence of any changes in surface topography at the GB, indicating that deformation between the neighboring grains was homogeneous.

The second group included those GBs where slip blocking was observed, or in other words, where slip transfer was not observed (Fig. 4.5 (c)). The slip traces were stopped at the GB or did not match at both sides of the GB and, sometimes, feather-shaped microvolumes of deformation appeared near the boundary, indicating the presence of stress concentrations associated with heterogeneous plastic deformation [62, 70, 71]. The presence of a ledge or significant change in the topography at a GB is also indicative of heterogeneous deformation at both sides of the GB, and it is often associated with uncertain or poor slip transfer conditions [26, 185].

The third and last group corresponds to what we define as partial slip transfer (Fig. 4.5 (d)). These cases show slip transfer to some extent but were different from the perfect slip

transfer cases depicted in Fig. 4.5 (a) and (b). For instance, just a few slip bands matched across a GB, or some traces matched but faded away a few micrometers away from the GB.

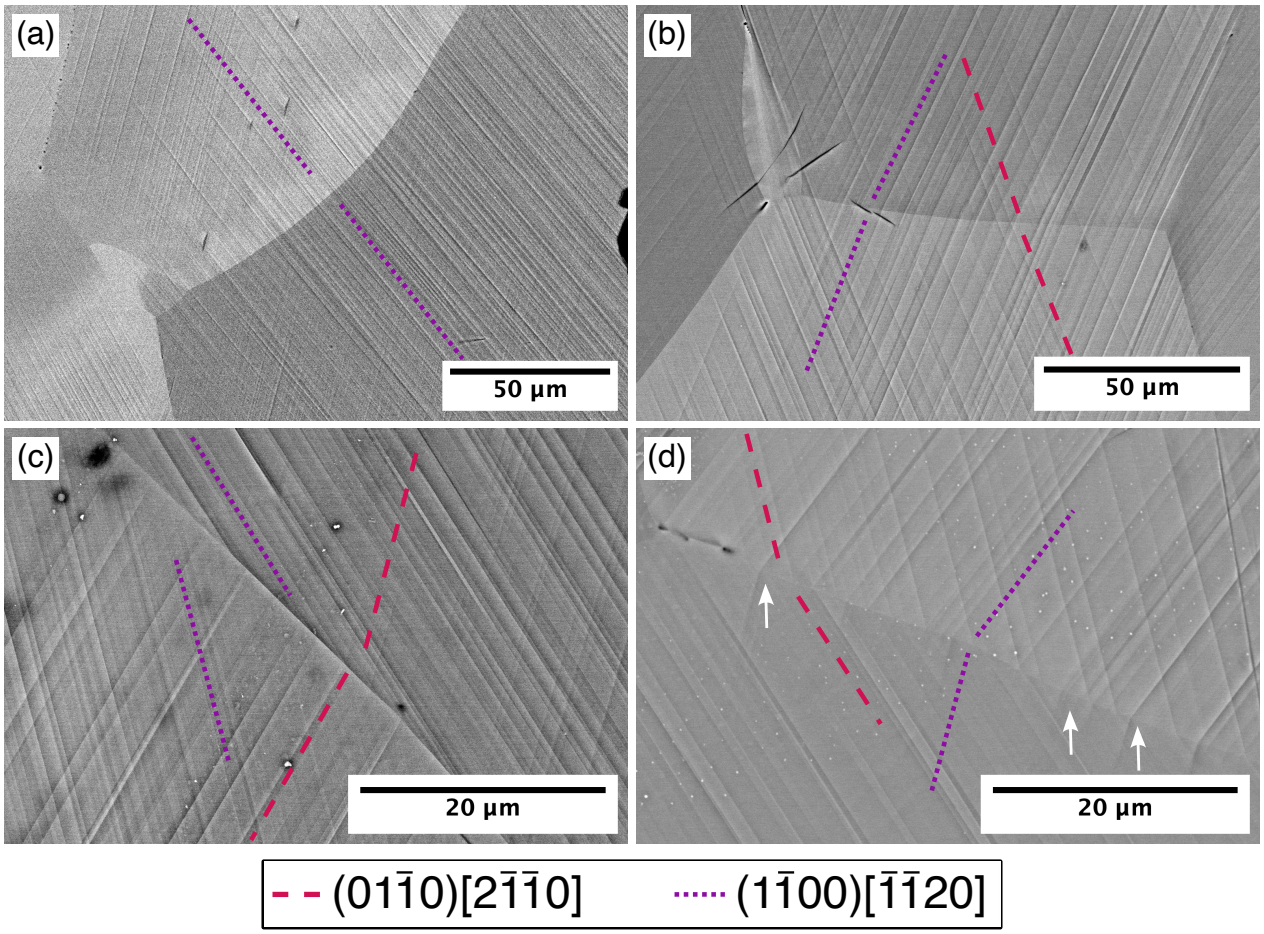

Figure 4.5: Prismatic-to-prismatic slip transfer/blocking across GB. The theoretical orientation of the slip traces of the active slip systems is indicated by the dashed lines. (a) Slip transfer. (b) Double slip transfer. (c) Slip blocking and ledge at the GB. (d) Partial slip transfer. The arrows indicate slip bands fading towards the grain interior.

Out of the 362 analyzed GB, convincing slip transfer was observed in 43.9% and partial slip transfer in 11.6% of the cases, leaving a remaining 44.5% of slip blocking instances (see Fig. 4.6 (a)). Therefore, the likelihood of slip transfer in this sample is distributed in approximately 50-50 fashion, i.e., 50% for partial + full slip transfer and 50% for slip blockage. The relationship between slip transfer, partial slip transfer, and slip blocking with GB misorientation angle is plotted in Fig. 4.6 (b). It shows that slip transfer (either perfect or partial) occurs at low misorientation GBs ($< 30°$). Nevertheless, there are still slip blocking events located at low misorientation GB, suggesting that the GB misorientation angle is not sufficient to predict prismatic-to-prismatic slip transfer across GBs in pure Ti. With a comprehensive database of the geometrical characteristics of the grains and grain boundaries, we can now assess how the different slip transfer criteria perform

for the current Ti sample.

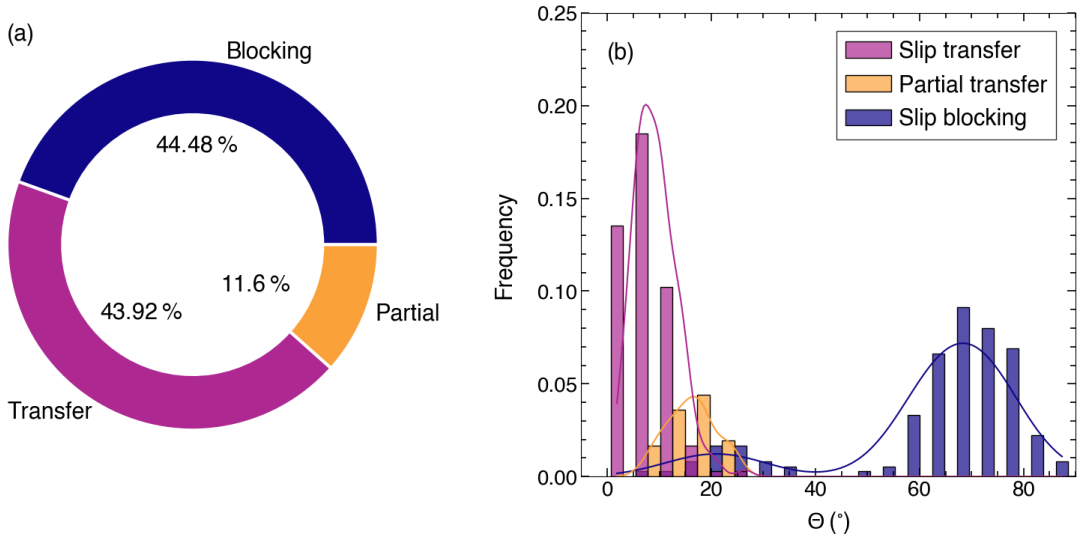

Figure 4.6: Distribution of slip transfer events in the microstructure: (a) Classification of prismatic-to-prismatic perfect slip transfer (purple), partial slip transfer (orange), and slip blocking (dark blue) across GB in Ti, and (b) Influence of GB misorientation angle distribution on the occurrence of perfect slip transfer, partial slip transfer and slip blocking.

4.3.4 Evaluation of slip transfer criteria

The slip transfer criteria presented in the introduction rely on the angles κ, ψ, γ, δ, and θ, in addition to the misorientation angle. All of them can be determined for each GB from the EBSD information of the neighboring grains except for θ, which requires 3D information about the orientation of the GB within the sample, given by $\boldsymbol{n}_{GB}$. This information was determined from the DCT data for 266 GBs out of the 362 analyzed by slip trace analysis (74%). This difference is due to the limitations of the DCT technique to accurately capture the shape and orientation of small grains [60]. Only GBs whose shape was accurately determined by both LabDCT and EBSD were included in the analysis. The twist angle θ was calculated using Eqs. (4.1) and (4.2), which take as input the grain boundary normal, $\boldsymbol{n}_{GB}$, obtained from LabDCT data, and the normals of the active slip planes across the GB, $\boldsymbol{n}_A$ and $\boldsymbol{n}_B$, obtained from the combination of SEM imaging and EBSD crystallographic information.

Traditionally, κ (that determines the residual Burgers vector) and ψ (that captures the misorientation between the incoming and outgoing slip planes) have been considered the most relevant angles to assess slip transfer [26, 82], following the Luster-Morris parameter m'. Their ability to predict slip transfer is shown in Fig. 4.7 (a), which shows that the majority of slip transfer events were found when κ and ψ were $< 20°$, in agreement with previous investigations [7, 24, 130, 154]. In these cases, the incoming and outgoing slip systems are well aligned because the magnitude of the residual dislocation left at the GB is small, and the resolved shear stress acting on the incoming slip system is easily

transmitted to the outgoing slip system because ψ is also small. Moreover, all partial slip transfer instances are located at low to moderate values of these angles ($< 30°$), and all the blocking events are shifted towards higher angles, except for three outliers where there is a ledge at the GB, indicating that plastic deformation at these GBs was not homogeneous. Two of these three outliers correspond to the GB shown in Fig. 4.5 (c), which presents a significant change in topography between the adjacent grains. In this case, two slip blocking instances are observed between both pairs of active slip systems (purple-to-purple and pink-to-pink) despite presenting, in principle, suitable geometrical alignment for slip transfer. The information provided by the conventional slip trace analysis technique is not sufficient to explain why slip transfer is not observed across this GB. Nevertheless, other techniques, such as HRDIC, could be employed to assess the heterogeneous distribution of the deformation and the effect of the local stress on the occurrence of slip transfer.

The occurrence of slip transfer/blocking is plotted in Fig. 4.7 (b) as a function of κ and θ. Perfect slip transfer is associated with low values ($< 20°$) of both angles, but no instances of slip transfer are found if $\kappa > 30°$, regardless of θ. Low values of θ only lead to slip transfer if they are associated with low values of κ. Moreover, many perfect or partial slip transfer instances are found if $\kappa < 25°$ even for very large values of θ. Finally, the occurrence of slip transfer/blocking is plotted in Fig. 4.7 (c) as a function of ψ and θ. Slip transfer is mainly associated with low values of ψ, but there is no obvious trend with θ. Moreover, it should be noted that large values of θ ($< 30°$) can be found even when the incoming and outgoing slip planes are well aligned and $\psi < 20°$. Theoretically, when ψ is small, the slip planes are well aligned, and thereby θ is very small and independent of the GB inclination angle β (Fig. 1.5). However, as ψ increases, the twist angle θ is more sensitive to the GB inclination. Thus, it cannot be concluded that –in general– good alignment between the active slip planes leads to low twist angles, and it is necessary to obtain this information experimentally. Overall, these results seem to indicate that θ plays a secondary role in determining slip transfer/blocking, compared with κ and ψ for the current prismatic-dominated slip transfer. This can be an effect of the strong texture in the sample, where all plastic deformation can be accommodated through prismatic slip. The influence of θ in a randomly oriented sample is still not well understood and could affect slip transfer between prismatic and non-prismatic slip systems.

To obtain more quantitative information, a categorical model was used to assess the influence of the different angles (κ, ψ, θ, δ and γ in Fig. 1.5, together with the GB misorientation Θ calculated from the crystal orientation of the neighbor grains) on the likelihood of slip transfer. To this end, all the data were divided into two categories: slip transfer (including partial slip transfer) and slip blocking. This is a reasonable assumption since partial slip transfer instances do transfer slip to some extent. The occurrence or absence of slip transfer for each GB was characterized by the categorical variable *slip* that can only take the values of 1 or *true* (slip transfer) or 0 or *false* (slip blocking).

The next step was to determine the optimum value of each angle that is able to discriminate slip transfer from slip blocking for each angle. The procedure is schematically shown in Fig. 4.8 (a) for κ. For any value of κ (such as $\kappa = 45°$ in Fig. 4.8 (a)), the data set will be divided into two groups, with $slip = 1$ (slip transfer) to the left of κ and $slip = 0$ (slip

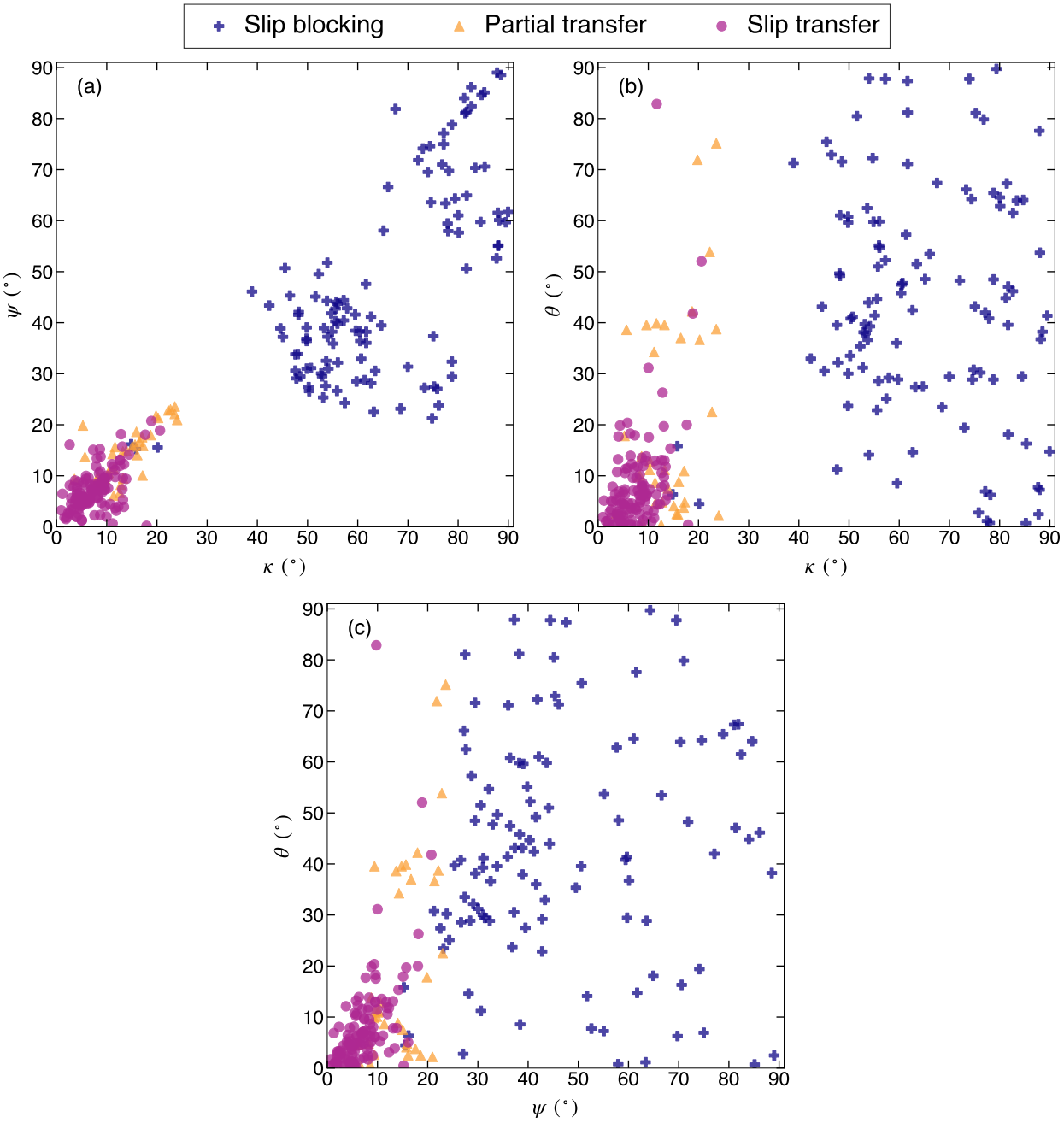

Figure 4.7: Dependence of slip transfer on κ, ψ, and θ: (a) Influence of κ and ψ on the occurrence of slip transfer/blocking across the GB. (b) Influence of κ and θ on the occurrence of slip transfer/blocking across the GB. (c) Influence of ψ and θ on the occurrence of slip transfer/blocking across the GB.

blocking) to the right of κ. This leads to a binary categorical model, where the data can be arranged in a confusion matrix including the true positives (TP), true negatives (TN), false positives (FP), and false negatives (FN), as depicted in Fig. 4.8 (b). Different model classification metrics, such as Precision (Eq. (4.3)) and Recall (Eq. (4.4)) [145, 176], can be

defined as

$$\text{Precision} = \frac{\text{TP}}{\text{TP} + \text{FP}} \tag{4.3}$$

$$\text{Recall} = \frac{\text{TP}}{\text{TP} + \text{FN}}. \tag{4.4}$$

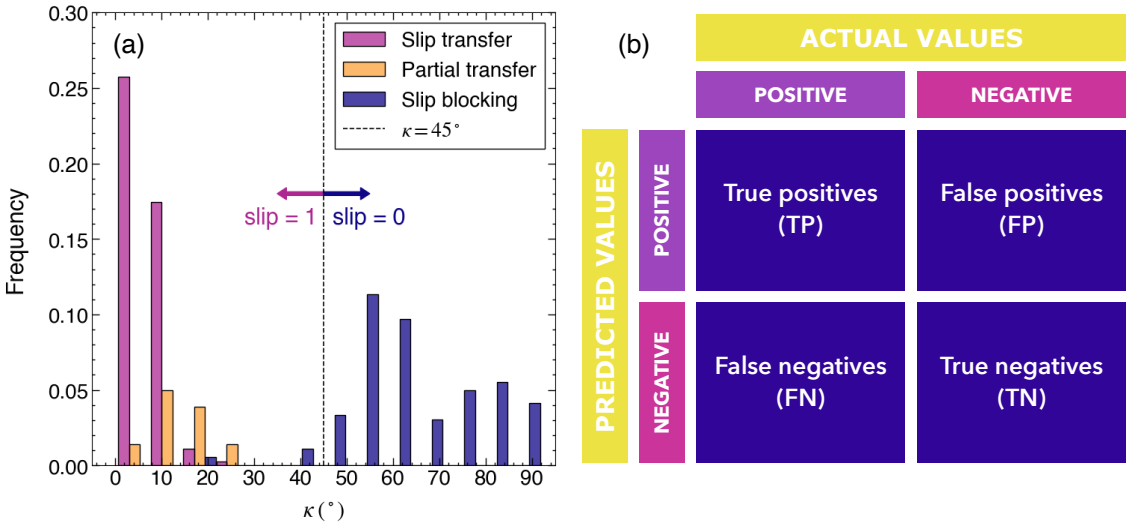

Figure 4.8: (a) Influence of angle κ on slip transfer, partial slip transfer, and slip blocking. A black vertical dashed line is drawn in $\kappa = 45°$ to represent a potential threshold that divides the data in predicted slip events ($slip = 1$) to the left of the line and predicted blocking events ($slip = 0$) to the right of the line. (b) Schematic representation of a confusion matrix to compare the actual and predicted values slip transfer/blocking for any categorical variable.

Precision or confidence deals with the "Predicted positive" row of the confusion matrix, determining how accurate the model is in predicting the positive outcomes out of all the predicted outcomes. Recall, or sensitivity, deals with the "Actual positive" column of the confusion matrix and measures the completeness of the positive predictions or how accurately the model was able to identify the positive outcomes out of all positive outcomes that were actually present. In other words, Precision indicates the accuracy of the positive predictions, whereas Recall refers to the percentage of positive values correctly classified by the model. In a model with 100% Precision, there are no false positives, and every positive prediction is correct, whereas with 100% Recall, there are no false negatives, and every negative prediction is correct.

Any of these metrics can be used to evaluate the performance of any categorical model, depending on the specific purpose of the model. However, they have to be combined into a single metric when precision and recall are equally important. This is normally achieved through the F1 score [176]

$$\mathrm{F1} = 2 \cdot \frac{\mathrm{Precision} \cdot \mathrm{Recall}}{\mathrm{Precision} + \mathrm{Recall}} \tag{4.5}$$

that can be interpreted as a measure of overall model performance ranging from 0 (worst) to 1 (best).

The threshold value for slip transfer for all the angles that characterize the GB was assessed from the maximum value of F1, and the results are summarized in Table 4.1. They show very similarly low values for the GB misorientation Θ, κ, ψ, and θ, and very similarly high values for δ and γ. However, the predictions for each angle are not similarly accurate; the higher the optimum F1, the better this angle can predict slip transfer/blocking. This information is summarized in the F1 score matrix (Fig. 4.9), which shows the maximum value of F1 for each angle in the diagonal of the matrix as well as the maximum F1 that can be obtained by choosing any pairwise combination of two angles with their respective thresholds presented in Table 4.1. The F1 score has been used as a heat map variable; therefore, the colors of each box in the matrix represent the magnitude of F1 compared to the other boxes.

According to the data in Fig. 4.9, the best indicator of slip transfer is $\kappa < 24.5°$, with F1 = 0.993. The F1 values for all the out-of-diagonal terms are smaller than this value, which means that the combination of two angles does not lead to better predictive performance for the current microstructure. It is also worth mentioning that combining three or more angular parameters leads to worse results than those presented in Fig. 4.9. The next best performances are attained by the pairwise combinations of misorientation Θ, κ, and ψ, whereas the performance of criteria based on the θ angle always attains the poorest performances to predict slip transfer/blocking. It should be noted that these findings may differ for a more random microstructure, and further exploration is needed to assess more diverse cases.

Table 4.1: Threshold angle (according to the F1 score) to predict slip transfer.

Angle	*Threshold angle*
Θ	$< 24.5°$
κ	$< 24.5°$
ψ	$< 23°$
θ	$< 23°$
δ	$> 74°$
γ	$< 78.5°$

A similar analysis was carried out to assess the performance of the slip transfer criteria presented in the introduction of this paper, namely GB misorientation angle Θ, Luster-Morris parameter m', normalized Burgers vector $\Delta b/b$, LRB, and N. The corresponding threshold values of each parameter for slip transfer that led to the highest F1 score are shown in Table 4.2. These thresholds were used as the best possible separation between the slip

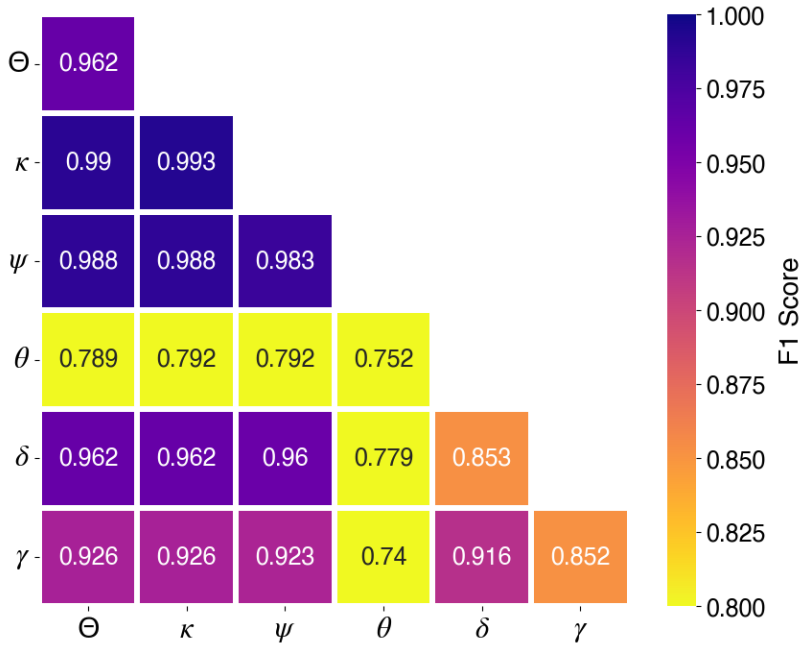

Figure 4.9: F1 score matrix for slip transfer/blocking. The diagonal terms represent the performance of a single angle in terms of the F1 score, whereas the out-of-diagonal terms represent the F1 score obtained by the combination of two angles. The F1 score value is indicated in each box and represented as a heat map variable, ranging from yellow (lowest) to blue (highest). The threshold that leads to the maximum F1 for each angle is depicted in Table 4.1.

transfer and blocking populations, and the corresponding F1 score matrix is presented in Fig. 4.10.

Besides low misorientation angles, slip transfer is likely to occur for low $\Delta b/b$ and high m' and N. The accuracy of these thresholds to predict the slip transfer/blocking, according to the F1 score, is shown in Fig. 4.10. The best performance is obtained with either $\Delta b/b$ or m', which leads to F1 = 0.993. Other slip transfer criteria (N and Θ) lead to lower F1 scores, while the LRB criterion gives the lowest F1 metric, indicating that it is not a good criterion to predict prismatic-to-prismatic slip transfer/blocking at GBs in Ti. The combination of two slip transfer criteria (for instance, $\Delta b/b$ and m', $\Delta b/b$ and N, m' and N) improves the F1 score up to the values obtained with only $\Delta b/b$ or m' but not more. On the contrary, the F1 score of LRB or any combination of LRB with another criterion is much lower, indicating that LRB is not a reliable criterion for slip transfer/blocking for this particular system.

4.4 Discussion

The results presented in the previous section provide the first assessment of slip transfer across GBs in polycrystalline metals in which a) the active slip systems across the GB

Table 4.2: Optimum threshold (for maximum F1 score) for different well-known slip transfer criteria.

Parameter	*Threshold*
Θ	$< 24.5°$
m'	> 0.8
$\Delta b/b$	< 0.45
LRB	> 0.65
N	> 0.9

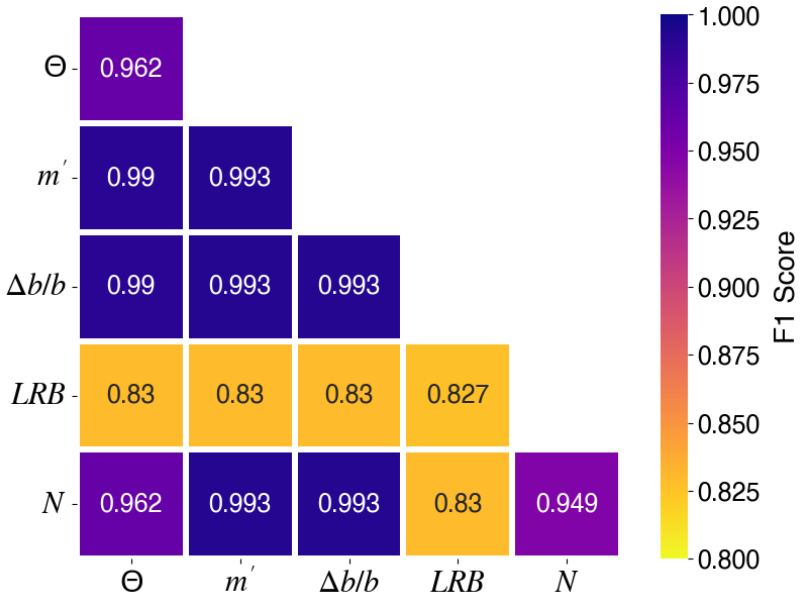

Figure 4.10: F1 score matrix for slip transfer/blocking. The diagonal terms represent the performance of a single slip transfer criterion in terms of the F1 score, whereas the out-of-diagonal terms represent the F1 score obtained by the combination of two slip transfer criteria. The F1 score value is indicated in each box and represented as a heat map variable, ranging from yellow (lowest) to blue (highest). The threshold that leads to the maximum F1 for each slip transfer criterion is depicted in Table 4.2.

are actually identified, b) the GB geometry is fully characterized in 3D and c) slip transfer/blocking data are obtained in a statistically significant number of GBs. These unique advantages allow us to robustly identify the governing geometrical parameters that impact the slip transfer in our prismatic slip-dominated Ti sample.

One of the primary conclusions of the analysis of the data is that the normalized residual Burgers vector across the GB, $\Delta b/b$, appears to be the best criterion to predict slip transfer, which is likely to occur if $\Delta b/b < 0.45$ (or $\kappa < 24.5°$) while slip blocking will be dominant otherwise. Similar scores are obtained in the case of m', which includes information about the residual Burgers vector and the angle ψ between the normals of the incoming and the

outgoing slip planes, which are related to the resolved shear stresses in both planes.

It should be noted, however, that the particular texture of the Ti sample leads to the presence of two prismatic planes in each grain with very high SF. Thus, if $\Delta b/b$ is small and there is no large barrier for slip transfer, the incoming dislocations will likely find another slip system with a high resolved shear stress in the neighbor grain that will be available to accommodate slip transfer. Thus, it is possible that m' (that includes the information about the residual Burgers vector) becomes a better predictor of slip transfer/blocking in other microstructures. These results generally agree with previous investigations based on surface observations in different polycrystalline metals [7, 24, 26, 82, 130].

The second main conclusion of this analysis is that the twist angle θ (and, thus, the LRB criterion) does not appear to be a good predictor of slip transfer/blocking for the grain orientations in the prismatic slip-dominated Ti sample tested here. Many instances of perfect and partial slip transfer were found for high values of θ, and slip transfer never occurred for low values of θ unless the residual Burgers vector was also small (Fig. 4.7 (b). This result is, to some extent, surprising because the limited information available in the literature seemed to indicate that θ played a major role in slip transfer. Zhou *et al.* [200] studied basal-to-prismatic and basal-to-pyramidal slip transfer in a Mg alloy. The actual basal slip system was determined using lattice-rotation analyses, and slip transfer was reported in 23 cases, corresponding to high m' in 16 cases and low $\Delta b/b$ in 21 cases. The GB orientation was measured by sectional grinding in one of the cases with slip transfer and low m', and it was found that $\theta = 26°$. Nevertheless, θ was not measured (but estimated) in other cases with slip transfer and low m', and solid conclusions could not be reached. Besides that, low $\Delta b/b$ seems to be a very good predictor of basal-to-prismatic and basal-to-pyramidal slip transfer in Mg.

Furthermore, Sarebanzadeh *et al.* [154] recently carried out a detailed analysis of basal-to-basal slip transfer in pure Mg. The actual active basal slip system in each grain was carefully identified by means of slip trace - modified lattice rotation analysis [190] and slip blocking when $m' < 0.45$ and $\Delta b/b < 0.6$ was only found in a few cases, that were analyzed in detail. They corresponded to situations in which basal slip was almost parallel to the GB (and, thus, slip lines did not cross the boundary) or to five cases in which the GB orientation was measured through the thickness through sequential FIB. $\theta > 60°$ in all these cases, and it was concluded that high twist angles may hinder basal to-basal slip transfer in Mg. In fact, the actual slip transfer mechanism for high twist angles is not known, and it has been suggested [73] that the activation of secondary slip systems (such as <a> basal or pyramidal slip in Ti) is needed near the GB to accommodate slip transfer between the primary prismatic slip systems when θ is high. While this is possible in Ti, because the critical resolved shear stress for <a> basal slip is not far away from that for <a> prismatic slip, this is unlikely to happen in Mg, in which the critical resolved stress for <a> basal slip is much lower than for other slip systems, blocking slip transfer for high twist angles. Zhou *et al.* [200] measured subsurface dislocation activity by differential aperture X-ray microdiffraction in five grains and found that <c+a> dislocations were active, but their activity did not appear at the surface. This observation implies that other unexpected dislocation sources may be assisting the slip transfer process under the

surface.

In the case of special GBs, such as twin boundaries, the effect of the twist angle can be assessed because the GB normal can be directly determined from the known crystallographic rotation between the parent and the twin. Genée *et al.* [62] analyzed slip transfer across $\Sigma 3$ annealing twin boundaries in a Ni-based superalloy and reported that the θ was the main geometrical parameter determining slip transmission across twin boundaries, where $\theta = 0°$ appeared as a necessary condition for slip transfer. Chen *et al.* [38] performed uniaxial tensile testing at $650°C$ in Inconel 718 Ni-based superalloy and also reported that $\theta = 0°$ and $\Delta b < 0.6b$ are sufficient conditions to ensure slip transfer across twin boundaries. However, the actual pair of active slip systems across the twin boundary was dictated by the maximum Schmid factor and was not conclusively established. Nieto-Valeiras and LLorca [130] acquired a significant number of slip transfer/blocking occurrences across grain and twin boundaries in a pure Ni sample deformed in tension. Slip transfer across twin boundaries was only observed when $\Delta b \approx 0$, regardless of the twist angle θ, which pointed out that slip transfer across annealing twins seems to be controlled by dislocation cross slip. Regarding regular grain boundaries, the effect of θ was not assessed due to the lack of information about the GB normal, but slip transfer was generally observed when $m' > 0.8$.

It should be finally noted that - given the experimental difficulties in measuring the GB orientation through the thickness of polycrystalline samples - some studies have assumed that GB is perpendicular to the sample surface [38, 62, 103] to study the effect of θ on the likelihood of slip transmission. Under this assumption, Genée *et al.* [62] determined that slip transfer was mostly observed for $\theta < 30°$, although it was also found for higher twist angles $> 40°$. Similarly, Chen *et al.* [38] stated that slip transfer was likely to occur when $\mathrm{LRB} > 0.82$, but several slip blocking instances were found at high LRB values while slip transfer was also observed below such threshold. However, this hypothesis may lead to large errors in the evaluation of θ and thus on LRB.

Thus, the experimental information obtained in this work provides -for the first time- sound evidence that prismatic-to-prismatic slip transfer across regular GBs in Ti is favored by a minimum magnitude of the residual Burgers vector and also by the good alignment between the incoming and outgoing slip planes, while the twist angle plays a secondary role in the process. However, it is important to mention that the negligible effect of the twist angle, in this case, could be affected by the strong texture present in the sample, which could lead to easier plastic deformation accommodation. The influence of the twist angle could still be important for slip transfer between non-prismatic slip systems in randomly oriented Ti samples.

This investigation showed that some of the simple geometrical slip transfer criteria (i.e., those based in Δb and m') can be used to assess slip transfer/blocking in > 99% of the GBs and, thus, are suitable to be incorporated into crystal plasticity models to simulate the behavior of polycrystals. In addition, large twist angles do not hinder prismatic-to-prismatic slip in Ti. However, there are a few GBs within the analyzed dataset whose behavior does not follow these geometrical criteria. These outliers could be caused by the local stress distribution in the GB neighborhoods, which may change the local SF, hindering slip transfer.

As mentioned in the introduction (1.3), conventional slip trace analysis does not provide any information about the strain heterogeneity within the sample, and other techniques, such as HRDIC, are required in order to assess the effect of the local stress state around GBs on the likelihood of slip transfer.

4.5 Conclusions

In this chapter, slip transfer across GBs was analyzed by means of SEM-based slip trace analysis and electron backscatter diffraction in a thin Ti sample which presented a strong rolling texture. The two-dimensional microstructural analysis was combined with three-dimensional grain maps, procured through LabDCT, which allowed for the determination of 3D grain shapes and the orientation of grain boundaries within the sample. After a thorough characterization, the sample was loaded in tension, which resulted in the activation of its <a> prismatic slip systems. The orientation of the active prismatic slip system(s) in each grain was determined from the orientation of the slip traces, and slip transfer/blocking was analyzed in > 300 GBs on the sample surface. The likelihood of slip transfer/blocking as a function of the main angles that characterize the incoming and outgoing slip systems and the grain boundary (misorientation angle Θ, κ, ψ, θ, γ and δ) was assessed by means of the "F1 score" within the framework of categorical models. The analysis was further extended to assess the efficacy of widely used slip transfer criteria available in the literature (Θ, $\Delta b/b$, m', LRB, and N). Via a thorough analysis of the various geometric characteristics of grains and grain boundaries, we arrived at the following observations:

1. For the current prismatic slip-dominated Ti sample, the best angle to predict slip transfer was the angle between the incoming and outgoing slip directions, with $\kappa < 24.5^\circ$ as the threshold for slip transfer with an F1 score of 0.993.
2. The next best performances were attained by the pairwise combinations of grain boundary misorientation angle Θ and the angles between incoming and outgoing Burgers vectors and slip planes, κ, and ψ.
3. Interestingly, the predictions for slip transfer based on the twist angle θ resulted in the poorest performance for the current prismatic slip-dominated system.
4. From the slip transfer criteria available in the literature, the best performance was obtained with either $\Delta b/b$ or m' slip transfer criteria (that lead to an F1 score of 0.993) while other slip transfer criteria (based on N and or the misorientation angle), led to lower F1 scores, with the LRB criterion giving the lowest F1 metric.
5. The combination of two slip transfer criteria (for instance, $\Delta b/b$ and m', $\Delta b/b$ and N, m' and N) improved the F1 score up to the values obtained with only $\Delta b/b$ or m', but not more.
6. In contrast, any combination of LRB with another criterion led to much lower F1 scores, indicating that LRB was not a reliable criterion to predict prismatic-to-prismatic slip transfer/blocking at GBs in the current Ti sample.

The results of this analysis highlight the effectiveness of combining established characterization techniques like EBSD and SEM with newer methods, like LabDCT, in thoroughly decoding the mechanisms of slip transfer in metals. The study has delivered substantial evidence that, in the case of the prismatic-slip dominated Ti sample, prismatic-to-prismatic slip transfer across regular GBs in Ti is facilitated by a minimal residual Burgers vector and a favorable alignment between the incoming and outgoing slip planes. The methodology demonstrated in this chapter could assist in shedding light on the comparative influence of the different geometrical parameters in more diverse slip systems.

Nevertheless, a few GBs in the dataset presented slip blocking when slip transfer should be active according to the geometrical criteria. This abnormal slip transfer phenomenon could be caused by the local stress state near those GBs, and HRDIC will be used in the next chapter to assess this behavior.

5 Analysis of slip transfer in pure Ti through HRDIC

5.1 Introduction

The geometrical slip transfer criteria have been successfully used to predict slip transfer/blocking across GBs in metallic materials [19, 91]. Nevertheless, they are not always accurate, and slip blocking is sometimes found in GBs with good geometrical alignment and vice versa [70, 88, 131, 154]. These deviations from the regular behavior were attributed to two main reasons: the precise identification of the active slip systems across the GB and the influence of the twist angle θ that cannot be obtained from surface information. These limitations were overcome in the previous chapter (Chapter 4) through the choice of a Ti sample with only prismatic slip activity and the use of LabDCT to scan the microstructure in 3D. Thus, the active slip system was uniquely identified, and the twist angle θ was calculated.

Nevertheless, several outliers were still found within the data, and slip blocking or partial slip transmission (i.e. just a few slip bands matched across a GB or some traces matched but then faded away a few micrometers away from the GB) was found in GBs that were suitably oriented for slip transfer. These results point out the complexity of the slip transfer process in which good alignment between incoming and outgoing slip systems seems to be necessary, but no sufficient condition and other factors may be relevant. For instance, the applied stress (that controls the driving force for slip activation) may lead to slip transfer once a minimum threshold is overcome, or the activation of cross-slip may be necessary to allow slip transfer when the twist angle is high [73]. This latter mechanism would explain why θ angles impede basal-to-basal slip transfer in Mg (because cross-slip from prismatic or pyramidal is very difficult due to the large critical resolved shear stresses) but nor prismatic-to-prismatic slip transfer in Ti.

HRDIC appears as a powerful tool for quantifying the strain heterogeneity near GBs in polycrystalline metals and ascertaining other processes that affect slip transfer/blocking at GBs. Unlike conventional EBSD-based slip trace analysis, HRDIC can capture the surface strains at the sub-grain scale, where plasticity is localized at individual slip bands, GBs, and triple junctions. Different investigations have used this technique to examine

the spatial distribution and the slip characteristics in Ni-based superalloys [79, 167], and others have attempted to correlate the dislocation-GB interactions with the plastic strain heterogeneity at the GB neighborhood. Other works have analyzed slip transfer and the plastic strain concentrations via HRDIC in Ni-based superalloys [2], FeCr BCC alloys [140], or TiAl alloys [65]. Thus, HRDIC can provide extra information about the local plastic strains near the GB that can be used to elucidate other factors –besides good alignment– that control slip transfer at GBs.

In this chapter, HRDIC has been used to assess slip transfer/blocking in a pure Ti foil as a function of the applied strain. The microstructure of the sample was characterized in 3D using DCT to have all the geometrical parameters that describe the slip configuration across a GB, especially the twist angle θ. The occurrence or absence of slip transfer at different deformations was ascertained from the observation of the slip bands in the shear strain HRDIC maps, which also provided information about the strain heterogeneity in the specimen after plastic deformation. Then, the well-known geometrical slip transfer criteria were tested for every GB analyzed to evaluate their performance to predict the likelihood of slip transmission, and particular attention was paid to those GBs in which the geometrical criteria failed.

5.2 Materials and methods

A similar sample to that used in Chapter 4 (Fig. 4.1) was employed, with identical heat treatment and sample preparation.

5.2.1 Microstructural characterization

EBSD maps of the gauge section of the sample were acquired before and after mechanical deformation. The crystallographic orientations were collected in an FEI Helios NanoLab 600i dual-beam microscope with an Oxford Instruments EBSD detector. The whole gauge length was mapped by the serial acquisition of several overlapping maps, followed by stitching in AZtec. The EBSD maps were acquired at 20 kV and 2.7 nA, with 3 μm step size for the maps before deformation (in which the whole gauge was mapped) and 0.6 μm after deformation in the selected region to accurately capture the crystallographic orientation gradients. The overall quality of the EBSD maps was above 95% indexing. The maps were post-processed with the MTEX Matlab Toolbox [14], and the GB misorientation threshold was set to 2° to capture low-angle GBs.

The microstructure of the sample was characterized in 3D using a Zeiss Xradia Versa 620 X-ray microscope with a DCT pro module [13]. The diffraction contrast data was collected following a helical phyllotaxis high aspect ratio tomography strategy, where the vertical and the rotational motion are combined to capture the entire sample in a single scan, as explained in Chapter 3. The flat panel detector was used to capture the diffraction spots, and a projection geometry was employed for this scan by positioning the source 14.5 mm from the sample and the detector 245 mm from the sample. The source voltage and power were set to 110 kV and 10 W, respectively. An exposure time of 15 seconds was used per

projection to ensure a good signal-to-noise ratio. The different regions of the sample were illuminated with a polychromatic beam through a letterbox aperture of 250×750 μm^2. A total of 3032 diffraction projections were collected to cover the entire gauge section, resulting in a total scan time of 13 hours. The advantages of helical phyllotaxis as compared with conventional DCT scanning have been recently reported [60, 134], and explained in Chapter 3.

The acquired DCT projections were reconstructed with GrainMapper3D (Xnovo Technology) using the forward modeling approach [132] until the average completeness values reached at least 90%. Then, Dream3D [69] was used to segment the volume into grains and GBs, and Paraview [12] was used for visualization purposes. The DCT acquisition strategy and post-processing workflow are detailed in Chapter 3.

The reconstructed sections were denoised and segmented in Dream3D using a minimum completeness value of 0.1 and a GB misorientation threshold of 2° to characterize the GBs in 3D. Then, the spurious data were filled using an erode/dilate process with two iterations. Once the volume of the sample was reconstructed, a triangular surface mesh was generated over the inner GBs and outer surfaces of the samples. The initial triangular surface mesh was smoothed using a Laplacian smoothing algorithm to avoid the stair-stepped appearance, and the resulting triangle data (triangle id, centroid, area, curvature, misorientation, and normal direction) were exported for further analysis. The reconstructed volume of the sample is shown in Fig. 5.1 (a), where the region of interest (ROI) is displayed along with the smooth surface mesh generated at the GBs. The surfaces within the triangular mesh are colored according to the GB numerical identifier. The grains within the studied ROI are colored according to the inverse pole figure plotted in Fig. 5.1 (b). Fig. 5.1 (c) shows a close-up view of a pair of grains within the ROI, where the volume reconstructed with voxels (cubic elements) is shown on the left, and the smoothed GBs are shown on the right.

The normal vector to each triangle in the surface mesh was directly obtained from the surface mesh, and the GB normal direction was estimated. To this end, a different subset was generated for every GB from the triangular mesh, so only the corresponding triangle normals were selected. The triangle winding was carefully checked and corrected so that all normal directions were pointing in the same direction. Given that the mean curvature of the studied GBs is close to 0, the GB normal was taken as the mean of the triangle normals included in the surface.

5.2.2 High-resolution digital image correlation

HRDIC was used to capture the heterogeneous strain distribution and assess slip transfer at different applied strains in the sample. An Au nano-speckle pattern was created on the surface of the gauge section of the sample- To this end, a fine Au layer of ~ 15 nm was deposited by sputtering on the electropolished surface, followed by remodeling in a saturated water vapor environment for 3 hours at 350 °C, as indicated in [66]. A small ROI was mapped in the SEM, followed by tile stitching and further correlation. The individual images were acquired in a Thermo Scientific Apreo 2S scanning electron microscope at 5

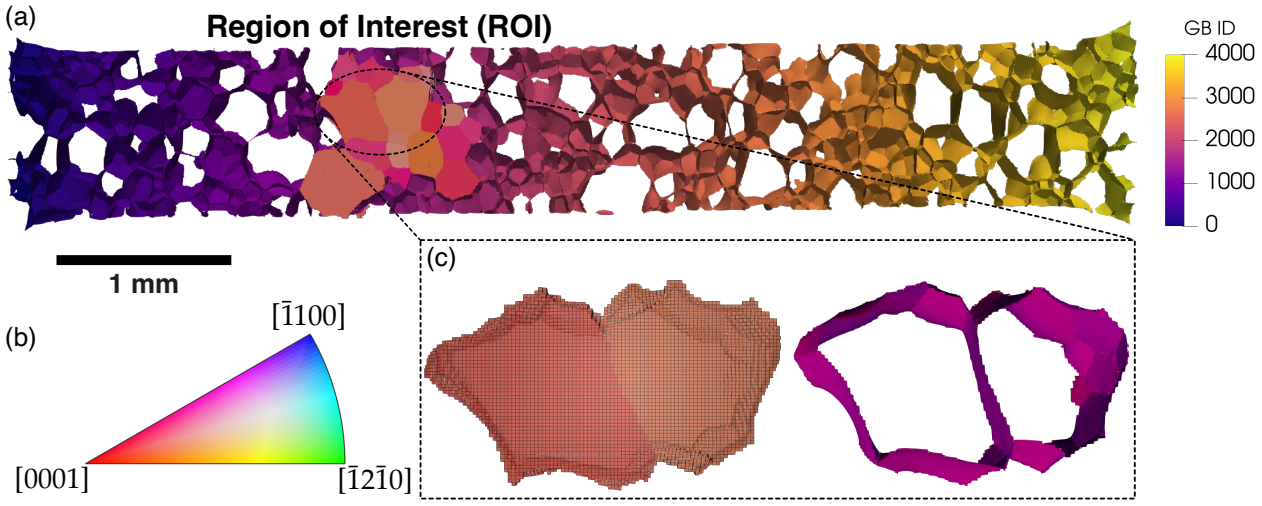

Figure 5.1: Microstructural characterization by DCT. (a) Reconstructed DCT map of the sample gauge, where the grains of the ROI have been colored according to the inverse pole figure with respect to the screen plane (color key in (b)). The region outside the ROI corresponds to the surface mesh generated at the GB, colored according to an integer number given to each GB (GB identifier). (c) Detailed view of two neighbor grains in the ROI, where the reconstructed voxelized volume is shown on the left and the corresponding surface mesh on the right.

kV voltage and 1.6 nA probe current to maximize spatial resolution. Moreover, the image quality was improved using the in-lens backscatter detector to achieve optimum contrast between the Ti substrate and the Au pattern. The working distance was set to 4.5 mm to maximize the signal-to-noise ratio, and every tile had a resolution of 1536×1024 pixels and a pixel size of ~ 65 nm. A representative SEM image of the Au pattern on the Ti sample for HRDIC is shown in Fig. 5.2 (a), where the nano-sized Au pattern (white particles) is homogeneously distributed onto the sample surface (black background). The particle size distribution was calculated using ImageJ standard particle size analysis procedures, depicted in Fig. 5.2 (b). The diameter of most Au particles is below 150 nm, thereby providing a suitable pattern to resolve microstructural features such as slip bands.

HRDIC provides the 2D full-field displacement tensor, which allows the calculation of the in-plane strain tensor. However, the effective shear strain, γ_{eff}, is a suitable metric of the heterogeneous strain in the metallic samples since plastic deformation in metals at room temperature occurs mainly dislocation slip [66]. It can be expressed as follows,

$$\gamma_{eff} = \sqrt{\left(\frac{\frac{\partial u}{\partial x} - \frac{\partial v}{\partial y}}{2}\right)^2 + \left(\frac{\frac{\partial u}{\partial y} - \frac{\partial v}{\partial x}}{2}\right)^2} \tag{5.1}$$

where u and v represent the horizontal and vertical components of the displacement field, respectively.

The background noise induced by the SEM operation was also assessed under the same

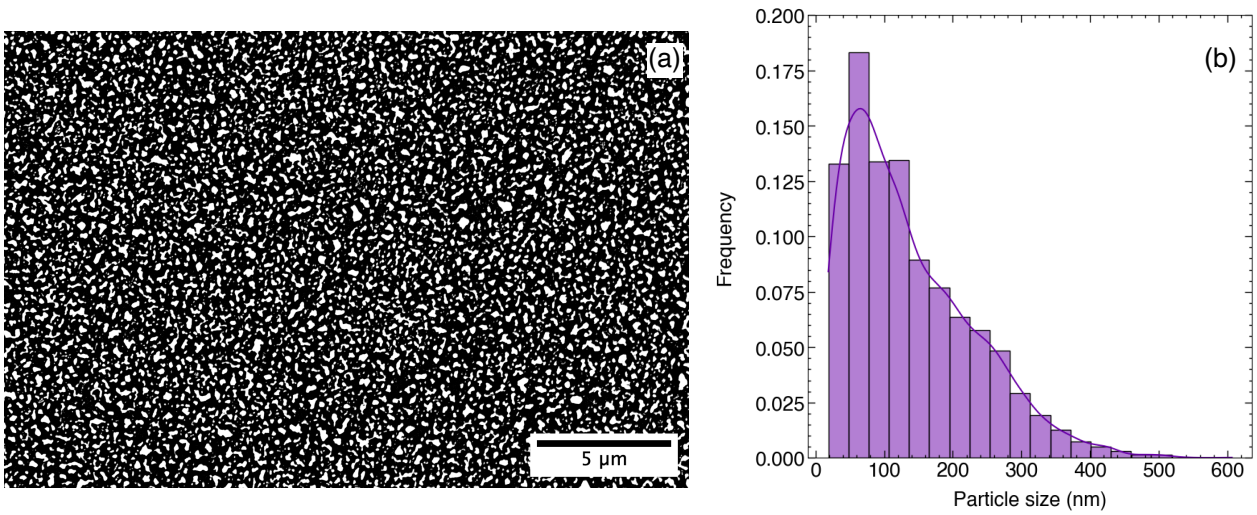

Figure 5.2: (a) Backscattered electrons image of the Au pattern on the Ti sample. The black background corresponds to the Ti substrate and the white speckles to the Au nano-sized pattern. (b) Au particle size distribution.

imaging conditions described above. The stage movement error was determined by the correlation between two images taken at the exact location after random movement of the SEM stage. The error was estimated as the mean shear strain in the correlated map and was below 0.98%. The error induced by the raster scanning during the image acquisition process was assessed by the consecutive acquisition of two images at the exact location. The correlation of these maps leads to an error of 0.74%. This means that the errors induced by the SEM were below 1% shear strain for any HRDIC maps taken under these imaging conditions. Finally, the out-of-plane pseudo-strain error –the error introduced by the movement of the grains out of the sample plane– can also be estimated. To this end, several images were acquired at the exact location for different defocusing conditions, ranging from -30 to 30 μm, to simulate an out-of-plane state. The images were correlated with the image at the focus condition pairwise, and the average effective shear strain was recorded for each of them and plotted against the defocus distance. This representation leads to a u-shaped curve, where the maximum error is located at the extreme defocus distances of -30 and 30 μm, keeping the symmetry along the y-axis from the focus condition at 0 defocus. The primary outcome of this error determination was that any out-of-plane displacement below $\pm 10\ \mu m$ leads to an average shear strain of a maximum of 1% under these imaging conditions. There are no expected out-of-plane displacements above 10 μm for the small applied deformations in this investigation, and hence, the induced systematic pseudo-strains will be negligible. It should be mentioned that no spatial drifts were observed in the error distribution measured by these three methods.

Three different areas of study were mapped as grids of 6×6 individual images or tiles acquired with a 15% overlap to enable seamless stitching into a larger map. The images of the gold nano-speckle pattern after deformation were obtained after unloading. The total field of view of the stitched map was $\sim 525 \times 350 \mu m^2$, and the tiles were stitched together with a linear blending fusion algorithm provided by the Grid/Collection stitching plugin

included in the Fiji distribution of ImageJ [156]. The stitched maps after deformation were correlated with the map in the undeformed state with LaVision's commercial software DaVis 10 [104] using an interrogation window of 6×6 which corresponds to a sub-region size of 390×390 nm^2. The correlated maps obtained from DaVis 10 were post-processed and analyzed with the DefDAP deformation data analysis Python package [10].

5.2.3 Mechanical testing

The sample was deformed in tension in a Kammrath and Weiss micro-testing module equipped with a 1 kN load cell at a quasi-static strain rate of $\approx 10^{-3}\ s^{-1}$ and sequentially deformed three times *ex-situ* until approximately 1%, 2.5%, and 4.5% plastic deformation. After each deformation step, the sample was removed from the machine, and three different HRDIC maps within the ROI were acquired in the SEM.

5.3 Results and discussion

5.3.1 Slip transfer assessment from HRDIC data

The identification of the active slip systems from the HRDIC maps relies on the crystal orientations before plastic deformation provided by EBSD. The theoretical slip traces of the different slip systems in the crystal lattice of HCP-Ti are compared to those observed in the HRDIC maps to identify the active slip system(s) in each grain. The EBSD maps acquired within the ROI are presented in Fig. 5.3, (a) before plastic deformation, and (b) and (d) after 4.5% plastic deformation.

The crystal orientations before deformation are homogeneous, whereas orientation gradients are visible within several grains (G_{19}, G_{22} or G_{23} in 5.3 (b), or G_{11} and G_{12} in 5.3 (d)) after deformation. The EBSD maps acquired after plastic deformation present some non-indexed pixels, which in the case of G_{27} correspond to deformation twins. On the contrary, the non-indexed points in the EBSD map displayed in 5.3 (d) are caused by surface scratches and dirt deposited onto the Au speckle pattern. The *ex-situ* tensile test stress-plastic strain curve is presented in 5.3 (c), where the relevant steps of the experimental process have been labeled as def_i for the HRDIC maps and EBSD_i for the EBSD maps.

As shown in Fig. 5.3 (a), three HRDIC maps were acquired within the ROI after each applied deformation and correlated with the undeformed map. The effective shear strain maps (calculated from Eq. 5.1) acquired by HRDIC within the first sub-region of the ROI are depicted in Fig. 5.4. The slip traces of the active slip systems active 1% plastic deformation are visible and identified as prismatic slip bands in all cases, as revealed by the comparison with the theoretical slip traces (Fig. 5.4 (d)). The slip band intensity and the number of active slip bands generally increase while the slip band spacing decreases as plastic deformation increases. Furthermore, double prismatic slip can be observed in some cases from the first applied deformation (G_{12} in Fig. 5.4 (a)), while the secondary prismatic slip systems get activated after certain deformation in other cases (G_{11} in Fig. 5.4 (b)). After 2.5% plastic deformation, strain concentrations arise at GBs and triple junc-

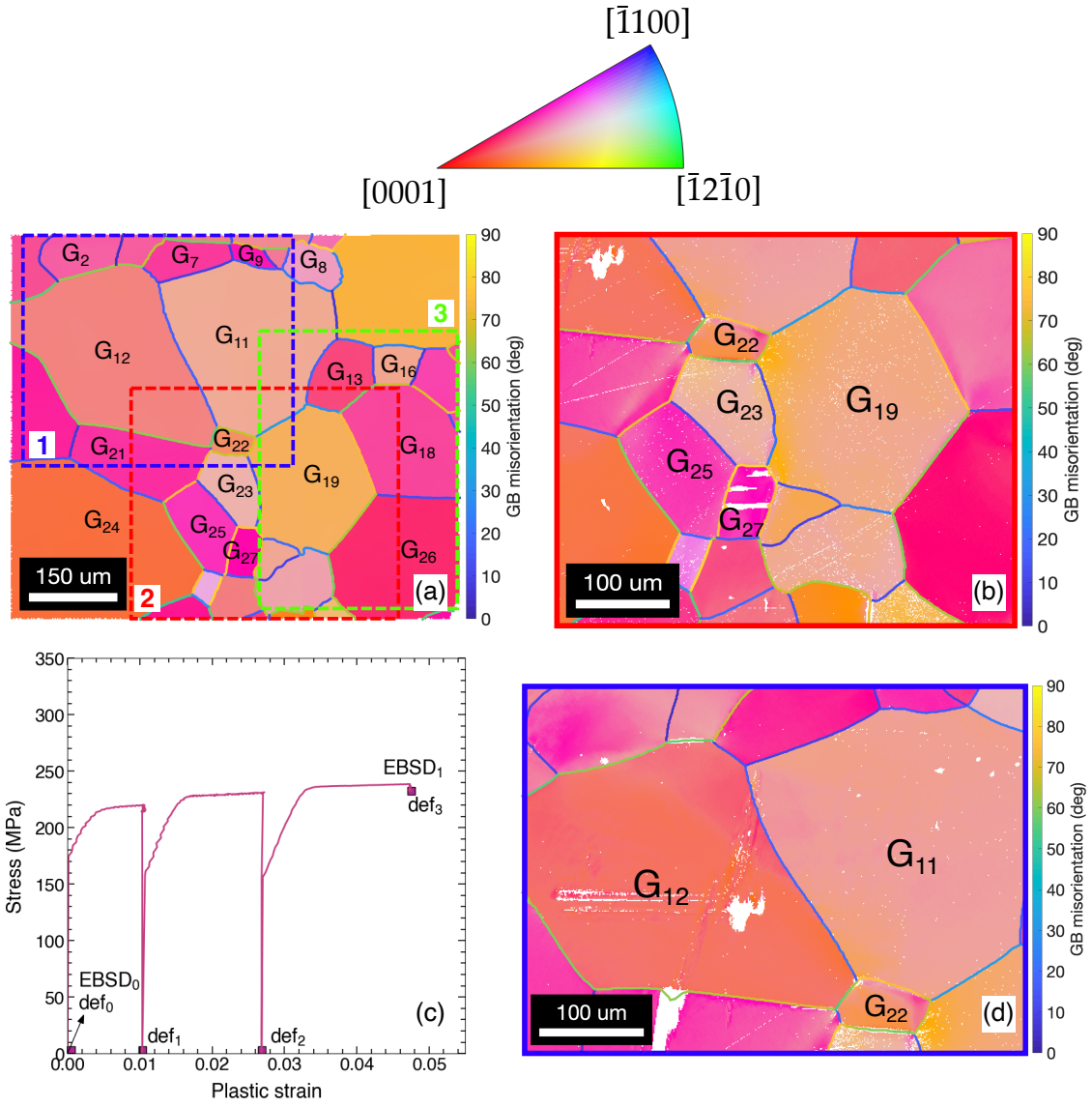

Figure 5.3: EBSD maps of the ROI surface. (a) EBSD map before deformation; the three dashed areas indicate the sub-regions where HRDIC maps were acquired. (b) EBSD map of sub-region two after 4.5% plastic strain. (c) Ex-situ tensile stress-plastic strain curve. The markers indicate the conditions in which the EBSD and the HRDIC maps were acquired. (d) EBSD map of sub-region one after 4.5% plastic strain. In the EBSD maps in (a), (b), and (d), the grains are colored according to the inverse pole figure with respect to the screen plane, shown at the top of the figure. The GBs are colored according to their misorientation angle Θ, ranging from low misorientations (blueish colors) to high misorientations (yellowish colors). The grains of interest have been labeled in (a). The non-indexed pixels have been colored in white in (b) and (d).

tions, as indicated by white arrows in Fig. 5.4 (b). When the strain reaches 4.5%, the shear strain levels and the strain concentrations at GBs and triple points drastically increase (Fig. 5.4 (c)). The shear strain distribution shows a macro-strain band that goes through G_{12}, de-

limited by the two red dashed lines in Fig. 5.4 (c) in which the shear strain is localized. As a result, the contrast between the effective strain levels within and outside the macro-band is huge.

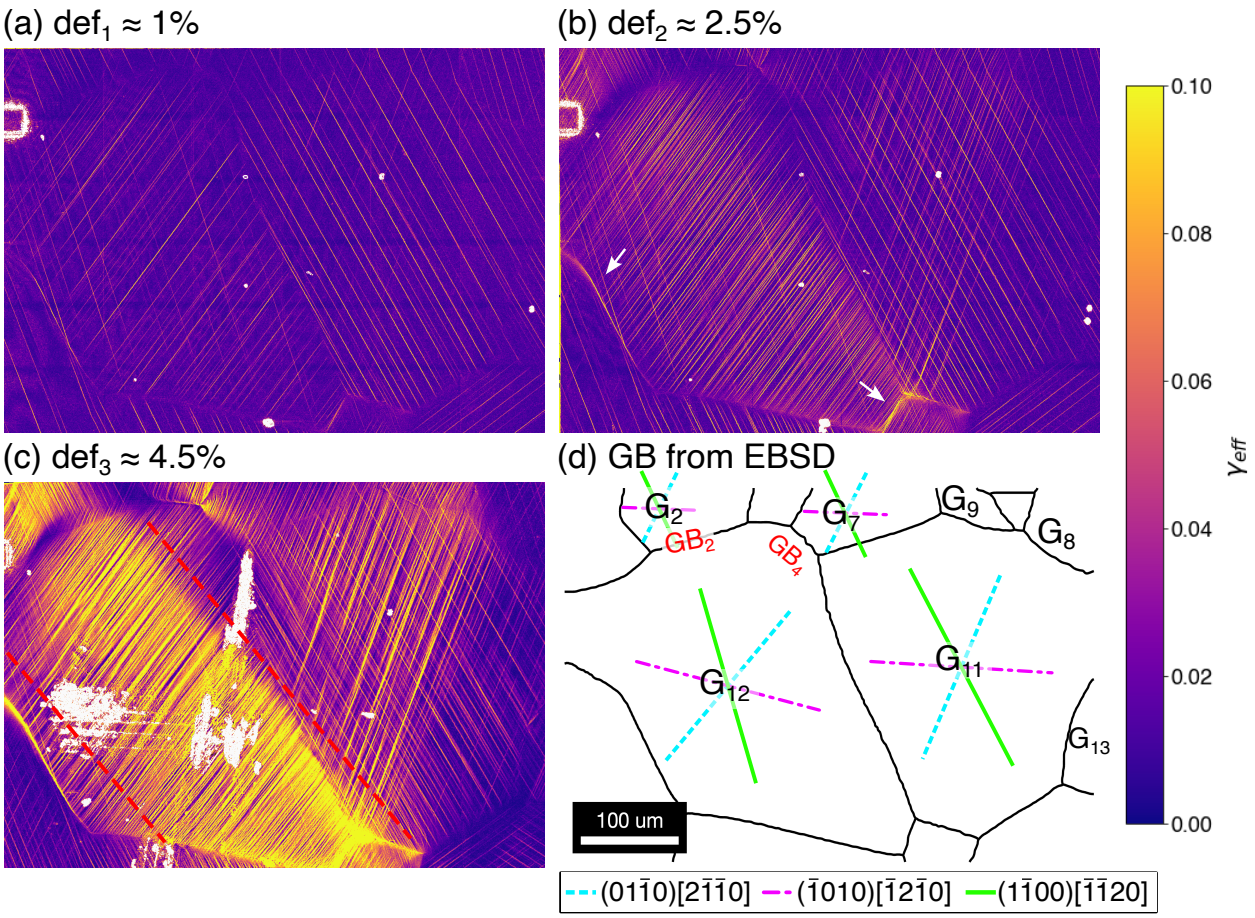

Figure 5.4: Effective shear strain maps acquired by HRDIC in the sample within sub-region 1. The correlated maps correspond to three deformation steps at (a) 1%, (b) 2.5%, and 4.5% plastic deformation. The white pixels in the maps correspond to non-correlated points caused by surface scratches and dirt deposited onto the gold nano-speckle pattern. The white arrows in (b) highlight strain concentrations close to GB and triple junctions. The red dashed lines in (c) delimit a macro-strain band. (d) GB map obtained from EBSD before deformation. The main grains and GB of study have been labeled, and the theoretical prismatic slip traces have been drawn at the center of the grains.

The effective shear strain distribution acquired in sub-region 2 is displayed in Fig. 5.5 for the three plastic strains of 1% (a), 2.5% (b) and 4.5% (c), whereas (d) presents a GB map with labeled grains and GBs of study in which the theoretical prismatic slip traces have been drawn at the center of the grains.

As observed in Fig. 5.5 (d), all slip bands are identified as prismatic, and the slip activity and intensity increase with plastic deformation. Several strain concentrations appear at 2.5% plastic deformation, especially at the triple junctions, and they are highlighted